

University of Nevada, Reno

Testing Silver Mobility: An investigation into supergene silver enrichment at the Rochester Mine in Pershing County, Nevada

A thesis submitted in partial fulfillment for the degree of Master of Science in Geology

by

Tracy L. Anderson

Dr. John L. Muntean/Thesis Advisor

December, 2016



THE GRADUATE SCHOOL

We recommend that the thesis
prepared under our supervision by

TRACY L. ANDERSON

Entitled

**Testing Silver Mobility: An Investigation Into Supergene Silver Enrichment At The
Rochester Mine In Pershing County, NV**

be accepted in partial fulfillment of the
requirements for the degree of

MASTER OF SCIENCE

Dr. John L. Muntean, Advisor

Dr. Peter G. Vikre, Committee Member

Dr. Mae S. Gustin, Graduate School Representative

David W. Zeh, Ph.D., Dean, Graduate School

December, 2016

Abstract

Supergene silver enrichment, comparable to chalcocite supergene enrichment blankets in porphyry copper deposits, has long been called upon to explain high grades in silver deposits that diminish in grade with depth. Rochester is a large-tonnage, low-grade disseminated silver-(gold) deposit hosted in Early Triassic rhyolites located in northwestern Nevada, where the role of supergene processes in controlling the distribution of ore and silver grade remained unclear prior to this study. The effect of supergene processes at Rochester was investigated by observing patterns of silver occurrences in structures, weathering zones, and ore and gangue mineral paragenesis.

The overall tabular geometry of the ore body straddling the Weaver-Rochester lithologic contact is defined by high grade zones in the lower Weaver oxide and upper Rochester oxide and mixed oxide-sulfide zones. Grades drop off significantly in the underlying protore sulfide zone. Protore hydrothermal alteration is dominated by quartz-sericite-pyrite with minor relict K-feldspar. Hypogene sulfides include pyrite, sphalerite, galena, tetrahedrite-tennantite, chalcopyrite, arsenopyrite, and rare molybdenite. Silver phases in the protore include silver-bearing tetrahedrite-tennantite; acanthite; and rare stromeyerite, pearceite, and polybasite. Geologic characteristics most closely associated with higher silver grades in oxide and mixed oxide-sulfide zones include faults, acanthite, and goethite-rich rocks. High grade zones (≥ 2 opt Ag) are controlled by high- and low-angle faults cutting the Weaver-Rochester contact. Acanthite is the dominant silver phase. Much of the acanthite formed by supergene enrichment based on its common occurrence with covellite as rims on hypogene sulfides in mixed zones. Chlorargyrite and native silver are commonly found in the oxide and mixed zone with acanthite. Other silver-halides, such as iodargyrite, are found in the oxide zone.

Based on these observations, coupled with published phase equilibria, early oxidation of protore caused the formation of silver-halides resulting in a decrease in silver mobility,

particularly when iodargyrite was stable. Upon oxidation, a small amount of silver is able to migrate to lower portions of the supergene profile forming acanthite. However, if iodide (I⁻) was not continually replenished the I/Cl ratio would have decreased and the chlorargyrite field would have expanded at the expense of iodargyrite, which would have allowed more downward transport of Ag⁺, as chlorargyrite is more soluble than iodargyrite. A dropping water table caused by uplift, erosion, and climatic changes, controlling silver deportment resulted in continued oxidation. As the water table dropped due to uplift related to Basin and Range extension, as well as decreasing precipitation from a cooling and drying climate, enriched zones would have oxidized. When groundwater was not saline chlorargyrite released Ag⁺ and upon oxidation acanthite released silver as AgHS⁰ for downward transport. New acanthite could have then formed at the deeper water table.

The amount of silver that became fixed as silver-halides and native silver in the oxide zone controlled the amount of aqueous silver in downward moving supergene fluids, which in turn controlled the extent and grade of supergene enrichment expressed as zones of abundant supergene acanthite. This was dependent on environmental conditions, including the salinity of groundwater, duration and periodicity of weathering, tectonic activity resulting in uplift and dropping of the water table, and composition of gangue minerals. The possibility that the overall tabular geometry of the Rochester ore body that sits just above the sulfide zone, resulted from supergene enrichment processes cannot be ruled out at this time without further work. Nevertheless, supergene silver enrichment certainly occurred at Rochester and resulted in high grade zones (≥ 2 opt Ag up to 70 opt) along high- and low-angle faults. Identifying the controls on such high grades is important for future exploration and mine planning.

Acknowledgements

First of all I have to profusely thank my wonderful advisor, John Muntean. John really helped make sense out of my observations and bring them all together for a coherent story. John is also an exceptional instructor and taught me more about ore deposits than I ever thought I could have learned from graduate school. This project also would not have been possible without the generous funding and support from Coeur Mining, Inc., especially Hans Rasmussen and Steve Johnson. I also want to thank all the Ralph J. Roberts Center for Research in Economic Geology (CREG) sponsors for their kind contributions to the program and John for being a great leader of the program. Thanks to Peter Vikre for all the past work he has done in the Rochester district as well as his support of this project. I thank my outside committee member, Mae Gustin, for her helpful comments and different perspective. I am very appreciative to all the laboratory help I received from Joel DesOrmeau in the SEM lab at UNR, Minghua Ren on the electron microprobe at UNLV, and Lisa Peters for $^{40}\text{Ar}/^{39}\text{Ar}$ analysis at NMT. I also want to thank the entire geology team at Rochester for their assistance and discussions. Big thanks to Susan Abbott for taking me in as her own during my summer work at Rochester and Tawandaroo and Girl Girl for being my away-from-home best dog friends. I need to thank my husband Ryan for not only putting up with the stressed version of me but also for thoughtful and insightful discussions on AFT, erosion, and thrusting. Ryan also made sure I never had pixelated figures, which I now appreciate. There are so many wonderful CREG and other UNR graduate students that shared their love, support, and knowledge with me and friendships made that I hope will last through the years. Lastly, I want to thank my parents and siblings for their unwavering support and have all been great examples to me.

Table of Contents

Abstract.....	i
Acknowledgements.....	iii
List of Tables.....	v
List of Figures.....	vi
Introduction.....	1
Background and Geologic Setting.....	2
Methods.....	12
Mineralization.....	16
Evidence for Supergene Enrichment.....	63
Geochronology.....	73
Interpretation of the Supergene Profile at Rochester.....	77
Regional Comparisons to other Silver-rich Districts.....	91
Conclusions.....	96

List of Tables

Table 1. Minerals associated with hypogene and supergene ore at Rochester.....	18
Table 2. $^{40}\text{Ar}/^{39}\text{Ar}$ analytical data.....	76

List of Figures

Figure 1. Idealized supergene profiles.....	2
Figure 2. Geologic map of the Humboldt Range.....	4
Figure 3. Geologic map of the Rochester Mine pit.....	10
Figure 4. Schematic geologic cross section through the Rochester Mine pit.....	10
Figure 5. Examples of crackle breccia.....	11
Figure 6. Locations of pit benches and core holes logged.....	13
Figure 7. Hypogene mineralization from Rochester Formation sulfide zone.....	19
Figure 8. Hypogene mineralization from Rochester Formation sulfide zone.....	20
Figure 9. Hypogene and supergene mineralization from Rochester Formation sulfide zone.....	21
Figure 10. Hypogene mineralization from Rochester Formation sulfide zone.....	22
Figure 11. Supergene sphalerite and acanthite from the Rochester Formation sulfide zone.....	23
Figure 12. Low-grade mineralization and alteration from the Weaver Formation oxide zone.....	24
Figure 13. Mineralization and alteration in the Weaver Formation oxide zone.....	25
Figure 14. Supergene mineralization from the Rochester Formation oxide zone.....	26
Figure 15. Supergene mineralization from the Weaver Formation oxide zone.....	27
Figure 16. Supergene mineralization from the Weaver Formation oxide zone.....	28
Figure 17. Supergene mineralization from the Weaver Formation oxide zone.....	29
Figure 18. Supergene mineralization from the oxide zone.....	30
Figure 19. Supergene mineralization from the oxide zone.....	30
Figure 20. Supergene mineralization from the Weaver Formation oxide zone.....	31
Figure 21. Supergene mineralization from the Weaver Formation oxide zone.....	32
Figure 22. Supergene mineralization from the Weaver Formation oxide zone.....	33
Figure 23. Supergene mineralization and hypogene sulfides from the Rochester Formation mixed zone.....	34
Figure 24. Hypogene alteration in the Rochester Formation mixed zone.....	35
Figure 25. Hypogene alteration in the Rochester Formation mixed zone.....	36
Figure 26. Mineralization and alteration in the Rochester Formation mixed zone.....	37
Figure 27. Hypogene mineralization and alteration in the Rochester Formation mixed zone.....	38
Figure 28. Supergene and hypogene sulfides in the Rochester Formation mixed zone.....	39
Figure 29. Supergene and hypogene mineralization in the Rochester Formation mixed zone.....	40
Figure 30. Hypogene sulfides cut by supergene covellite.....	41
Figure 31. Hypogene acanthite in the Rochester Formation mixed zone.....	43
Figure 32. SEM EDS elemental maps of tetrahedrite, acanthite, and galena.....	44
Figure 33. SEM EDS elemental maps of tetrahedrite, acanthite, and galena.....	45
Figure 34. Supergene mineralization in the Rochester Formation mixed zone.....	46
Figure 35. SEM EDS elemental maps showing supergene acanthite.....	47
Figure 36. SEM EDS elemental maps showing supergene acanthite and covellite.....	47
Figure 37. Electron microprobe WDS and SEM EDS elemental maps of sulfides.....	48
Figure 38. Mineralization and alteration from the Rochester Formation mixed zone.....	48
Figure 39. SEM EDS elemental maps of acanthite and goethite from the mixed zone.....	49
Figure 40. Supergene mineralization from the Rochester Formation mixed zone.....	50
Figure 41. SEM EDS elemental maps showing acanthite rimming sphalerite.....	51
Figure 42. SEM EDS elemental maps showing supergene mineralization.....	52
Figure 43. Supergene mineralization from the Rochester Formation mixed zone.....	53
Figure 44. Supergene mineralization from the Rochester Formation mixed zone.....	54
Figure 45. Electron microprobe WDS elemental maps showing supergene acanthite.....	55
Figure 46. Mineral phase paragenesis.....	56

Figure 47. Cross section through the Rochester pit with varying silver grades.....	58
Figure 48. Multiple cross sections through the Rochester pit with high silver grades.....	59
Figure 49. Sampled drill core intervals with the highest silver grades.....	60
Figure 50. Geological characteristics compared to assays in core hole ERC14-002.....	61
Figure 51. High grade sampled drill core in the Weaver Formation oxide zone.....	62
Figure 52. Mapped pit bench 6425 #2 showing the location of samples collected.....	62
Figure 53. Mapped pit bench 6425 #1 showing the location of samples collected.....	63
Figure 54. Elevation vs. silver grade.....	65
Figure 55. Elevation vs. gold grade and elevation vs. Ag:Au.....	66
Figure 56. Al ₂ O ₃ % vs. Zr (ppm) immobility plot with silver and copper.....	67
Figure 57. Specific gravity measurements relative to silver grade and weathering zone.....	68
Figure 58. Al ₂ O ₃ % vs. Zr (ppm) immobility plots with arsenic and silver, gold and silver.....	70
Figure 59. Al ₂ O ₃ % vs. Zr (ppm) immobility plots with lead and silver, and zinc and silver.....	71
Figure 60. Jarosite ⁴⁰ Ar/ ³⁹ Ar age spectra for sample NPWR 41.....	74
Figure 61. Jarosite ⁴⁰ Ar/ ³⁹ Ar age spectra for sample NPWS 45.....	75
Figure 62. Schematic timeline of the geologic events in the Humboldt Range.....	77
Figure 63. Oxygen fugacity vs. pH diagram for copper in the supergene environment.....	84
Figure 64. Oxygen fugacity vs. pH diagram for silver in the supergene environment.....	85
Figure 65. Schematic diagram of the interpreted supergene profile progression at Rochester.....	88

I. Introduction

The ability of silver to behave similar to copper in the weathering environment has historically been accepted, largely due to similar dissolution and transport characteristics in acidic solutions (Emmons, 1917; Titley and Marozas, 1995). While supergene processes involving copper deposits have been studied extensively, there have been few recent published studies on silver deposits (Mann, 1984; Webster and Mann, 1984; Saunders, 1993; Greffie et al., 2002; Rainbow et al., 2006; Sillitoe, 2007 and 2009; Fanlo et al., 2010; Reich et al., 2010; Yesares et al., 2014). Copper porphyry deposits often develop well defined supergene profiles (Fig. 1A), characterized by an oxidized and leached cap overlying a copper-sulfide enriched zone above hypogene mineralization (Blanchard, 1968; Anderson, 1982). If the historic view of silver behavior is correct, similar supergene processes could also form economically significant zones enriched in silver. However, Sillitoe (2009) reviewed 40 of the world's premier silver deposits, and concluded silver is relatively immobile in the supergene environment (Fig. 1B), including the large disseminated Rochester silver deposit in Nevada. He suggested any enrichment is largely the result of residual enrichment due to the extreme insolubility of silver-halides and efficient fixing of silver, calling into question the applicability of the copper supergene model to silver deposits (Sillitoe, 2009).

The main objective of this study was to test Sillitoe's (2009) conclusions and determine the role supergene weathering processes had on secondary silver deposition, including remobilization and possible enrichment at the Rochester deposit. This was accomplished by systematically identifying silver deportment in the oxide zone, near the sulfide-oxide boundary and within the sulfide zone; defining mineral paragenesis in both the oxide and sulfide zones; and describing how gold and silver relate to each other and to geological characteristics. Detailed pit mapping, core logging, downhole geochemistry, petrography, microanalyses of minerals, and geochronology were employed. If supergene enrichment exists, two observations are expected.

First, at the deposit scale, blanket-like or structurally controlled zones with higher silver grades should be present near the oxide-sulfide boundary. Secondly, at the microscopic scale, silver-bearing minerals and other minerals containing mobile elements, like copper, should be observed as rims on hypogene sulfides, such as pyrite. Alternatively, if such enrichment zones and rims are absent, the distribution of silver grades might be explained by hypogene zonation or residual enrichment within the oxide and mixed oxide-sulfide zones.

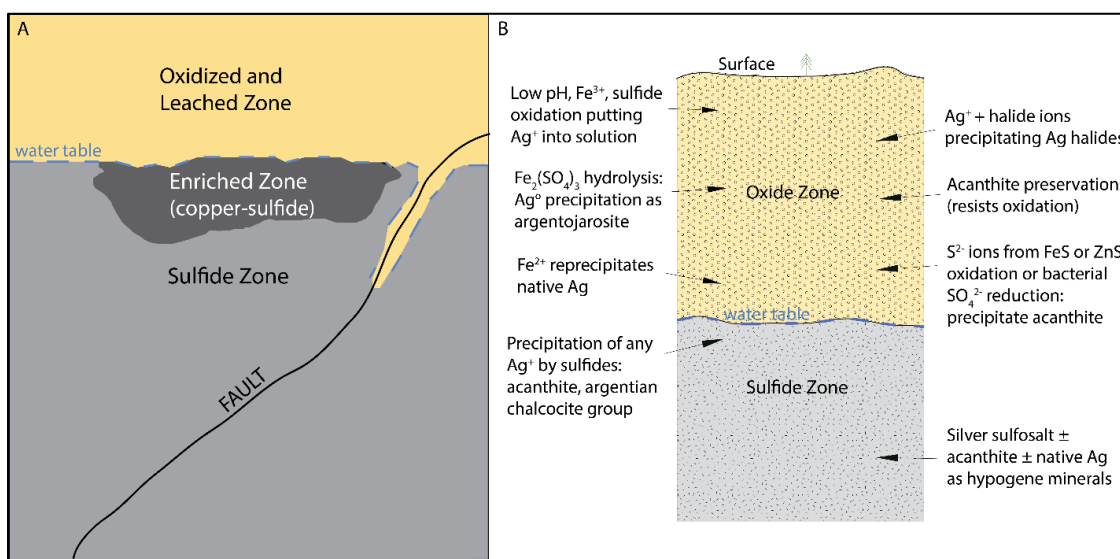


Figure 1. **A.** Idealized supergene profile of a copper-porphyry deposit with an initial copper-sulfide enriched zone at the water table modified from Anderson (1982). **B.** Schematic cross section depicting idealized interpreted supergene silver profile modified from Sillitoe (2009).

II. Background and Geologic Setting

Historically, numerous silver mines throughout Nevada have been short-lived after their shallow high-grade oxidized and underlying sulfide portions of veins were exploited. Examples of short-lived camps include Lander Hill in the Reese River District near Austin, the Belmont District in northern Nye County, and the Candelaria District in Mineral County (Page, 1959). Several of these mines contained chlorargyrite (see Table 1 for chemical formulas) and other silver-halides as the principal ore minerals in the shallow oxide zone, and electrum, native silver, acanthite, and

silver-bearing sulfosalts and galena deeper in the sulfide zone (Ross, 1953; Stager, 1977; Kleinhampl and Ziony, 1984). Most workers noted limonite and other oxides as vein constituents with sulfides suggesting ore was mined from both the oxide and mixed oxide-sulfide zones (Page, 1959; Stager, 1977; Kleinhampl and Ziony, 1984).

Silver was first discovered in the Rochester Mine area in 1911 when high-grade veins were found at the surface. From 1912 to 1928 720,000 tons of ore were produced from the Rochester district averaging 12 ounces of silver and 0.10 ounces of gold (Vanderburg, 1936; Vikre, 1981). Once the high-grade oxide and acanthite-rich mixed oxide-sulfide ores were mined (Knopf, 1924), silver production ceased until 1981 when ASARCO defined a low-grade bulk-tonnage resource, which was subsequently acquired by Coeur Mining, Inc. in 1983. Today Coeur mines Rochester as a low-grade, bulk-tonnage open pit silver-gold mine. In 2015, 4,631,000 ounces of silver and 52,588 ounces of gold were mined from ore grade averaging 0.63 opt silver and 0.003 opt gold (Coeur Mining, Inc., 2015). Silver and gold are extracted by cyanide heap leaching and processed using the Merrill-Crowe method. Projected life of pad recovery rates of crushed ore material is 92% for gold and 61% for silver, whereas 70% of the gold and 20% of the silver is recovered from run of mine ore (Robinson et al., 2014).

Regional Geology

The Rochester Mine sits in the center of a broad north-trending antiform of the Humboldt Range (Vikre, 1981), and is located 26 miles northeast of the town of Lovelock (Fig. 2) in Pershing County, Nevada. The Humboldt Range is host to numerous precious metal deposits ranging in age from Late Cretaceous to Quaternary (Vikre, 1981; John and Muntean, 2006; Price et al., 2014; Fifarek et al., 2015). The oldest rocks exposed in the Humboldt Range, are the Koipato Group, a sequence of Early Triassic volcanic rocks and intrusions with minor siliciclastics (Knopf, 1924; Wallace et al., 1969; Vikre, 1977). Volcanism represented by the

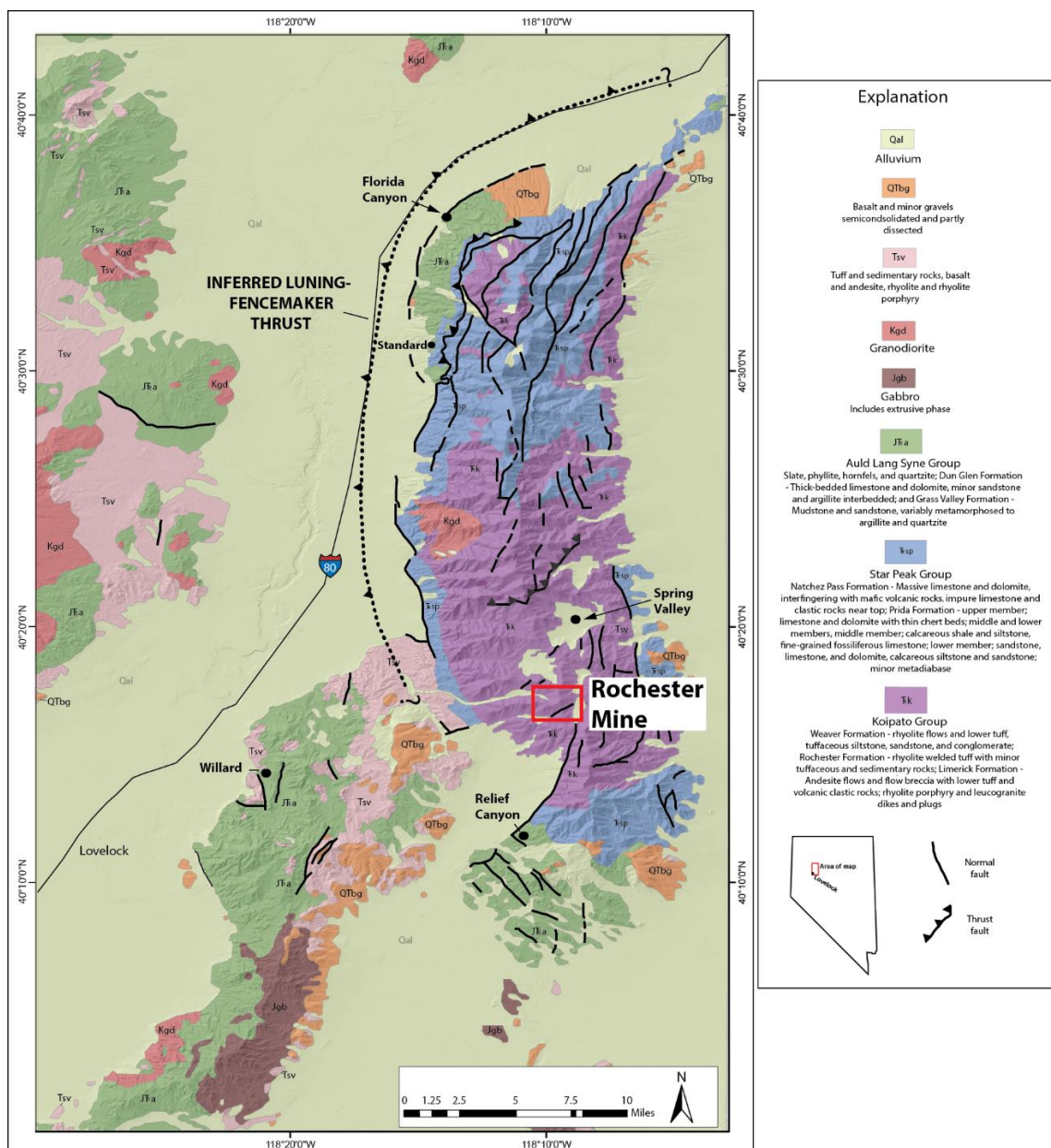


Figure 2. Geologic map of the Humboldt Range and surrounding ranges showing the location of the Rochester Mine (modified from Silberling and Wallace, 1967; Wallace et al, 1969a, 1969b; Wyld, 2016).

Koipato Group overlies the Golconda allochthon, which was emplaced during the Permian Sonoma Orogeny (Ferguson et al., 1952; Silberling and Roberts, 1962; Vetz, 2011). Whether movement along the Golconda thrust ceased after the deposition of subaerial Koipato volcanics continues to be debated (Wilkins, 2010).

Koipato volcanism ceased by Middle Triassic and a marine transgression ensued, as evidenced by fossiliferous limestone overlying basal conglomerate and sandstones of the Star Peak Group unconformably overlying the Koipato Group. The Middle to Middle-Upper Triassic Star Peak Group is dominantly a marine sedimentary package composed of fossiliferous limestones, mudstones, siltstones, and sandstones deposited in a vertical transition from shelfal to basinal carbonate sequence, the result of subsidence of the western continental margin (Knopf, 1924; Nichols and Silberling, 1977; Silberling and Nichols, 1982). Marine carbonate deposition concluded as the Star Peak Group was then overlain by the terrigenous Upper Triassic to Jurassic (?) Auld Lang Syne Group largely composed of mudstones, shale, and sandstones interbedded with limestone and dolomite, variably metamorphosed to argillite, phyllite, and quartzite (Silberling and Wallace, 1969; Burke and Silberling, 1974; Wyld et al., 2003).

Regionally, the late Jurassic Luning-Fencemaker Fold and Thrust Belt resulted in Mesozoic shortening in the back-arc of the U.S. Cordillera. This orogenic event produced low- and high-angle structures and metamorphosed late Permian-Jurassic strata in the Humboldt Range (Wyld, 2002; Wyld et al., 2003; Yonkee and Weil, 2015). Jurassic and Cretaceous intrusions throughout the range have been identified from dating both exposed intrusions and variably metamorphosed alteration mineral assemblages in older rocks, namely quartz-andalusite-dumortierite-muscovite and quartz+sericite±pyrite. A Jurassic mafic intrusive complex dated at ~170 Ma is widely exposed in the nearby West Humboldt Range, Stillwater Range, and Clan Alpine Mountains (Johnson and Barton, 2000). This intrusive body is interpreted to underlie portions of the Humboldt Range based on 168.6 ± 9.3 Ma Rb-Sr age of strongly altered Koipato

Group rocks in Limerick Canyon as well as δD and $\delta^{18}O$ values from altered rocks that correspond to the Jurassic magmatic waters (Kistler and Speed, 2000; Vikre, 2014). Late Cretaceous felsic intrusions in the Humboldt Range are largely inferred to underlie the range. The largest exposed Cretaceous intrusion is quartz monzonite in composition outcropping in Wright and Rocky Canyons with U/Pb ages of zircon ranging from ~92 to 89 Ma (Marvin and Dobson, 1979; Crosby, 2012; Vikre, 2014). The youngest granitic intrusion in the Humboldt Range is a ~32 Ma granodiorite found in the lower portion of Spring Valley based on U/Pb dates of zircon and $^{40}Ar/^{39}Ar$ of hornblende and biotite (Crosby, 2012; Vikre, 2014). Overlying the Auld Lang Syne Group in the West Humboldt range, a thin layer of Oligocene-Miocene fresh and marine carbonates and conglomerates are overlain by Tertiary aged Miocene(?) rhyolitic and dacitic tuffs (Bonham and Sharp, 1957; Wallace et al., 1969b; Vikre, 1977).

Basin and Range extension is responsible for ~N-S normal faulting within and bounding the Humboldt range. Late Miocene basalt dated at ~12-9 Ma occurs along the eastern flanks of the range and covers semi-consolidated Tertiary and Mesozoic sedimentary rocks along the eastern West Humboldt Range (Wallace et al., 1969; Vikre, 1977). Basin and Range faulting likely began with the onset of Tertiary volcanism and prior to Late Miocene basalts suggested by gravels of Koipato and Star Peak Group rocks interbedded with younger silt and tuff (Vikre, 1977). There were at least three major periods of erosion and exhumation in the region throughout the Mesozoic and Cenozoic complicating weathering history (Wyld, 2002; Wyld et al., 2003; Colgan et al., 2006). Shoreline deposits on the eastern and northwestern sides of the Humboldt Range show the high-stand for Pleistocene-Quaternary Lake Lahontan (Vikre, 1977; Silver et al., 2011).

District Geology

The Rochester Mining District makes up the central part of the Humboldt Range where the largest ore deposit is the Rochester mine. Other silver-gold and gold deposits in the district include Nevada Packard, Lincoln Hill, Independence Hill, and Spring Valley (Knopf, 1924; Vikre, 1977; Vikre, 2014). Non-precious metal ore deposits and industrial mineral deposits also occur in the district, including Pb-Zn, Be, U, and dumortierite (Knopf, 1924; Johnson, 1977; Vikre, 2014). Placers have historically been mined in nearby canyons and are still worked by independent claim owners.

Mineralization in the Rochester district is hosted primarily by the Koipato Group and is comprised of (oldest to youngest) the Limerick, Rochester, and Weaver Formations (Vikre, 1977; Vetz, 2011). The Limerick Formation dated by Vetz (2011) yielded a U/Pb date on zircon of 249.59 ± 0.08 to 249.37 ± 0.1 Ma and is composed of andesitic flows with lesser lithic and crystal tuffs, and volcanic derived siltstones and conglomerates. Limerick rocks are variably metamorphosed to greenstone that resulted from numerous metasomatic events related to intrusions in the Early Triassic, Jurassic intrusions, Luning-Fencemaker thrusting, and Cretaceous magmatism (Wyld et al., 2003; Vikre, 2014). The Rochester Formation, dated by U/Pb of zircon at 249.36 ± 0.07 to 248.53 ± 0.07 Ma (Vetz, 2011; Crosby, 2012) unconformably overlies Limerick rocks. The Rochester Formation is composed of aphyric to quartz-phyric rhyolite ignimbrites and porphyritic crystal rhyolite tuff, as well as minor ash layers, epiclastic sandstone, and siltstones (Johnson, 1977; Vikre, 1977; Martz and Reid, 1987; Crosby, 2012; Chadwick, 2014). The Weaver Formation was previously interpreted to overlie the Rochester along an unconformity; however, recent U/Pb dates on zircon (248.97 ± 0.07 to 248.32 ± 0.08 Ma) overlap with the Rochester (Vetz, 2011). The Weaver Formation is composed of rhyolites containing welded to non-welded lithic crystal-rich tuff with minor ash, and is capped by siltstones and

sandstones with spherulitic tuff at the south end of the district (Vikre, 1977; Martz and Reid, 1987; Chadwick and Harvey, 2001).

Two granitic phases intrude the Limerick and Rochester Formations and have historically been thought to be the intrusive equivalents of the Rochester and Weaver Formation (Wallace et al., 1960; Wallace et al., 1969a; Vikre, 1977). Zircons in leucogranite predate the Weaver Formation and have been dated by the U/Pb method at 249.13 ± 0.07 to 249.09 ± 0.08 Ma (Vetz, 2011; Crosby, 2012). Leucogranite is located directly east of the Rochester mine and the Black Ridge Fault as well as to the northwest in Limerick Canyon (Wallace, et al., 1969a; Vikre, 1977; Crosby, 2012). Rhyolite porphyry dikes yield U/Pb dates of 249.33 ± 0.08 to 249.08 ± 0.14 Ma (Vetz, 2011; Crosby, 2012) and often crop out alongside the leucogranite, and then increase in abundance north of Lone Mountain (Wallace et al., 1969b; Vikre, 1977).

Quartz+sericite+pyrite (QSP) is the most common alteration assemblage and is pervasive throughout the district (Vikre, 1981, 2014; Crosby and Thompson, 2015). Luning-Fencemaker thrust sheets as well as the Jurassic intrusive body are thought to account for this alteration on a regional scale (Vikre, 2014). Cretaceous intrusions were responsible for silver-gold mineralization and overprinting QSP alteration in the Rochester district and Spring Valley project. The Cretaceous age of this mineralizing event is evidenced by $^{40}\text{Ar}/^{39}\text{Ar}$ and K-Ar dates of muscovite from altered Koipato Group rhyolites and vein material which spans U/Pb dates of zircons from Cretaceous aged intrusions in the range (Crosby 2012; Vikre, 2014). Sericite from alteration halos and veins from Nenzel Hill at the Rochester mine yielded ~103-86 Ma ages from $^{40}\text{Ar}/^{39}\text{Ar}$ and K-Ar dates (Vikre, 1977, 2014).

The first recognized deformation event exposed in the Humboldt Range is the Jurassic Luning-Fencemaker fold and thrust belt (Heck, 1987; Cheong, 1999; Wyld et al., 2003). These deformational phases resulted in generally east-verging thrusts; N-NE-trending, west dipping penetrative foliation; and concentrated folding of the Star Peak Group (Cheong, 1999; Price et al.,

2014). The Black Ridge fault zone is a prominent structural zone bounding the Rochester deposit to the east. The fault trace extends from Moonlight Basin to the north to Nevada Packard to the south and then becomes a range-bounding fault south to Relief Canyon (Silberling and Wallace, 1967; Wallace et al., 1969; Crosby and Thompson, 2015).

Based on H₂O-CO₂-NaCl fluid inclusions, sphalerite geobarometry, and ⁴⁰Ar/³⁹Ar muscovite dates, rocks were buried to a depth of at least 3.8 km during Cretaceous mineralization at Rochester. If these estimates are correct, then at least one half of the Luning-Fencemaker allochthon had been removed prior to mineralization and the remainder has been eroded since mineralization (Vikre, 1977, 2014), suggesting the Rochester district is largely in the lower plate of the Luning-Fencemaker thrust.

Local Geology

The Rochester and Weaver Formations are the only units encountered in the Rochester mine area (Fig. 3). The most common hydrothermal mineral assemblage is quartz+sericite+pyrite±K-feldspar and is possibly related to numerous magmatic and tectonothermal events in the region, including intrusions coeval with the primary deposition of Koipato Group rocks, Jurassic magmatism and deformation, and Cretaceous intrusions (Vikre, 1977; 1981; 2014). Locally, silicification is strong, commonly obscuring primary volcanic textures. The Rochester deposit is cut by a series of high-angle faults that strike predominantly N-S, some of which show apparent normal displacement and others reverse displacement. There is also a set of stacked low-angle faults cutting through the deposit which strike mostly N-S to NE and have a westerly dip (Fig. 4) (Chadwick and Harvey, 2001).

Textures are also masked by supergene oxidation, which occurs as variably developed zones of pervasive goethite and hematite. Pervasive hematite locally increases near the Weaver-Rochester contact and adjacent to faults. Very minor jarosite locally occurs adjacent to mixed

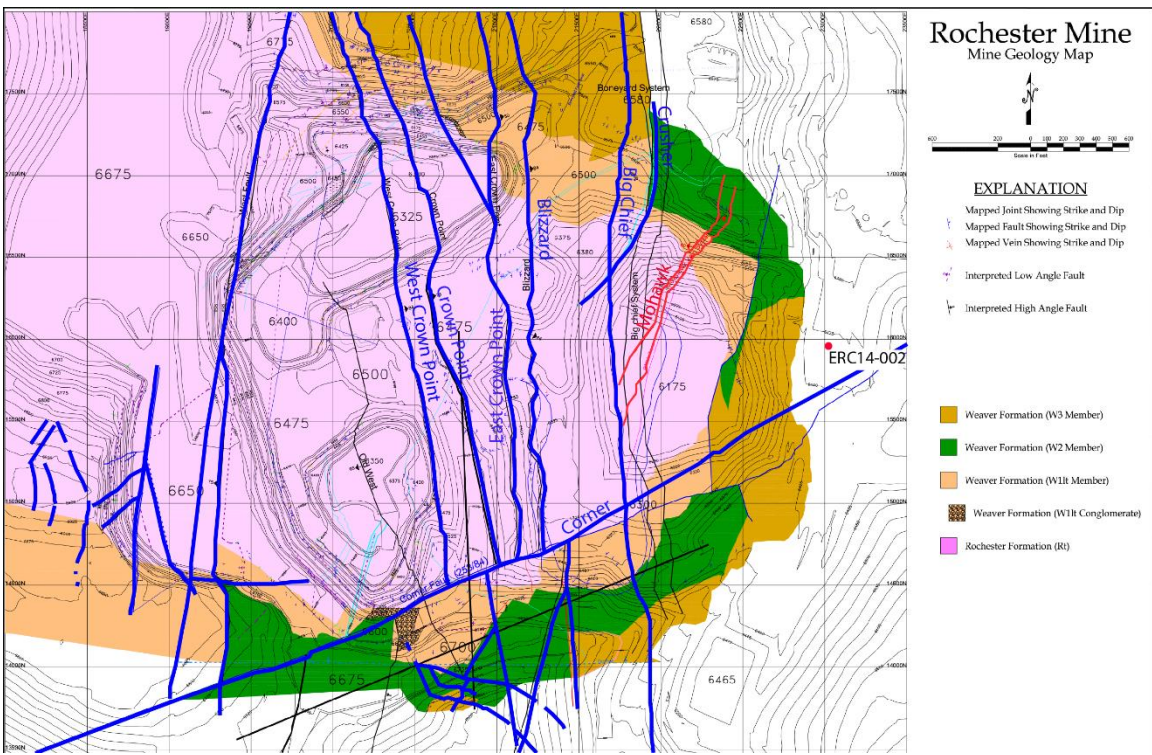


Figure 3. Geologic map of the Rochester Mine pit. Collar location for core hole ERC14-002 is indicated by red dot. (Modified from White and Chadwick, 2015; Chadwick et al., 2016).

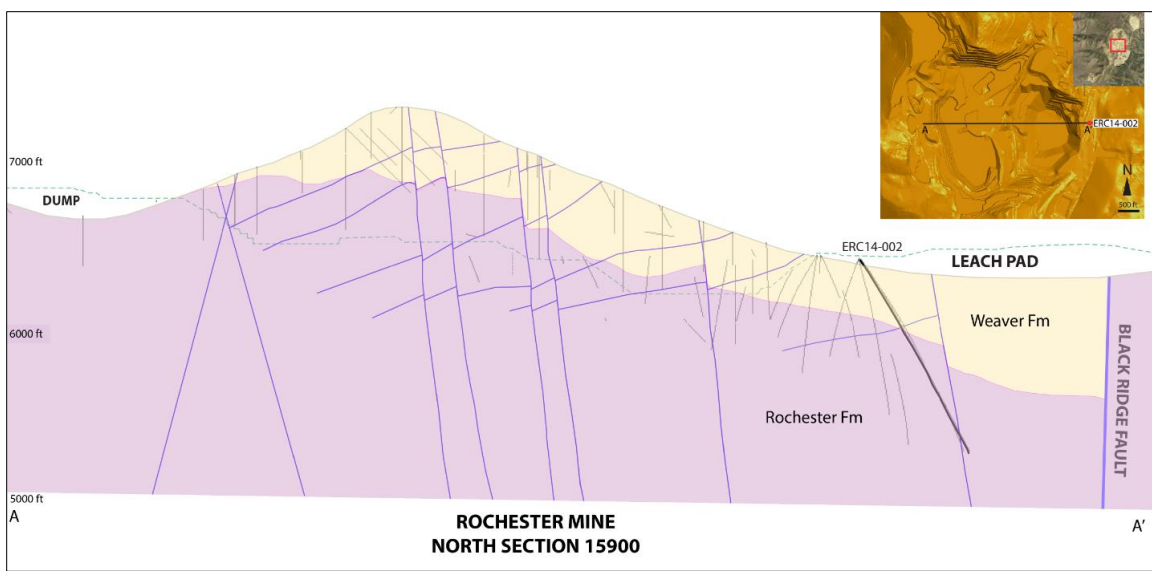


Figure 4. Schematic cross section A-A' showing stacked low-angle faults cut by high-angle faults through the Rochester deposit.

oxide-sulfide zones. Boundaries between mixed sulfide-oxide zones and oxide zones commonly occur at major faults, suggesting faults were important in focusing groundwater during weathering.

Silver-(gold) mineralization typically occurs near the Rochester-Weaver contact, which is commonly defined by a crackle breccia with a quartz±goethite±pyrite matrix (Fig. 5). The

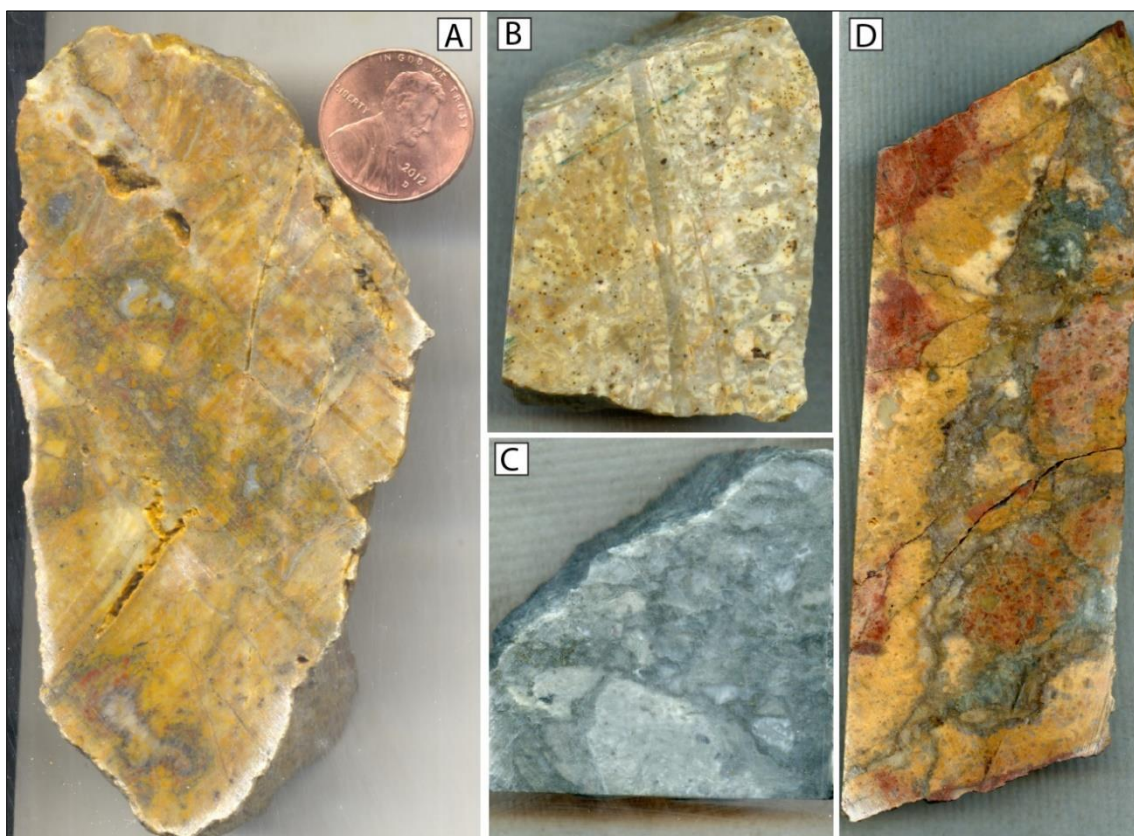


Figure 5. **A.** Crackle micro breccia from R11C-006 core hole at 38.5 feet in the Weaver Formation 5-foot interval assayed 4.1 opt Ag and 0.001 opt Au. **B.** Quartz veinlet cutting pervasive crackle breccia from HQ core hole ROCC16-1051 at 355 feet in the Rochester Formation and is not yet assayed. **C.** Crackle breccia in the mixed weathering zone in HQ core hole ERC14-002 at 655 feet in the Rochester Formation 8-foot interval assayed 0.1 opt Ag and 0.001 opt Au. **D.** Also from ERC14-002 crackle breccia at 409.2 feet in the Weaver Formation 5.2-foot interval ran 3.4 opt Ag and 0.003 Au.

breccia matrix is gray to milky white quartz with a cherty to fine-grained texture, clasts represent ~80% and are ~2-40 mm angular to subangular, pyrite or goethite can locally make up ~10% of

the matrix. This apparent hydrothermal breccia, characterized by a mosaic of angular to sub-angular rhyolite clasts with a quartz matrix, can extend a few hundred feet into the Rochester Formation. The matrix is dominated by cherty to fine-grained light gray quartz. Whether there are two, or possibly more, hydrothermal brecciation events, one characterized by light gray cherty to fine grained quartz matrix and the other by a fine-grained quartz±goethite±pyrite matrix, remains unclear. Ore also occurs as quartz-sulfide veinlets and disseminations in both the Weaver and Rochester Formations. Quartz±sulfide veinlets are dominantly ~1-2 mm and often cut the light gray quartz matrix of the crackle breccia (Fig. 5B). Higher grade ores appear to be controlled by shear zones and commonly occur at the intersection of high- and low-angle faults. In addition, silver and gold grades are higher in the oxide and oxide-sulfide mixed weathering zones and are mined exclusively from these zones. Prior to this study, whether this zonation resulted from supergene processes or original hypogene mineralization was a major outstanding question at Rochester and is addressed in detail below.

III. Methods

Core logging and open pit mapping were done in the summer of 2015 and 2016 using the Anaconda method. The method utilizes a color-coded scheme, which includes graphical and numerical data on rock type, structure, vein types, hydrothermal and supergene alteration, approximate volume percent of minerals and veins, and relative ages between the mapped features. Five core holes were logged in detail and six more were logged in a reconnaissance fashion to compare geological characteristics to silver grades. Six 150-foot sections of pit benches were mapped in detail (Fig. 6), and samples were collected for assay. Samples from core logging and pit mapping were collected for petrography and microanalyses. Samples from pit mapping were assayed at Coeur Rochester's on site laboratory using the fire-assay method followed by atomic absorption spectrophotometry.

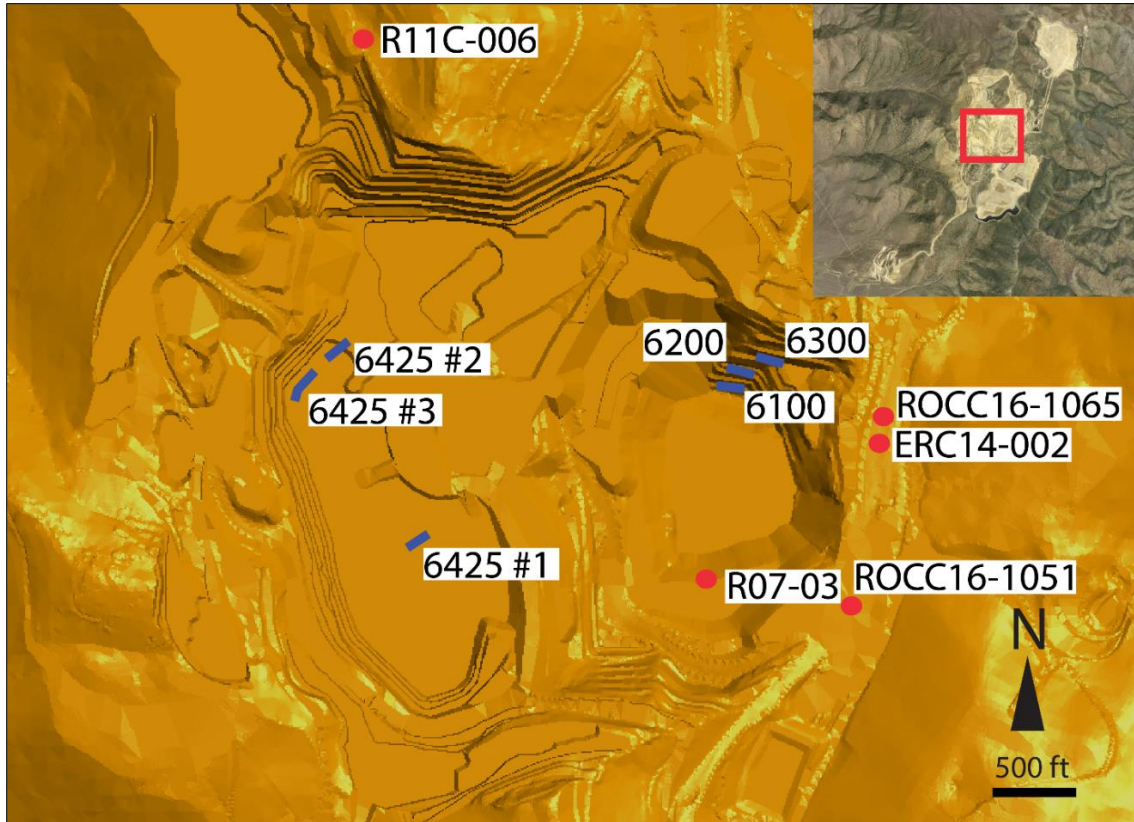


Figure 6. Locations of the five core holes logged in detail and six pit benches mapped.

Three core holes were logged in the summer of 2015. Core hole ERC14-002 was the focus of this study because of its well-defined oxide, mixed, and sulfide zones; good exposure of the Weaver-Rochester contact; and a high grade intercept of 71 opt Ag. ERC14-002 was drilled on the east side of the Rochester mine (Fig. 6) in the newly discovered “East Rochester” ore zone. Core hole ERC14-002 was assayed for gold, silver, and analyzed for 48 other elements by ALS Minerals in Reno. Silver was analyzed by fire assay with a gravimetric finish. Gold was analyzed by fire assay with an atomic absorption finish. The other 48 elements were analyzed by four acid digestion and finished with ICP-MS. Ore grade elements were reanalyzed with ICP-AES. Blanks and standards were inserted in the sample stream based on industry QA/QC standards. Sample breaks were chosen based on geological characteristics including oxidation

intensity, structure, and veining/silicification. The lengths of sample breaks ranged from 0.4 to composites of 27.4 feet.

Two of the core holes, R11C-006 and R07-03, were logged and sampled for microanalysis in the summer of 2015. These two older core holes were the only other intact core holes with high silver grades available at the time. Core hole R11C-006 was drilled in 2011 and is located on the northwestern side of the deposit (Fig. 6). Core hole R07-03, was drilled in 2007 and located on the southeastern side. R11C-006 and R07-03 were sampled and assayed for gold and silver on five to ten foot intervals soon after they were drilled.

A drilling program, including eight core holes, was completed and logged in the summer of 2016. Two of the holes ROCC16-1051 and ROCC16-1065, were logged in detail and samples were taken for petrography and microanalyses. Sample breaks for core hole ROCC16-1065 were based on geological features and sample lengths ranged from 1.0 to 5.3 feet. Due to time constraints, all other core holes were sampled on five foot breaks. Assay results for core holes logged in 2016 are not back at this time.

The oxide, mixed, and sulfide zones were modeled with the 3D modeling packages Leapfrog and Gemcom to characterize a relationship between lithology, faults, supergene oxidation and silver grade. The database used to model the oxidation surfaces is large (157,187 assay records from over 3,400 drill holes) and the majority of data are pre-2008, which was prior to use of the acQuire database software. These older data can be problematic in that they have missing assays and geological information. A dataset had to be selected for modeling since it would not be possible to use the entire database. A total of 707 drill holes were used based on several parameters including recent drilling, a representative distribution across the deposit, and data integrity, which was assessed by comparing the paper geologic log to the database record. Once holes were selected, drilling intervals were assigned to either oxide, mixed oxide-sulfide, or sulfide zones based on logs. Surfaces for tops of the mixed oxide-sulfide and sulfide zones were

created as a first pass in Leapfrog then adjusted in Gemcom to generate more accurate boundaries. Lithologic contacts and fault surfaces modeled by Rochester geologists were utilized.

Core and pit wall samples, ~115 and 47 respectively, were taken during logging and mapping. From these samples 84 were examined with the binocular microscope and polished thin sections were prepared. Low- to high-grade transects in the oxide, mixed oxide-sulfide, and sulfide weathering zones were targeted when selecting samples for microanalysis. Thin sections were examined using transmitted and reflected light microscopy. Selected polished thin sections were then examined using the JEOL 6010 scanning electron microscope (SEM). Images and element maps captured using the SEM typically used a voltage of 15 or 20 kV, a spot size of 63, and a working distance of 10 mm. The JEOL 7100 SEM was also used to obtain elemental maps with greater precision and resolution. Four polished thin sections from core hole ERC14-002 were analyzed using the JEOL 8900 Electron Probe Microanalyzer (EPMA) at the University of Nevada, Las Vegas to better characterize silver deportment in the oxide, mixed, and sulfide zones.

Grain mounts from Vikre's (1977, 1981) work in the Rochester district were also examined. The grain mounts were prepared from high-grade heavy metal concentrates from both the oxide and mixed oxide-sulfide zones from historic workings at Nenzel Hill, which were removed during open pit mining. Four samples were examined in reflected light and three of those were selected for SEM analysis. Ten polished thin sections were also made from high grade drilling intercepts in other drill holes, two from core hole 9712C and eight from reverse circulation (RC) chips collected from six different drill holes (AR15-057, AR15-059, ER14-001, ER14-010, ER14-032, SF14-035), ranging in grade from 10.6 to 23.5 opt Ag. From these, five polished thin sections were examined and analyzed using the SEM.

Specific gravity measurements were employed to identify differences in density across the oxide, mixed, and sulfide weathering zones. This was done by weighing a sample dry then attaching it to a triple beam balance with wire and submerging it in a 5-gallon bucket filled with water to obtain the mass of displaced water. Specific gravity was determined for 25 samples selected from core hole ERC14-002 to represent varying weathering zones and silver grades.

Samples from ERC14-002 were analyzed for supergene clays, that is alteration products from acidic meteoric fluids. A total of 29 samples from the oxide, mixed, and sulfide weathering zones in ERC14-002 were analyzed using the ASD Terraspec Spectrometer to make preliminary identifications of various clay and sulfate minerals using SWIR reflectance spectroscopy. Identification of SWIR spectra can be imprecise in samples with intergrown mineral mixtures.

IV. Mineralization

Hypogene Mineralization - Sulfide Zone

Drill holes were typically terminated a short distance within the hypogene sulfide zone due to low silver grades and poor silver recovery, resulting in a paucity of available sulfide ore samples in the Rochester Formation. The Weaver Formation is partially to completely oxidized everywhere; therefore, no hypogene Weaver sulfide ore unaffected by weathering was available. Consequently, petrographic descriptions of hypogene mineralization is limited to the Rochester formation, and is based on Vikre (1977; 1981), and five low- and high-grade sulfide samples examined in this study.

Hypogene silver mineralization occurs as disseminated sulfides and in quartz veins. The predominant alteration assemblage is texture destructive and composed of quartz+sericite+pyrite±rutile. Two stages of quartz veining were reported by Vikre (1977; 1981). Stage 1 consists of coarse-grained, euhedral comb-textured quartz+K-feldspar+sulfide veins with widths from 1 mm to 4 cm with sharp, straight walls, making up 1 to 5% of the rock. Stage 1 veins contain coarse

sulfides with up to 20% pyrite, 15% sphalerite, 5% galena, and 1% chalcopyrite (see Table 1 for chemical formulas). Historic ore production came exclusively from stage 2 veins, which consist of quartz+K-feldspar+sericite+sulfide+sulfosalt, largely filling fault zones occasionally >3 m thick but more commonly seen today cutting wallrock 1 to 15 mm thick. Historically, stage 2 veins had combined strike lengths of 450 m and dip extents of up to 550 m. Vein alteration envelopes consist of quartz+sericite±K-feldspar extending up to a centimeter from veinlets, often obscuring where one envelope stops and the next one starts. Veins have indistinct walls often grading into hydrothermal microbreccias with fragments of rhyolite wall rocks. Stage 2 quartz veinlets and stringers make up 1 to 5% of the rock with local vein density up to 20%. Stage 2 veins were reported to cut stage 1 veins in old workings (Vikre, 1977; 1981).

Pyrite is the predominant sulfide making up more than 95 percent of all sulfides. Sphalerite, tetrahedrite, arsenopyrite, chalcopyrite, and galena make up most of the remaining sulfides. Pyrrhotite, teallite, and owyheeite are exceptionally rare. Pyrrhotite is almost completely replaced by pyrite and sphalerite. Arsenopyrite and pyrrhotite appear to have formed early in the sulfide paragenesis. Vikre (1977; 1981) reports silver-bearing tetrahedrite as the most significant hypogene silver-bearing ore mineral and occurs in both veins and disseminated ore. Acanthite occurs as discrete grains (Fig. 7D) and inclusions in pyrite (Fig. 8C) within veins and wallrock. Electrum is a very minor constituent contributing to silver grade. Unweathered veins account for no more than 15% of the overall silver content (Vikre, 1981).

Disseminated ore is largely made up of sulfides occurring in aggregates in a quartz+sericite groundmass. There are at least two generations of disseminated pyrite— euhedral to subhedral arsenian pyrite with sulfide inclusions and non-arsenian euhedral pyrite without inclusions. Sphalerite is the second most abundant sulfide and always appears to be later than pyrite. Arsenopyrite, chalcopyrite, and molybdenite are found as inclusions in both sphalerite and

Table 1. Minerals associated with hypogene and supergene ore at Rochester.

MINERAL/GROUP	FORMULA	OCCURRENCE
<u>SULFIDES</u>		
Pyrite	FeS ₂	hypogene
Sphalerite	ZnS	hypogene , supergene
Galena	PbS	hypogene
Tetrahedrite	(Cu,Fe,Ag,Zn) ₁₂ Sb ₄ S ₁₃	hypogene
Tennantite	(Cu,Fe,Ag,Zn) ₁₂ As ₄ S ₁₃	hypogene
Chalcopyrite	CuFeS ₂	hypogene
Arsenopyrite	FeAsS	hypogene
Molybdenite	MoS ₂	hypogene
Polybasite	Cu(Ag,Cu) ₆ Ag ₉ Sb ₂ S ₁₁	hypogene?
Pyrrhotite	FeS	hypogene
Teallite	PbSnS ₂	hypogene
Owyheeite	Ag ₃ Pb ₁₀ Sb ₁₁ S ₂₈	hypogene
Stromeyerite	AgCuS	hypogene, supergene
Acanthite	Ag ₂ S	hypogene, supergene
Pearceite	Cu(Ag,Cu) ₆ Ag ₉ As ₂ S ₁₁	supergene?
Proustite	Ag ₃ AsS ₃	supergene
Stephanite	Ag ₅ SbS ₄	supergene
Miargyrite	AgSbS ₂	supergene
Jalpaite	Ag ₃ CuS ₂	supergene
Covellite	CuS	supergene
Chalcocite	Cu ₂ S	supergene
Imiterite	Ag ₂ HgS ₂	supergene
<u>HALIDES</u>		
Chlorargyrite	AgCl	supergene
Iodargyrite	AgI	supergene
Iltisite	HgAgS(Cl,Br)	supergene
<u>OXIDES</u>		
Goethite	FeO(OH)	supergene
Jarosite	KFe ₃ (SO ₄) ₂ (OH) ₆	supergene
Hematite	Fe ₂ O ₃	supergene
Valentinite	Sb ₂ O ₃	supergene
Plattnerite	PbO ₂	supergene
Bindheimite	Pb ₂ Sb ₂ O ₆ (O, OH)	supergene
Chalcophanite	(Zn,Fe,Mn)Mn ₃ O ₇ ·3H ₂ O	supergene
<u>SULFATES</u>		
Anglesite	PbSO ₄	supergene
Chalcanthite	CuSO ₄ ·5H ₂ O	supergene
Melanterite	FeSO ₄ ·7H ₂ O	supergene
<u>CARBONATES</u>		
Malachite	Cu ₂ (CO ₃)(OH) ₂	supergene

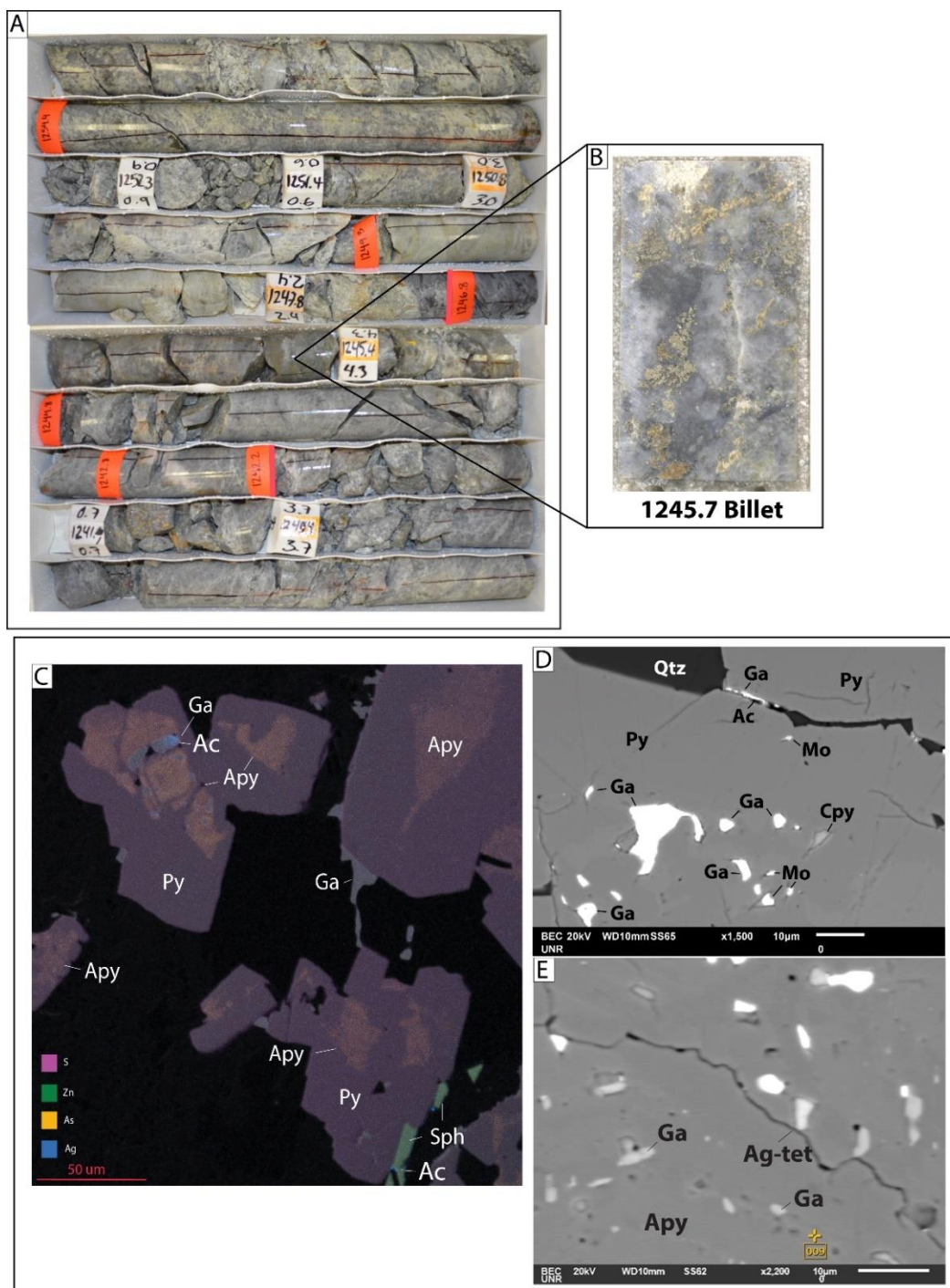


Figure 7. Core hole ERC14-002 from the Rochester Formation sulfide zone. **A.** Sample interval 1242.2-1248.6 ft, assayed 0.59 opt Ag and 0.003 opt Au. **B.** Thin section billet of sample 1245.7 ft. **C.** Microprobe WDS elemental image showing late acanthite (Ac) as the dominant silver phase with early arsenopyrite (Apy), pyrite (Py), and late sphalerite (Sph) and galena (Ga). **D.** SEM image of sample 790.2 ft showing late acanthite-galena-quartz (Qtz) veinlet cutting pyrite. Galena, molybdenite (Mo), and chalcopyrite (Cpy) inclusions are shown in pyrite. **E.** SEM image from 790.2 ft showing silver-bearing tetrahedrite (Ag-tet) and galena inclusions in arsenopyrite.

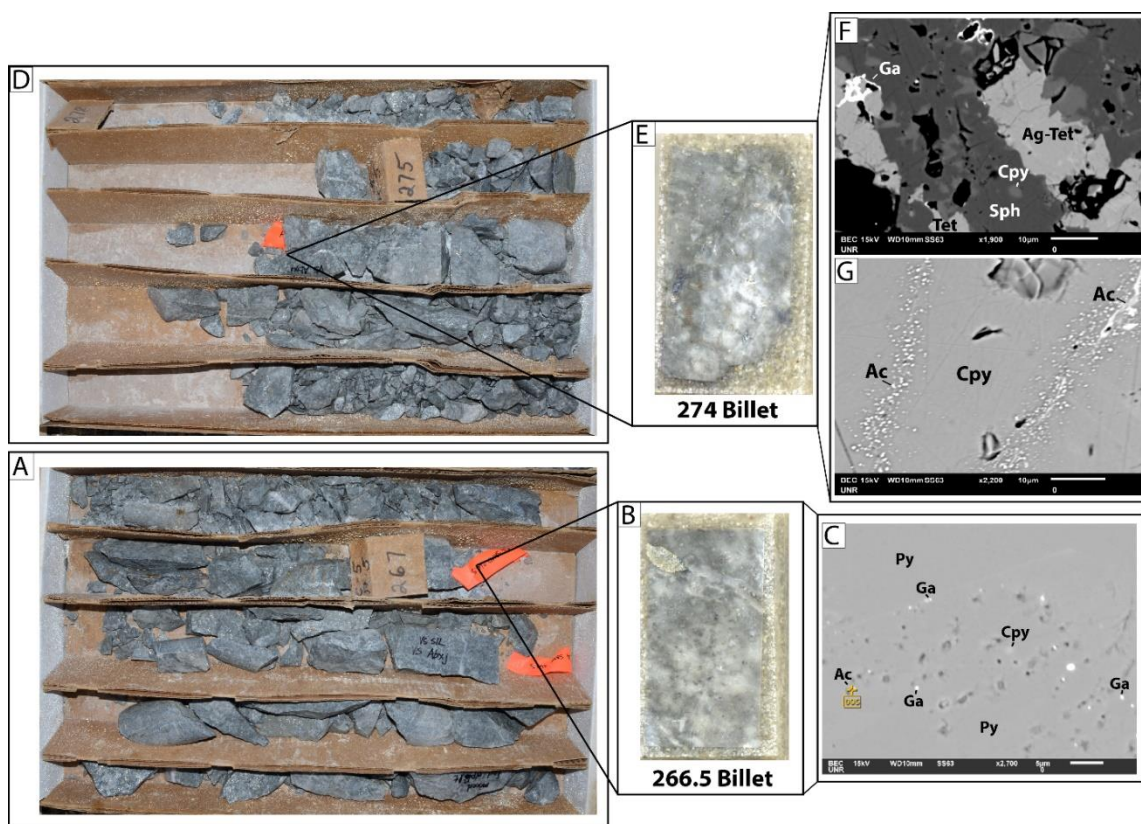


Figure 8. Core hole R07-03 from the Rochester Formation sulfide zone. **A.** Sample interval 265-270 ft, assayed 0.44 opt Ag and 0.011 opt Au. **B.** Thin section billet of sample 266.5 ft. **C.** SEM BSE image from 266.5 showing acanthite (Ac), galena (Ga), and chalcopyrite (Cpy) occurring in pyrite (Py) in a quartz veinlet. **D.** Interval 270-275 ft, assayed 0.5 opt Ag and 0.003 opt Au. **E.** Thin section billet of sample 274 ft. **F.** SEM BSE image from 274 ft showing silver-bearing tetrahedrite intergrown with chalcopyrite, sphalerite, and galena. **G.** SEM BSE image from sample 274 ft showing acanthite stringers cutting chalcopyrite.

pyrite (Fig. 7), and occur as discrete grains. Minor chalcopyrite disease occurs in sphalerite indicating some chalcopyrite crystallized concurrently with sphalerite or exsolved from solid solution (Fig. 9B). Galena most often rims and cuts sphalerite (Fig. 9B) and pyrite, but also occurs as inclusions in pyrite (Fig. 7, 8C). Minor barite is also present in disseminated ore and pyrite veinlets.

Argentiferous tetrahedrite-tennantite and acanthite are the most important silver phases in disseminated ore. Hypogene argentiferous tetrahedrite-tennantite occurs as discrete grains, inclusions in pyrite (Fig. 7), and locally replaces chalcopyrite (Fig. 10). Interpreted hypogene

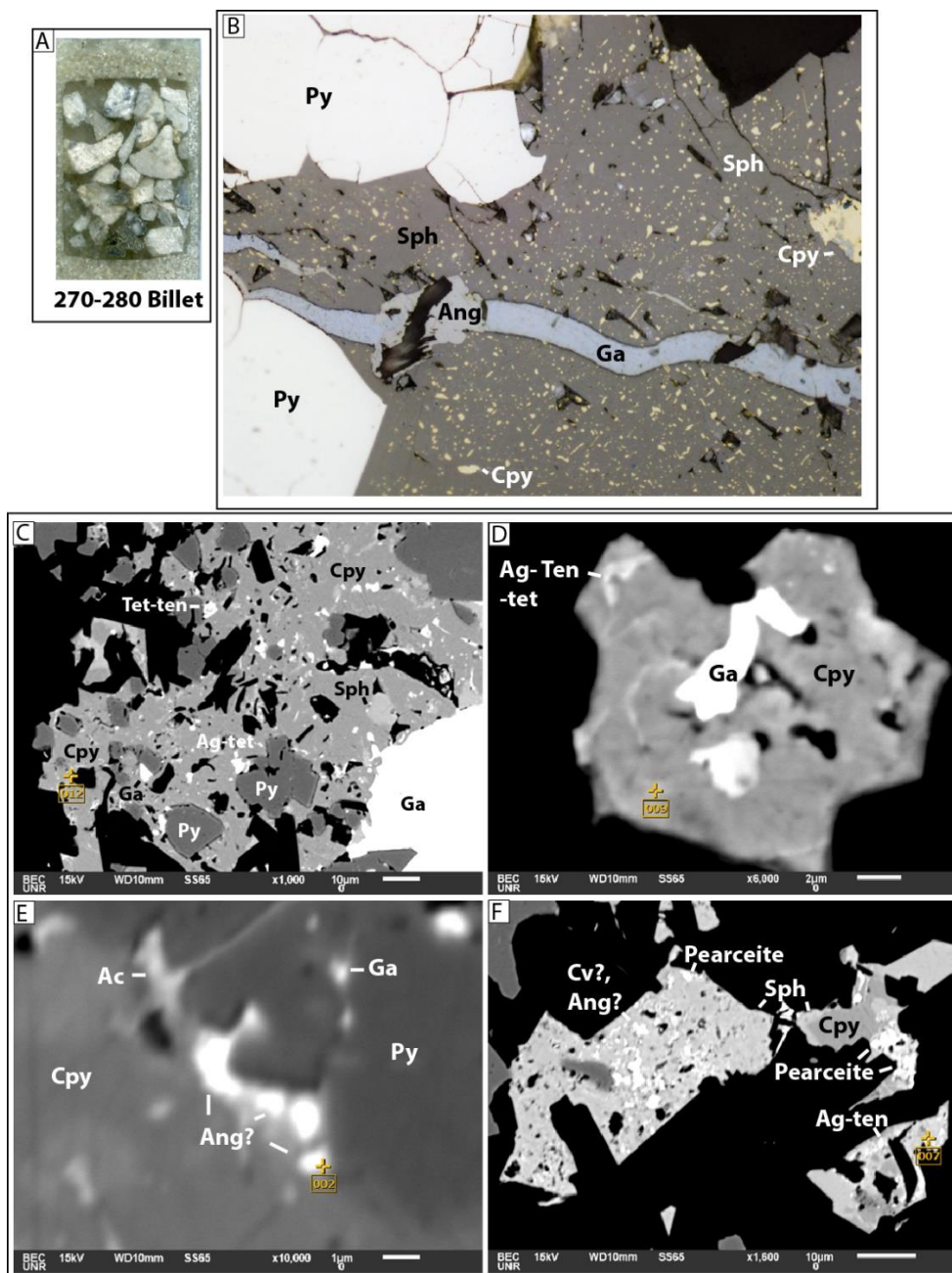


Figure 9. RC hole AR15-057 from the Rochester Formation sulfide zone. **A.** Thin section billet of sample 270-280 ft. This interval assayed 11.1 opt Ag and 0.245 opt Au. **B.** Reflected light photo showing a veinlet of galena (Ga) locally oxidized to anglesite (Ang) cutting sphalerite (Sph) with chalcopyrite “disease” that envelops pyrite (Py). **C.** SEM BSE image showing silver-bearing tetrahedrite (Ag-tet) with pyrite, chalcopyrite, galena, sphalerite, and tetrahedrite-tennantite. **D.** SEM BSE image showing silver-bearing tetrahedrite-tennantite with chalcopyrite and galena. **E.** SEM BSE image showing acanthite (Ac) and anglesite(?) along the grain boundary between pyrite and chalcopyrite, that likely formed by oxidation of a late hypogene galena. **F.** SEM BSE image showing pearceite with sphalerite and chalcopyrite. Late supergene covellite(?) (Cv) and anglesite(?) are also present.

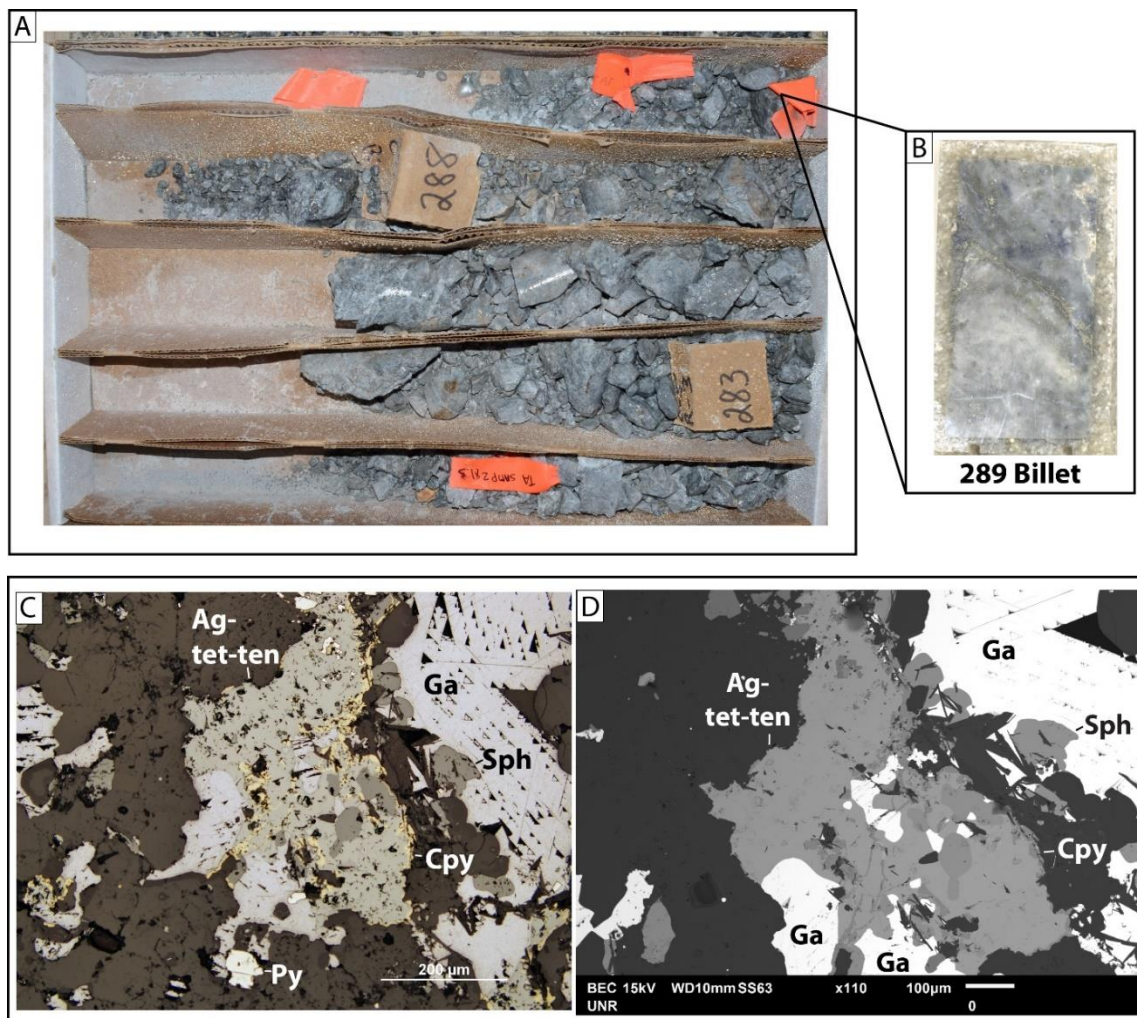


Figure 10. Core hole R07-03 from the Rochester Formation sulfide zone. **A.** Sample interval from 285-290 ft, assayed 4.8 opt Ag and 0.047 opt Au. **B.** Thin section billet of sample 289 ft. **C.** Reflected light photo from sample 289 showing silver-bearing tetrahedrite-tennantite (Ag-tet-ten) replacing chalcopyrite (Cpy). **D.** SEM BSE image of the same reflected light photograph showing silver-bearing tetrahedrite-tennantite with galena (Ga) and sphalerite (Sph).

acanthite occurs along arsenian growth zones in pyrite, discrete grains, and locally cuts chalcopyrite (Fig. 8G). Vikre (1977; 1981) separated optically pure wallrock pyrite from other sulfides and found these pyrites contain 68 to 330 ppm Ag occurring either cryptically in the pyrite crystal structure or in optically unresolvable inclusions. From these data Vikre estimated wallrock pyrite contained up to 5% of the overall silver in the Rochester deposit. Acanthite locally occurs with anglesite (PbSO_4) in the sulfide zone, indicative of incipient oxidation (Fig.

9). Rare supergene(?) acanthite and sphalerite were found at high elevations of the sulfide zone rimming chalcopyrite (Fig. 11). Local silver phases include stromeyerite, pearceite (Fig. 9), and polybasite. Pearceite and polybasite were found occurring with other sulfides in RC chips, it is not clear if these silver phases are disseminated aggregates or in fragments of quartz veins.

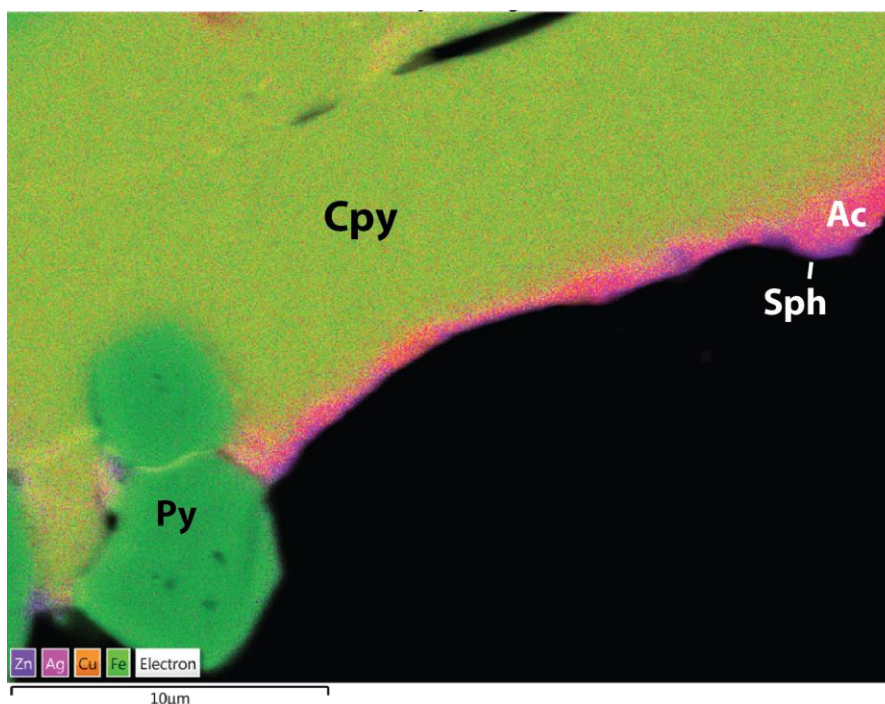


Figure 21. RC hole AR15-057 from the Rochester Formation sulfide zone. This sample interval assayed 11.1 opt Ag. SEM EDS layered elemental map showing acanthite (Ac) rimming chalcopyrite (Cpy) with later sphalerite (Sph) rim.

Supergene Mineralization - Oxide Zone

Silver mineralization in the oxide weathering zone is characterized mainly by goethite, acanthite, and chlorargyrite. Oxide zone samples are characterized by abundant exotic goethite>>hematite, and rare jarosite. Wallrock alteration is similar to the sulfide zone dominated by quartz with up to 50% sericite and <1 to 10% remnant K-feldspar variably altered to quartz±sericite±goethite. Minor supergene kaolinite and poorly crystalline sericite in post-

mineralized fault zones and on oxidized fractures, and rare halloysite were reported by Vikre (1977; 1981).

Oxide samples contain ~3% indigenous limonite (goethite > hematite), typically as disseminations that are locally clustered and in quartz veins and stringers (Fig. 12). Local relict pyrite occurs as disseminations and in quartz veinlets, typically no more than 0.5% but can be up to 3% of the sample in local sulfide pockets. Indigenous hematite is more common when remnant pyrite is present (Fig. 13E).

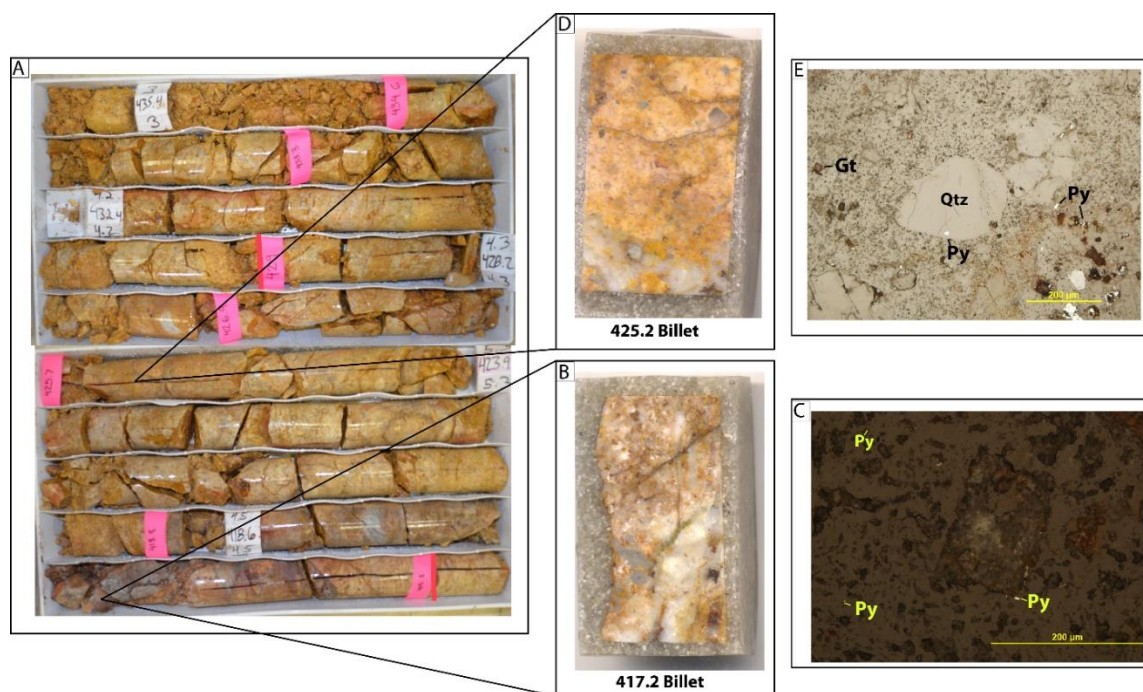


Figure 12. Core hole ERC14-002 from the Weaver Formation oxide zone. **A.** Sample interval 415.8-429 ft, assayed 0.35 opt Ag and 0.003 opt Au. **B.** Sample 417.2 thin section billet. **C.** Sample 417.2 in reflected light showing fine-grained pyrite (Py) disseminated in quartz+sericite+goethite groundmass. **D.** Sample 425.2 thin section billet. **E.** Reflected light photo of sample 425.2 showing fine-grained remnant pyrite variably oxidized to goethite (Gt).

Acanthite is the dominant silver-bearing phase occurring mostly as disseminated grains that range in size from one to 20 microns. Goethite and acanthite commonly occur as incipient weathering on the rims of pyrite (Fig. 14B, 15, 16C). Similarly, proustite and hematite occur with acanthite as concentric rims on pyrite (Fig. 17). Where pyrite is completely weathered to

goethite, acanthite is found as inclusions and rims on goethite (Fig. 14, 18, 19C, 20). The second most common silver phase is chlorargyrite (Fig. 16D), which commonly occurs with acanthite

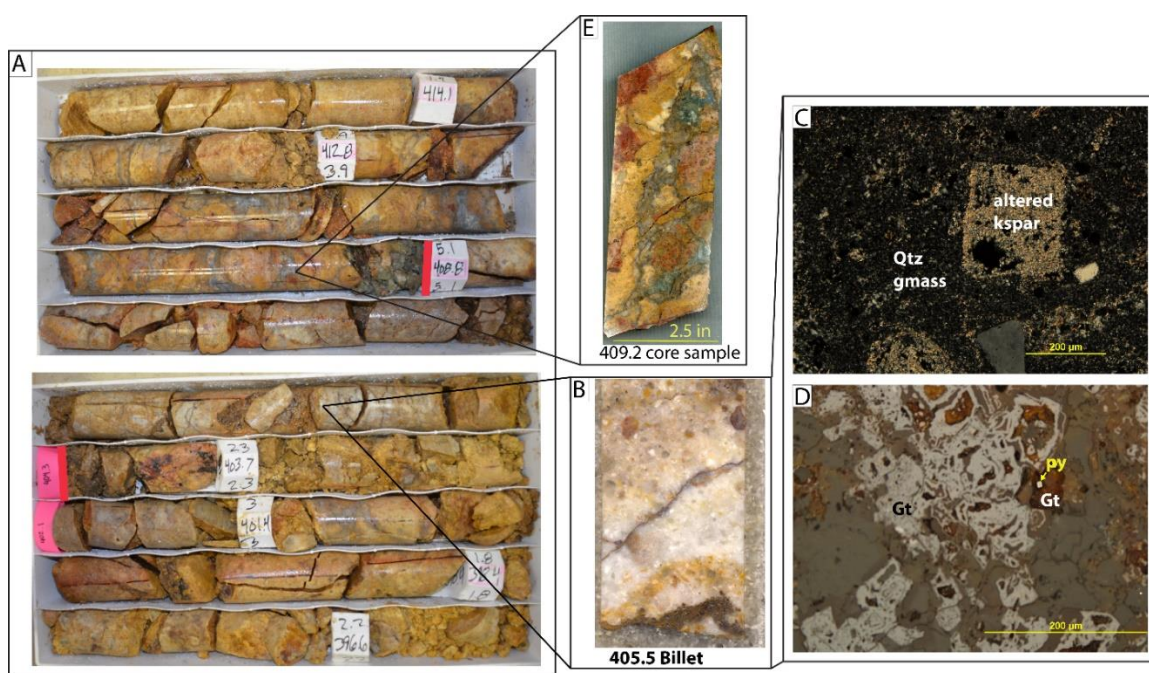


Figure 13. Core hole ERC14-002 from the Weaver Formation oxide zone. **A.** Sample interval 404.3-408.8 ft, assayed 0.85 opt Ag and 0.002 opt Au. **B.** Sample 405.5 thin section billet. **C.** Transmitted light photo showing K-feldspar altered to sericite and quartz and the groundmass altered to quartz. **D.** Reflected light photo showing relict pyrite (Py) surrounded by goethite (Gt). **E.** Sample 409.2 from assay interval 408.8-414.1 ft that assayed 3.36 opt Ag.

and goethite (Fig. 21). Other mineral phases associated with chlorargyrite and acanthite include iodargyrite, native silver, imiterite, iltisite (Fig. 21 and 22), stephanite (Fig. 15), proustite (Fig. 20D), jalpaite (Figure 17C), antimonial-silver and antimony-oxide (valentinite?) and lead-oxides (plattnerite?) (Fig. 20B, D). Schrader (1914) reported abundant bindheimite in hand samples of ore. Vikre (1977) noted the likelihood of additional unidentified antimony, lead, and zinc oxides. Very rare covellite was identified in the oxide zone. Minor native gold occurs with acanthite (Fig. 20E). Barite locally occurs as rims on goethite, along with minor copper-oxides (malachite?) suggesting it formed in the later stages of oxidation. Vikre (1977; 1981) reported minor amounts of chalcocite, chalcophanite, melanterite, and Mn-oxides.

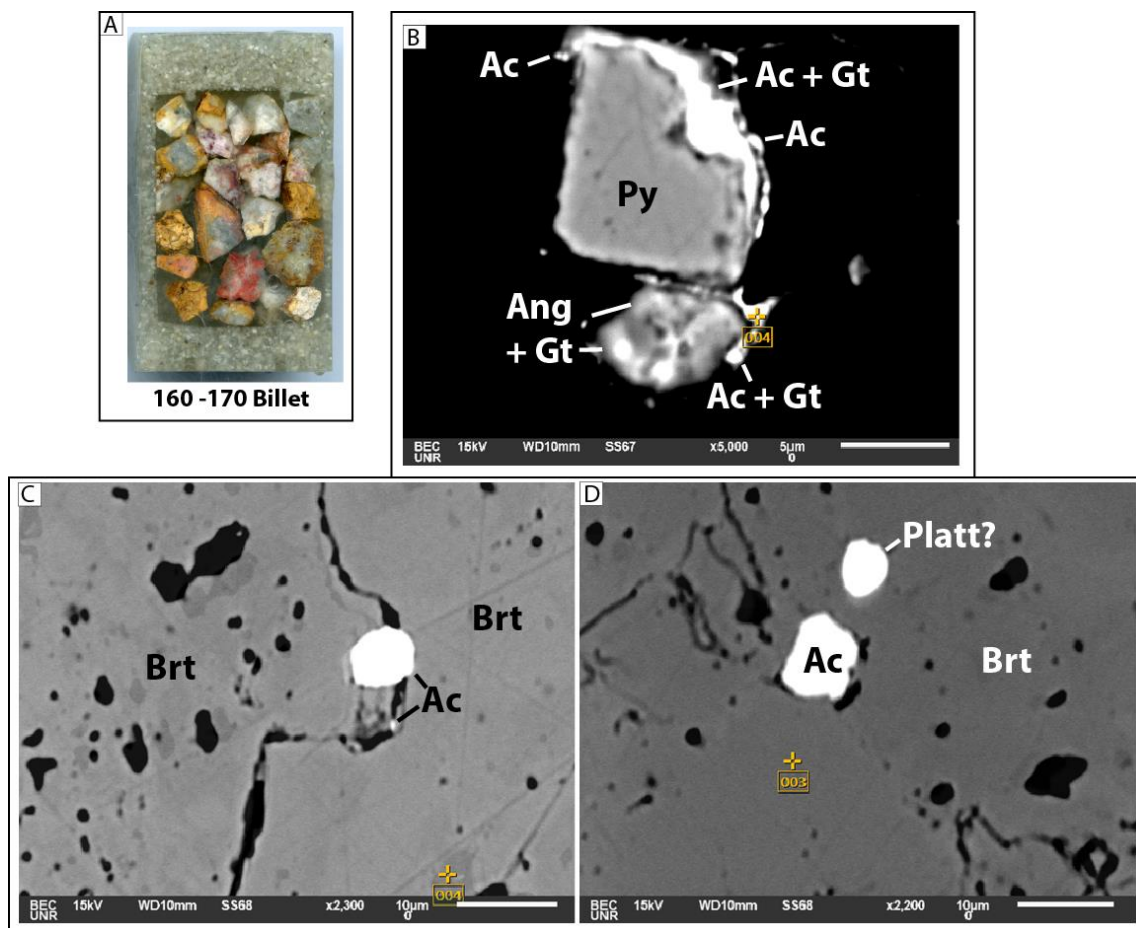


Figure 14. RC hole AR15-059 from the Rochester Formation oxide zone. **A.** Thin section billet from interval 160-170 ft, assayed 14.2 opt Ag and 0.012 opt Au. **B.** SEM BSE image showing pyrite (Py) oxidizing to goethite (Gt), which contains blebs of acanthite (Ac). Anglesite (Ang) plus goethite likely represents oxidizing of pyrite+galena. **C.** SEM BSE image showing acanthite along the grain boundary between barite (Brt). **D.** SEM BSE image showing acanthite and a lead-oxide phase (plattnerite?) in barite.

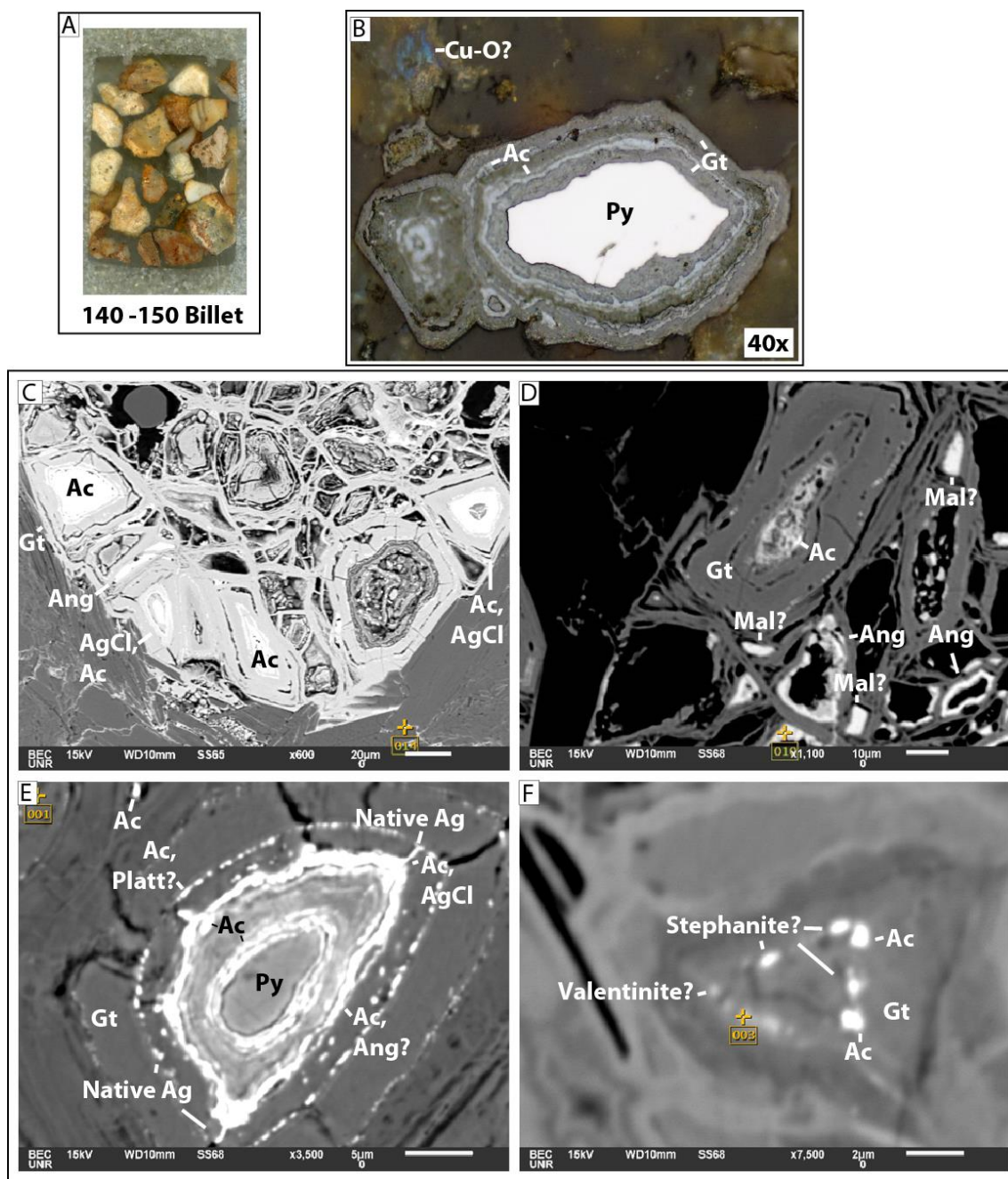


Figure 15. RC hole ER14-032 from the Weaver Formation oxide zone. **A.** Thin section billet from 140-150 ft interval that assayed 23.48 opt Ag and 0.236 opt Au. **B.** Reflected light photo showing pyrite weathering to goethite with layers of acanthite. There is also a bright blue-purple mineral in the left corner, possibly a copper oxide phase. **C.** SEM BSE image showing acanthite (Ac), chlorargyrite (AgCl), and anglesite (Ang) surrounded by goethite (Gt). **D.** SEM BSE image showing acanthite, malachite(?) (Mal), and anglesite surrounded by goethite. **E.** SEM BSE image showing a pyrite grain oxidizing to acanthite and goethite. Native Ag, chlorargyrite, plattnerite (Platt), and anglesite are also present. **F.** SEM BSE image showing acanthite, stephanite, and valentinite as discrete grains in goethite.

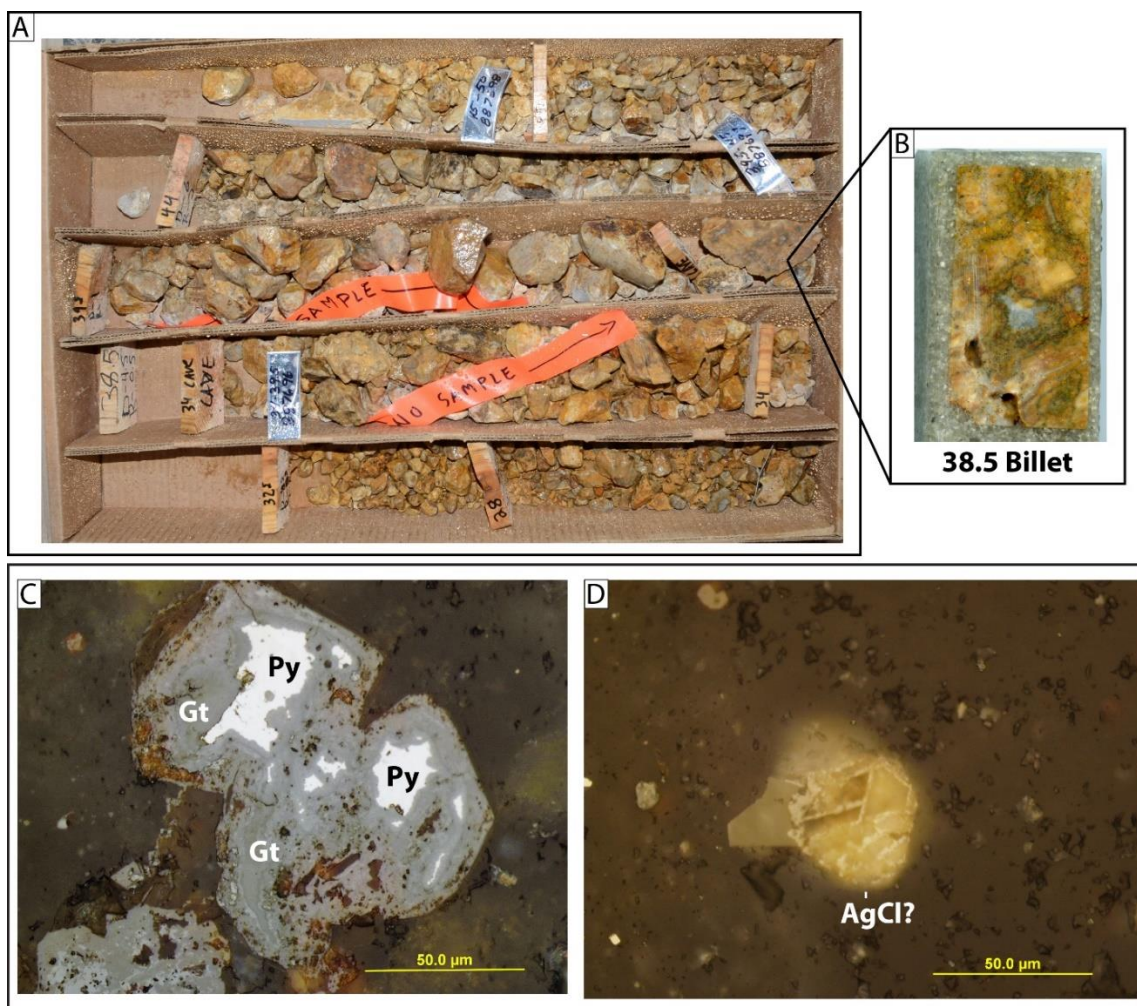


Figure 16. Core hole R11C-006 from the Weaver Formation oxide zone. **A.** Interval 34-39.5 ft, assayed 4.1 opt Ag and 0.003 opt Au. **B.** Thin section billet of sample 38.5 ft. **C.** Reflected light photo showing pyrite (Py) partially oxidized to goethite (Gt). **D.** Reflected light image showing chlorargyrite(?) (AgCl).

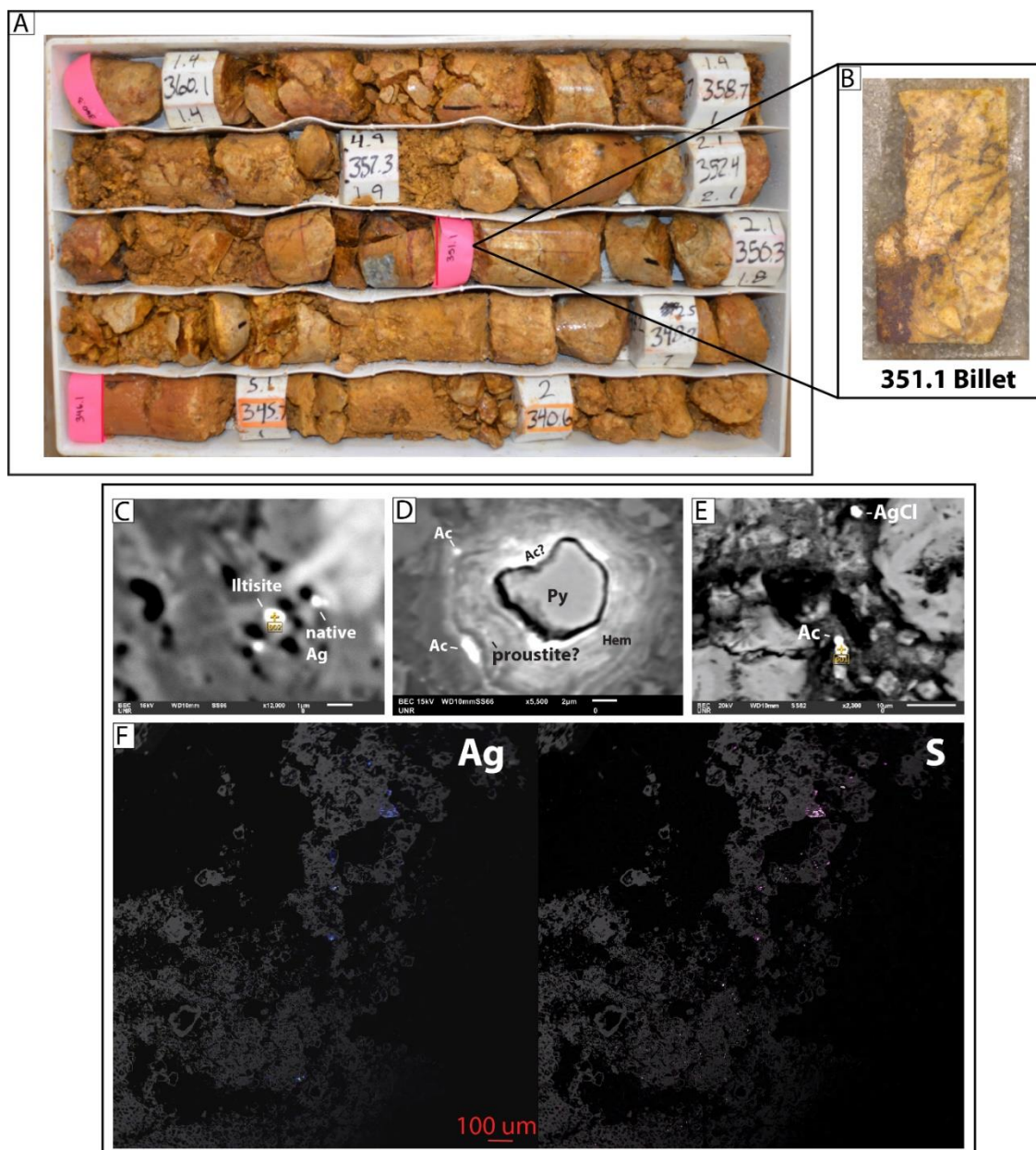


Figure 17. Core hole ERC14-002 from the Weaver Formation oxide zone. **A.** Sample interval 346.1-351.1 ft, assayed 3.94 opt Ag and 0.004 opt Au. **B.** Sample 351.1 thin section billet. **C.** SEM BSE image showing iltisite and native silver surrounded by oxidized gangue. **D.** A partially oxidized pyrite (Py) surrounded by multiple silver phases including acanthite (Ac) and proustite(?). **E.** SEM BSE image showing chlorargyrite and acanthite in gangue. **F.** Electron microprobe WDS map showing silver and sulfur phases in 351.1. Silver and sulfur largely occupy the same space suggesting acanthite is the predominant silver-bearing phase.

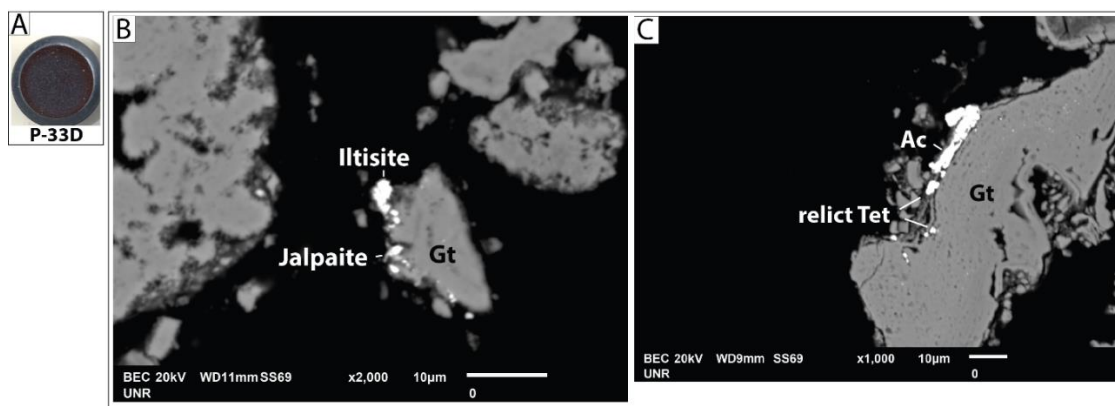


Figure 18. A. Grain mount P-33D from Vikre's (1977; 1981) work from the oxide zone containing no megascopic sulfides. B. SEM BSE image showing jalpaite and iltisite. C. SEM BSE image showing acanthite (Ac) and relict tetrahedrite (Tet) rimming goethite (Gt).

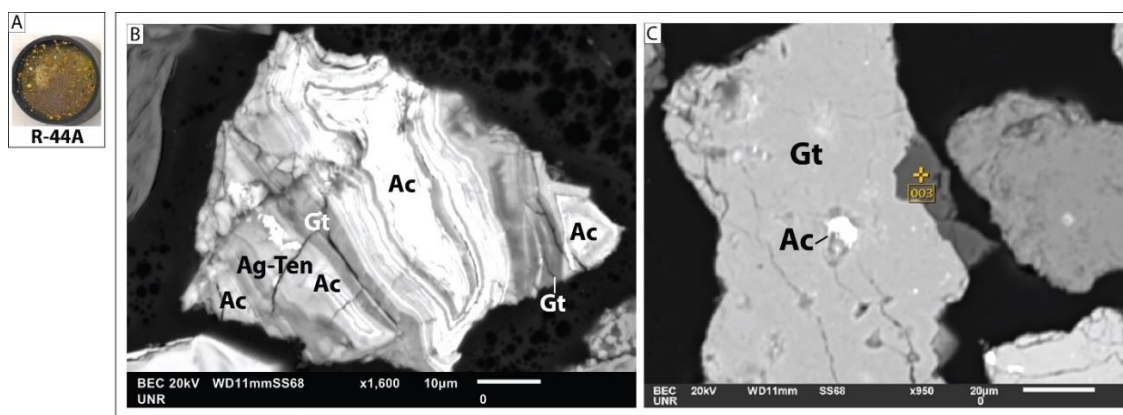


Figure 19. A. Grain mount R-44A from Vikre's (1977; 1981) work from the oxide zone. B. SEM BSE image showing tennantite (Ten) and acanthite (Ac) partially oxidized to goethite. C. SEM BSE image showing acanthite surrounded by goethite.

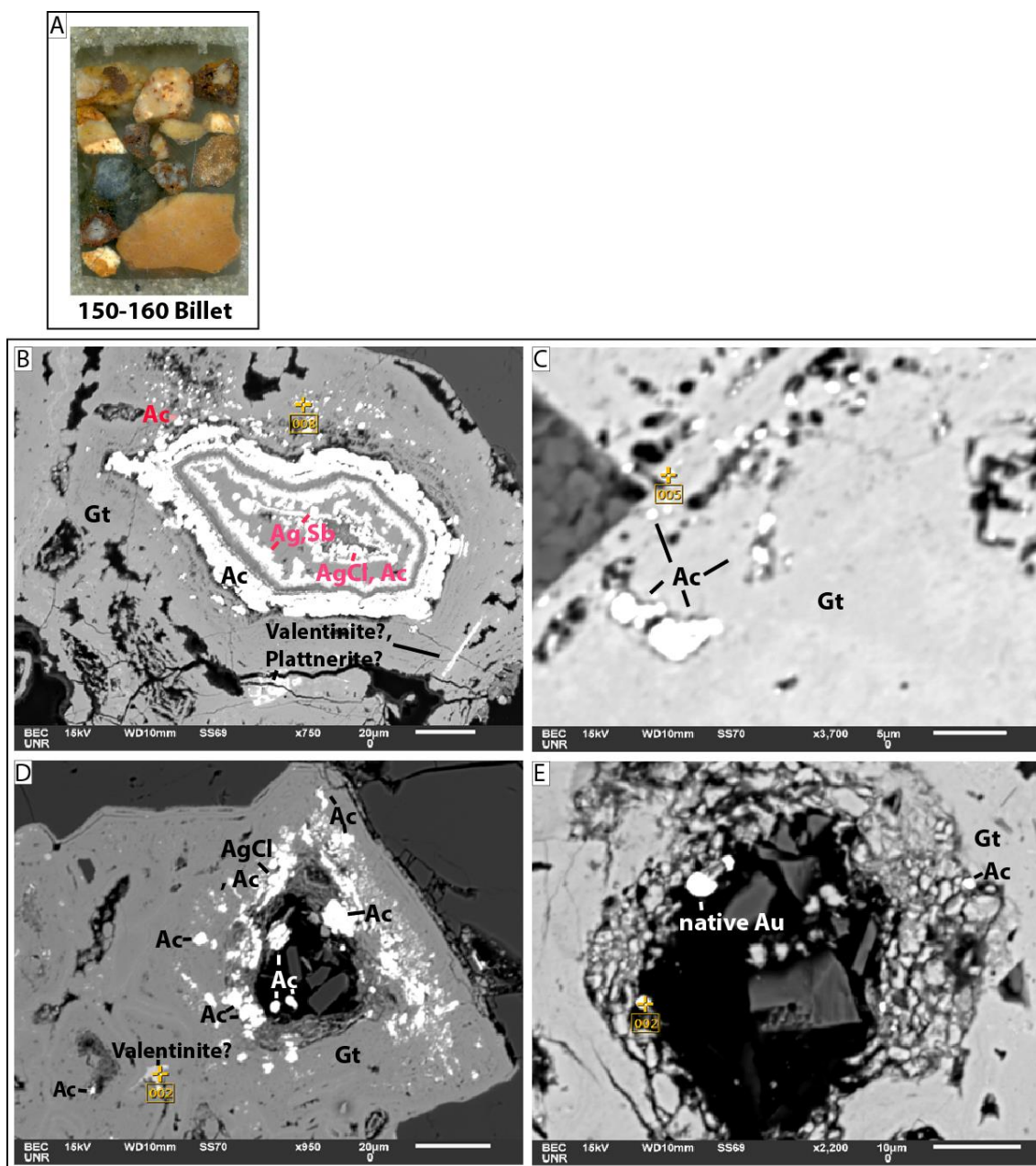


Figure 20. RC hole ER14-010 from the Weaver Formation oxide zone. **A.** Thin section billet from 150-160 ft interval that assayed 16.98 opt Ag and 1.563 opt Au. **B.** SEM BSE image showing acanthite (Ac) rimming an oxidized grain where antimonial-silver (Ag, Sb), chlorargyrite (AgCl), and acanthite occur. Valentinite? and plattnerite(?) are also present. **C.** SEM BSE image showing discrete acanthite grains surrounded by goethite (Gt). **D.** SEM BSE image showing acanthite and minor chlorargyrite grains in goethite. Valentinite(?) is also present. **E.** SEM BSE image showing a native gold (Au) grain and acanthite with goethite.

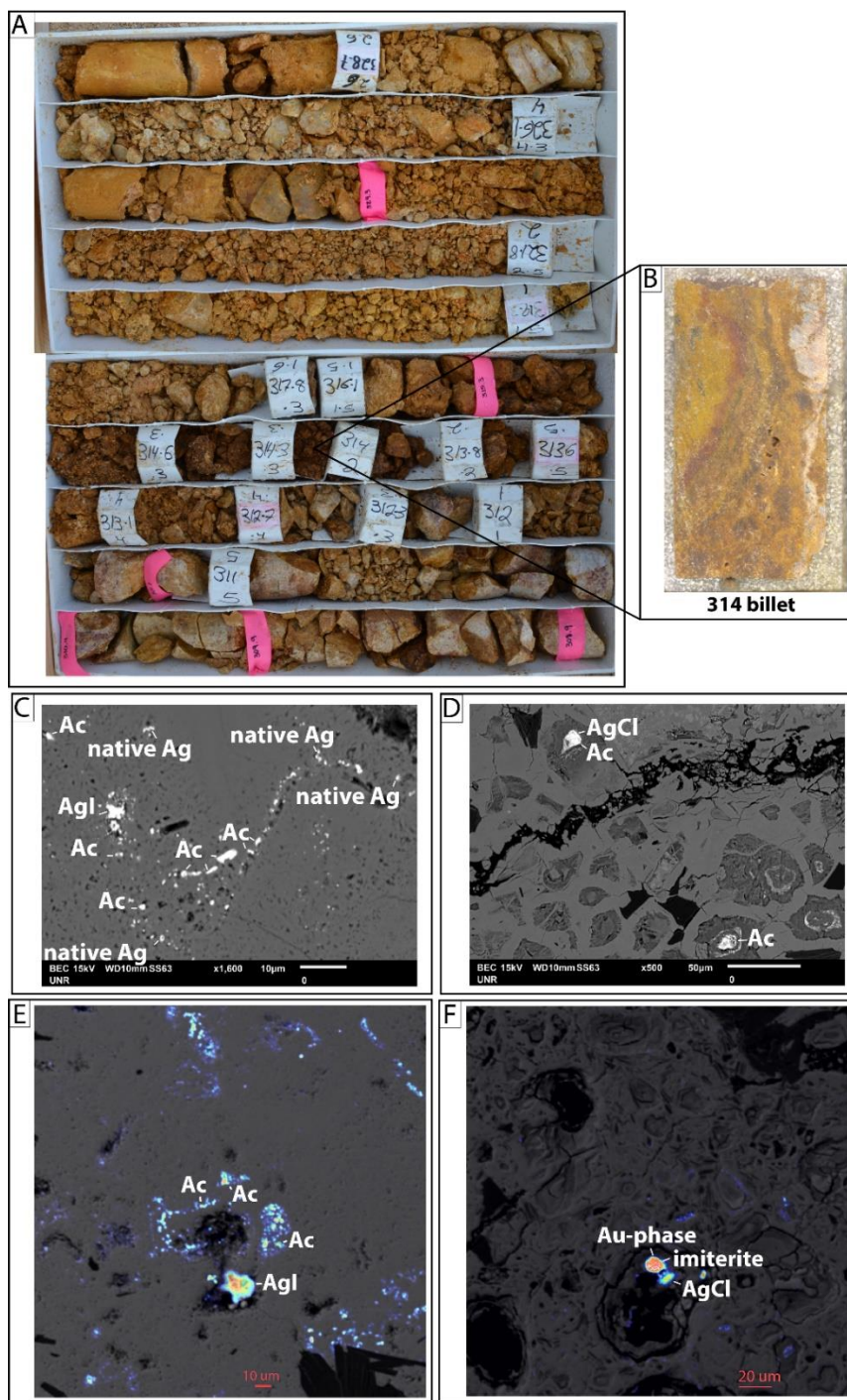


Figure 21. Core hole ERC14-002 from the Weaver Formation oxide zone. **A.** Sample interval from 310.9-329 ft, assayed 2.99 opt Ag and 0.009 opt Au. **B.** Thin section billet from 314 ft. **C.** SEM BSE image showing acanthite (Ac) as the dominant silver phase, iodargyrite (AgI), and native silver. **D.** SEM BSE image showing acanthite and chlorargyrite closely intergrown. **E.** Electron microprobe WDS elemental map of silver showing acanthite and iodargyrite. **F.** Electron microprobe WDS elemental map of silver showing imiterite, chlorargyrite, and a gold-phase closely intergrown.

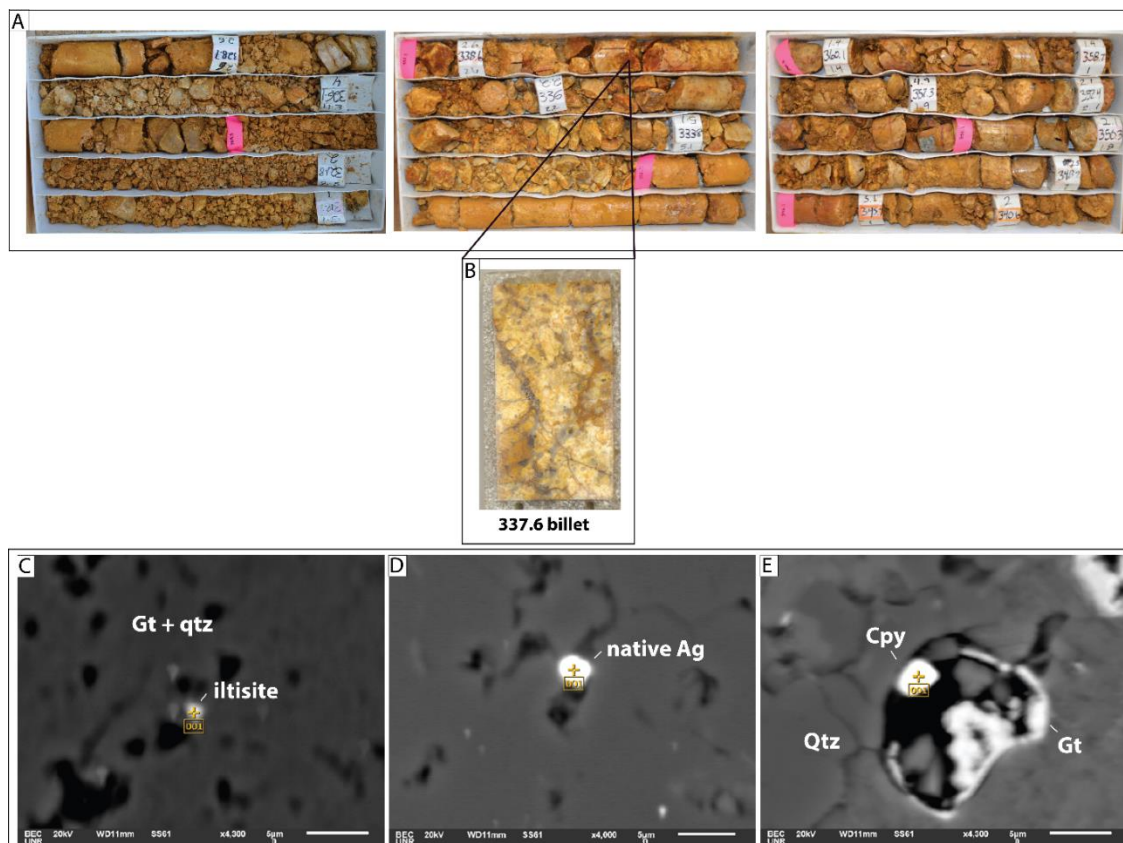


Figure 22. Core hole ERC14-002 from the Weaver Formation oxide zone. **A.** Sample interval 329-346.1 ft, assayed 1.57 opt Ag and 0.005 opt Au. **B.** Sample 337.6 thin section billet. **C.** SEM BSE image showing iltisite (based on SEM EDS analysis) surrounded by goethite (Gt) and quartz (Qtz). **D.** SEM BSE image showing native silver surrounded by gangue. **E.** SEM BSE image showing chalcopyrite (Cpy) and goethite (Gt) partially in a cavity.

Supergene Mineralization - Mixed Zone

High-grade silver mineralization also occurs along the boundary between the oxide and mixed oxide-sulfide weathering zones. Some of the highest silver grades (71 opt Ag) from this study occur in the mixed zone (Fig. 23). The mixed oxide-sulfide weathering zone is characterized by common pockets of unweathered hypogene sulfides that range up to several feet in diameter surrounded by exotic limonite (goethite>>hematite). The alteration and quartz veining is the same as the sulfide zone (Fig. 24 and 25). Kaolinite locally occurs along fractures in pit exposures. Laths of alunite locally occur with hematite (Fig. 26C).

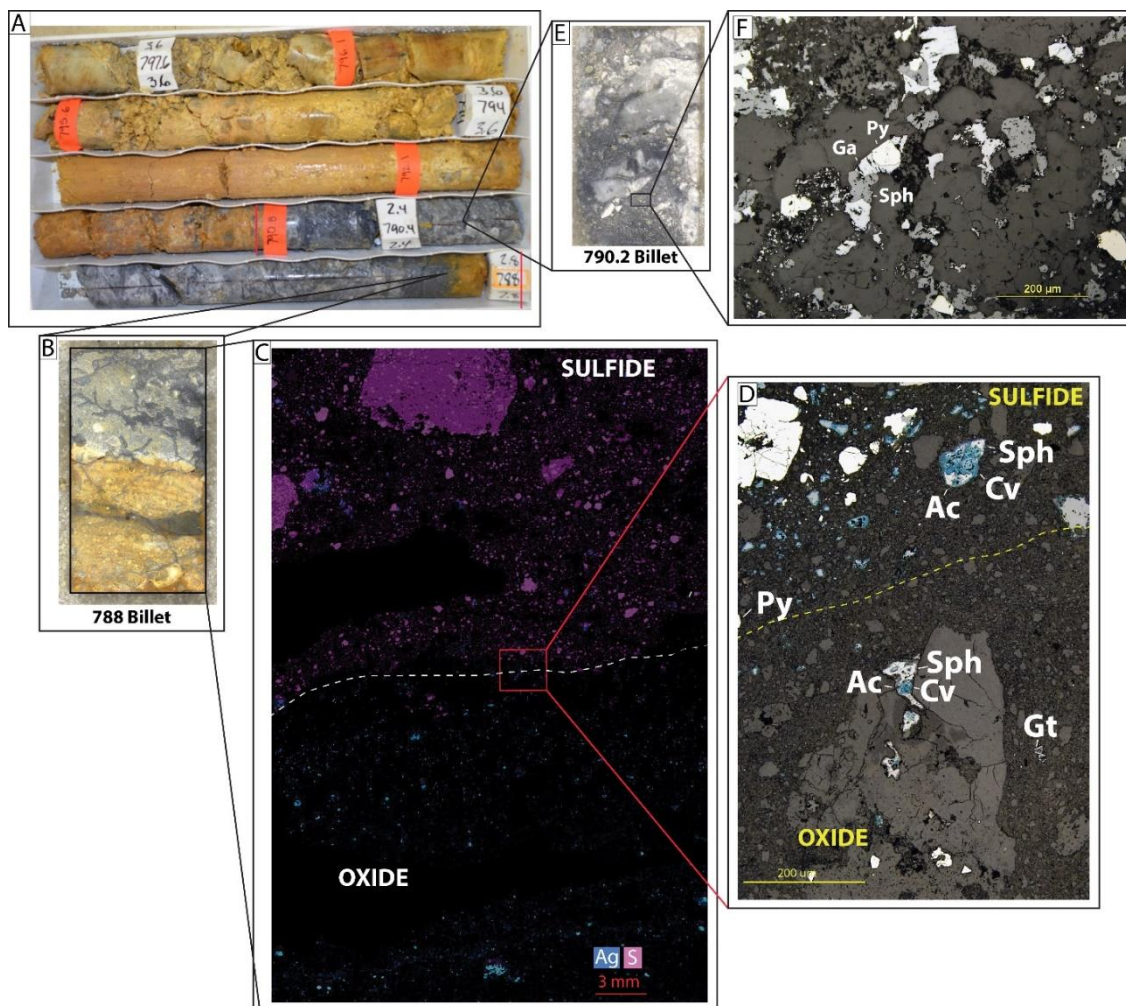


Figure 23. Core hole ERC14-002 from the Rochester Formation mixed zone. **A.** Sample interval 788-790.8 ft, assayed 71.92 opt Ag and 0.113 opt Au, the highest grade assay in ERC14-002. **B.** Sample 788 thin section billet. **C.** Microprobe elemental WDS map of 788 depicting silver and sulfur occurrences. **D.** Reflected light photo of 788 showing covellite (Cv) and acanthite (Ac) rimming sphalerite (Sph) in the sulfide and oxide portion of the thin section. **E.** Sample 790.2 thin section billet. **F.** Reflected light photo of 790.2 showing apparent contemporaneous galena (Ga), pyrite (Py), and sphalerite.

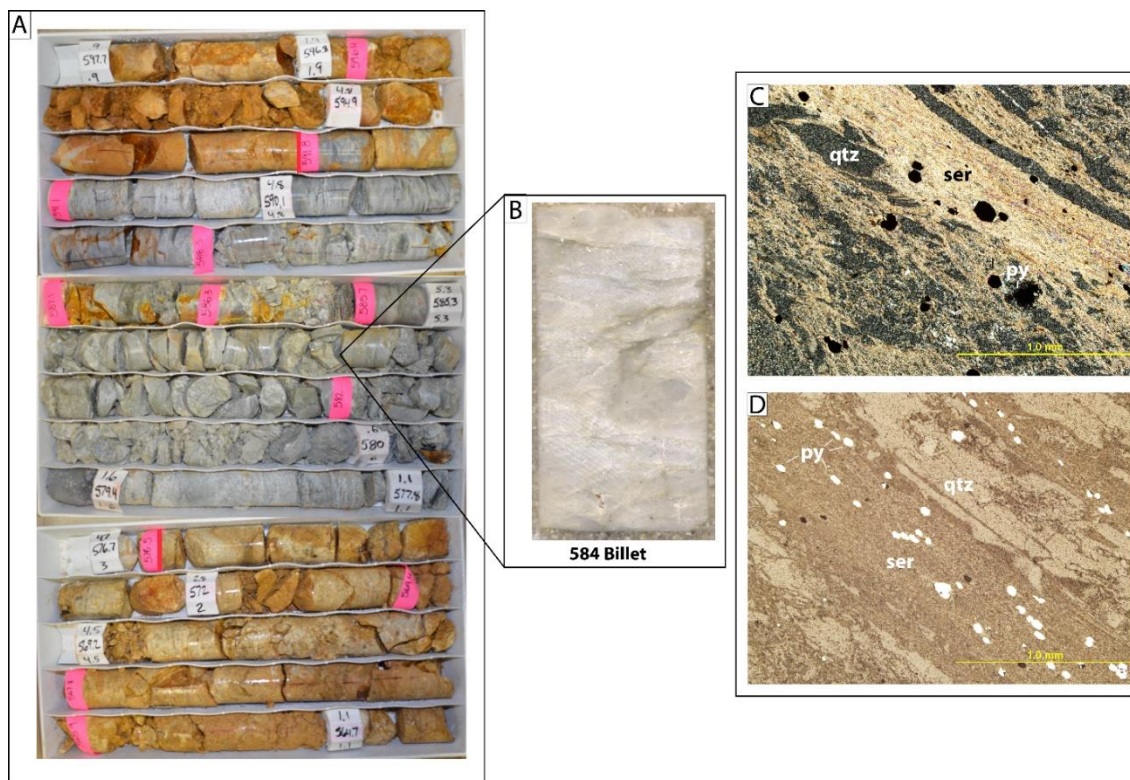


Figure 24. Core hole ERC14-002 from the Rochester Formation mixed zone. **A.** Sample interval 576.5-591.8 ft, assayed 0.12 opt Ag and 0.0006 opt Au. **B.** Sample 584 thin section billet. **C.** Transmitted light photo from sample 584 showing bands of sericite, quartz, and pyrite replacing groundmass. **D.** Reflected light photo of sample 584 showing replacement by sericite, quartz, and pyrite.

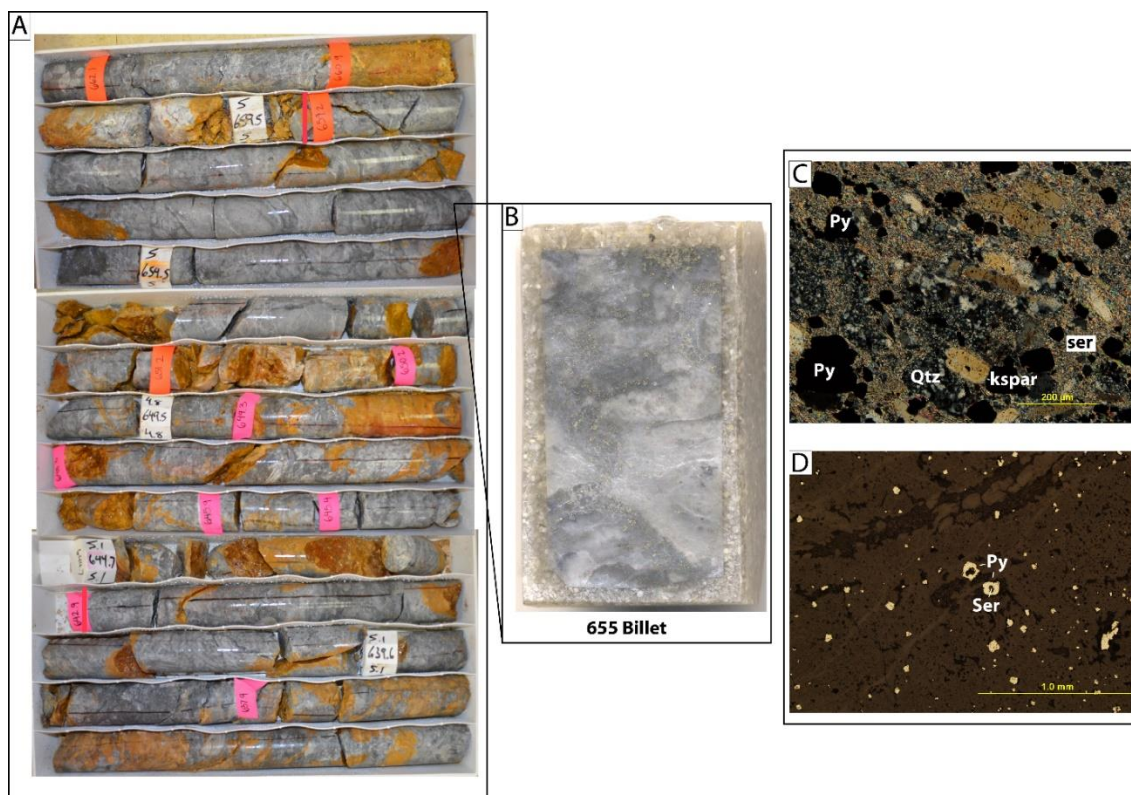


Figure 25. Core hole ERC14-002 from the Rochester Formation mixed zone **A.** Sample interval 642.9-659.2 ft, assayed 0.11 opt Ag and 0.001 opt Au. **B.** Sample 655 thin section billet. **C.** Transmitted light photo showing unoxidized quartz+sericite+pyrite alteration with remnant K-feldspar. **D.** Reflected light photo showing pyrite and sericite occurring together.



Figure 26. Core hole R11C-006 from the Rochester Formation mixed zone. **A.** Interval 1000-1010 ft assayed 2.6 opt Ag and 0.008 opt Au. **B.** Thin section billet of sample 1005.2 ft. **C.** Transmitted light photo from sample 1005.2 of alunite (Alun) and hematite (Hem). **D.** Reflected light photo from sample 1005.2 showing the yellow internal reflections of jarosite (Jar). **E.** Thin section billet of sample 1009.5 ft. **F.** Reflected light photo from sample 1009.5 showing euhedral pyrite rimmed and enveloped by aggregates of much finer grained subhedral pyrite (Py).

Hypogene sulfide pockets contain aggregates of <1 to 20% pyrite, arsenian pyrite, and minor sphalerite, galena, arsenopyrite, and chalcopyrite, along with trace molybdenite.

Chalcopyrite (<0.5%) and arsenopyrite mostly occur as inclusions in pyrite (Fig. 27C, 28).

Sphalerite locally makes up to 10% of samples. Galena (~1%) typically occurs after sphalerite and pyrite. Acanthite, described below, argentiferous tetrahedrite-tennantite, and rare

stromeyerite are the only hypogene silver phases. Argentiferous tetrahedrite-tennantite occurs mainly as individual grains (Fig. 29B) and inclusions in pyrite (Fig. 30). Barite also locally occurs with pyrite surrounded by sphalerite (Fig. 30).

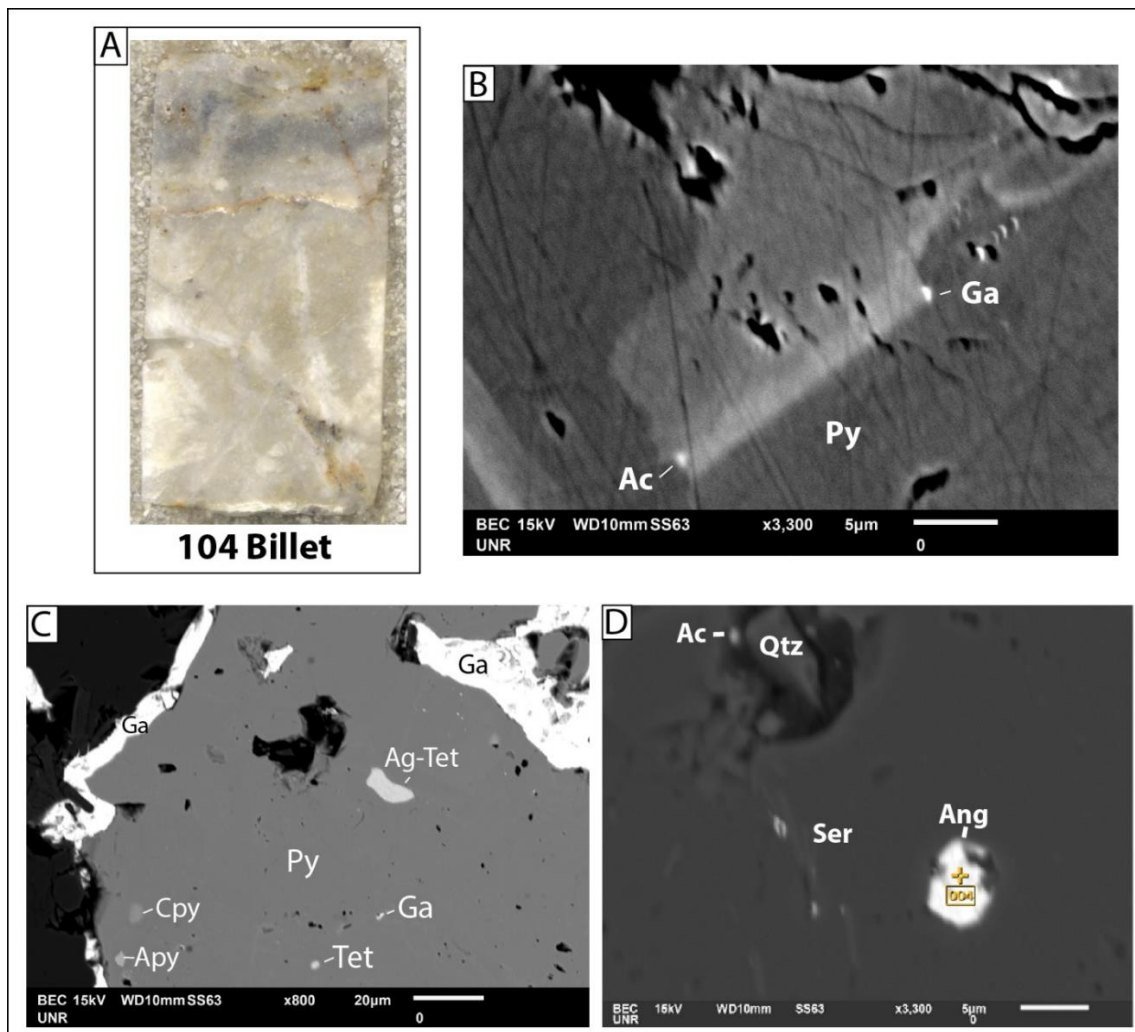


Figure 27. Sample 104 from mapped 6425 Bench #2 in the Rochester Formation mixed zone. **A.** Thin section billet assayed 2.5 opt Ag and 0.008 opt Au. **B.** SEM BSE image showing acanthite (Ac) and galena (Ga) along arsenian and lead-rich growth zones in pyrite (Py). **C.** SEM BSE image showing Ag-tetrahedrite (Ag-tet), chalcopyrite (Cpy), arsenopyrite (Apy), and galena inclusions in pyrite rimmed by late galena. **D.** SEM BSE image showing acanthite and anglesite (Ang) in a quartz (Qtz) and sericite (Ser) groundmass.

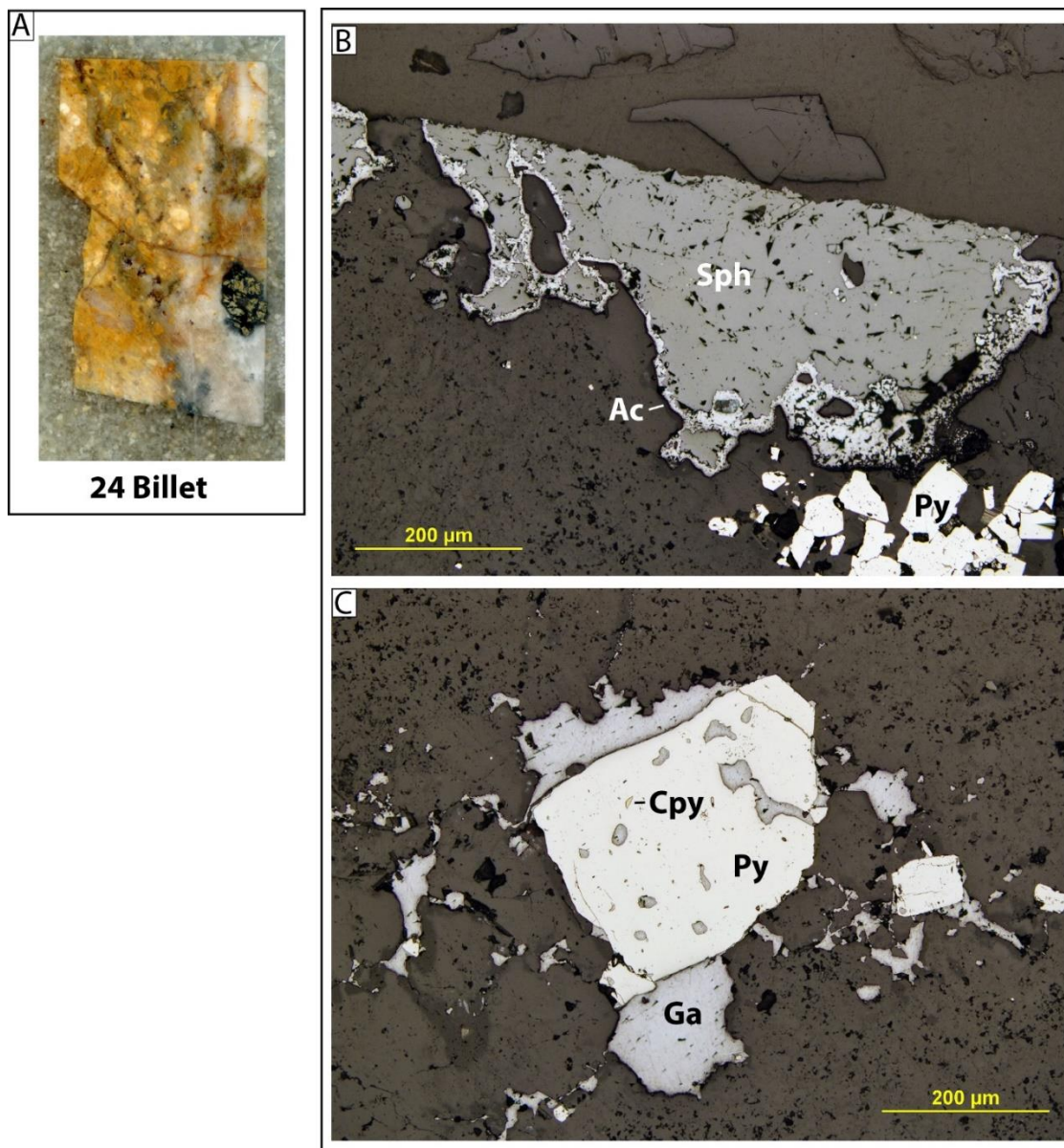


Figure 28. Core hole 9712C from the oxide-mixed zone boundary Weaver Formation. Sample interval 21.3-24.2 ft assayed 2.58 opt Ag and 0.02 opt Au. **A.** Thin section billet of sample 24 ft. **B.** Reflected light photo showing acanthite (Ac) rimming sphalerite (Sph). **C.** Reflected light photo showing chalcopyrite (Cpy) and galena (Ga) with pyrite (Py).

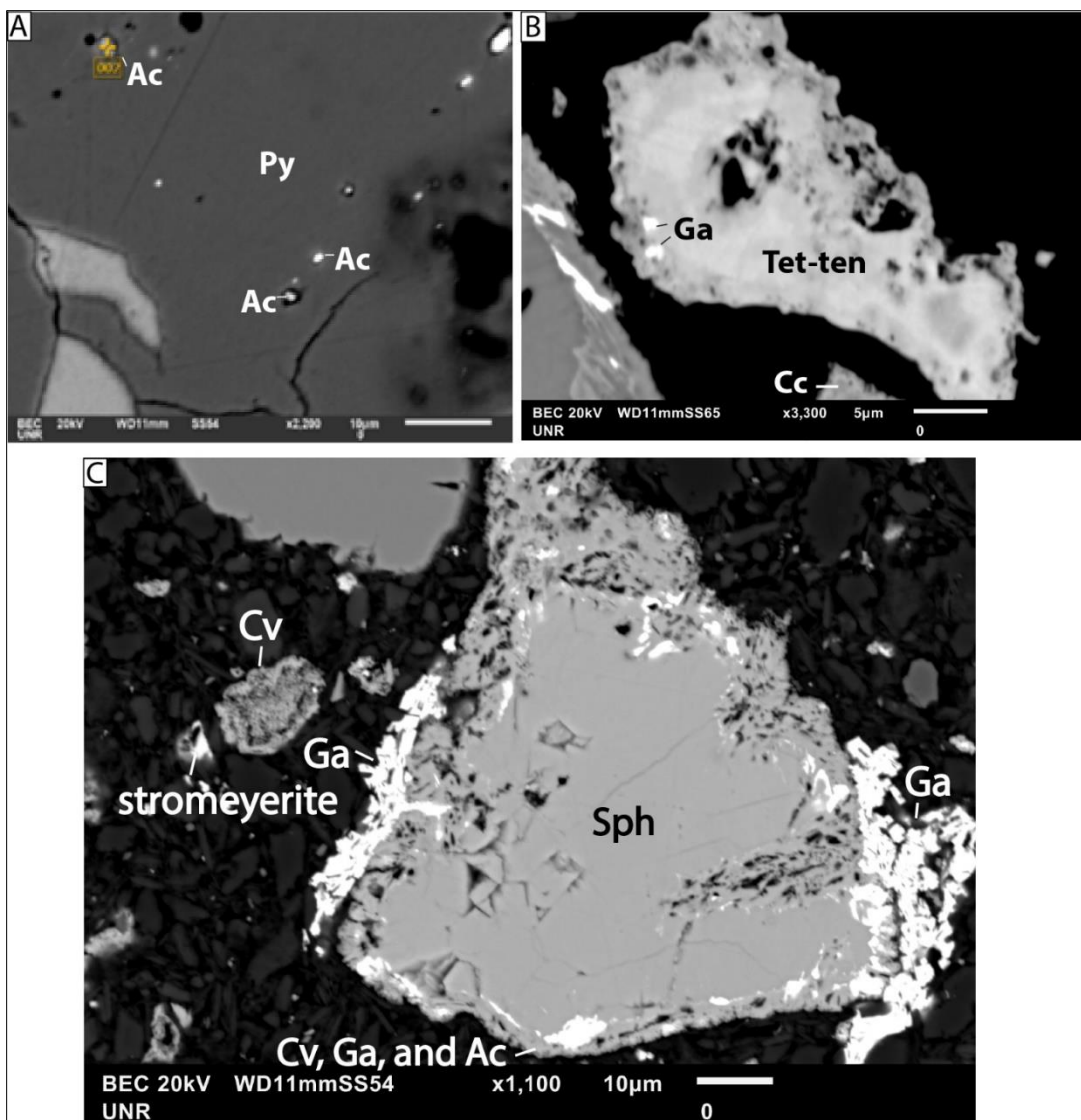


Figure 29. SEM BSE images of the sulfide portion from sample 788 ERC14-002 Rochester Formation mixed zone. **A.** SEM Acanthite (Ac) inclusions in pyrite (Py). **B.** Silver-bearing tetrahedrite (Tet) and galena inclusions. Chalcocite (Cc) is in the lower portion of the image. **C.** Covellite (Cv), galena (Ga), and acanthite (Ac) rimming a sphalerite (Sph) grain.

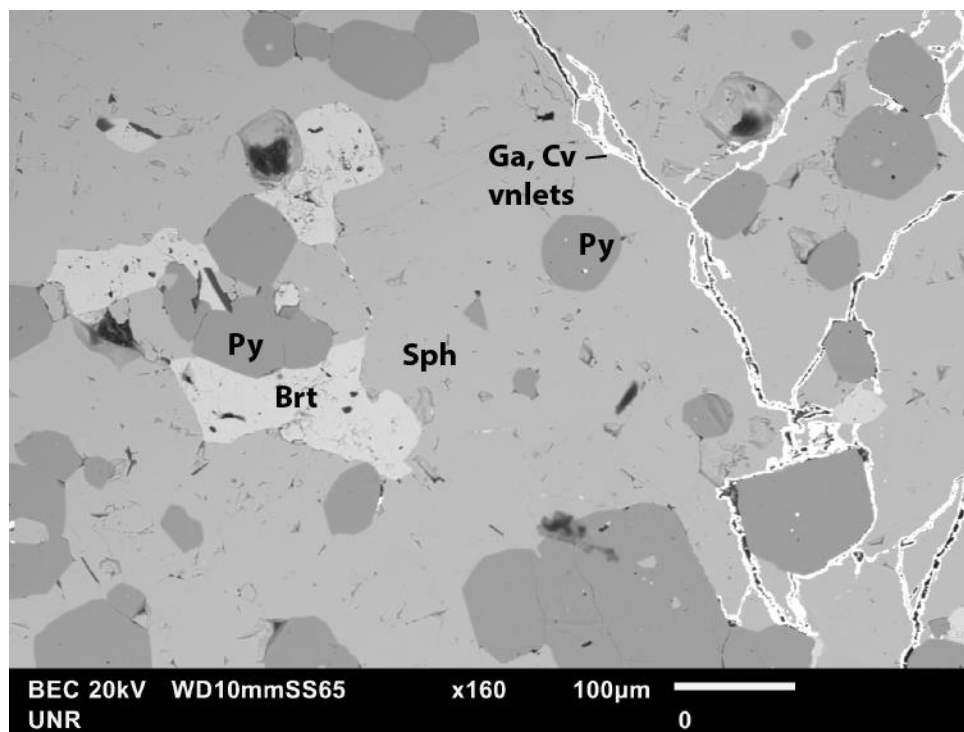


Figure 30. Sulfide portion from sample 788 ERC14-002 Rochester Formation mixed zone. Hypogene barite (Brt) and pyrite (Py) included in later sphalerite (Sph). Silver occurs within pyrite as Ag-bearing tennantite-tetrahedrite inclusions (bright spots in pyrite). Barite grows around euhedral pyrite. Veinlets composed of galena and supergene covellite cut sphalerite and occur along the grain boundaries of pyrite.

Indigenous goethite occurs as disseminations, aggregates, and veinlets with total abundance varying from ~1 to 15%. Indigenous hematite is less abundant (~0.5-5%), typically occurring as disseminations. Rare jarosite (up to 4% locally) is present in veinlets and as disseminations.

Acanthite is the dominant silver-bearing phase occurring with both hypogene and supergene textures in the mixed zone. Hypogene occurrences of acanthite occur along microfractures (Fig. 31C), and in arsenian pyrite growth zones (Fig. 31D, E; 29A; 27B, D), as well as replacing tetrahedrite-tennantite (Fig. 32 and 33). Supergene acanthite mainly occurs with covellite as rims on hypogene sulfides (Fig. 34, 23, 29C, 35, 36, 37, 38B) as well as rims on indigenous goethite (Fig. 39; 40C, E). The rims of supergene acanthite and covellite

mainly occur on sphalerite (Fig. 41, 28B, 42), galena (Fig. 34), and less commonly pyrite (Fig. 40B) and tetrahedrite-tennantite (Fig. 33, 35, 36). The supergene origin for these rims is further supported by the rarity of such rims in the sulfide zone. There are numerous minor supergene silver phases associated with acanthite including stromeyerite (Fig. 34D, 29C, 43A), chlorargyrite (Fig. 43A), imiterite (Fig. 44C), native silver (Fig. 43C, 40D, 40E), stephanite (Fig. 40D), and miargyrite (Fig. 43B). The rims of silver-bearing minerals are locally rimmed by goethite and anglesite (Fig. 40D) suggestive of incipient oxidation of supergene sulfides.

Stromeyerite occurs as both inclusions in pyrite and rimming pyrite with acanthite and covellite suggesting both hypogene and supergene origin for stromeyerite (Fig. 34D). Native silver and chlorargyrite are typically found with acanthite in areas of stronger oxidation, suggesting they could form by oxidation of relict hypogene silver-bearing sulfides, sulfosalts, and supergene sulfides, such as the rims of acanthite. Anglesite and plattnerite(?) occur in areas typically associated with the oxidation of galena (Fig. 34 and 42). Minor jarosite indicates local highly oxidized, acidic conditions that post-dated formation of the supergene sulfides. Anhedral acanthite occurring as discrete grains (Fig. 38D) and in masses of indigenous goethite (Fig. 44 and 45) is likely supergene acanthite that is oxidizing in place and forming immobile silver phases such as native silver and silver-halides. The rims of silver-bearing minerals are locally rimmed by goethite and anglesite (Fig. 40D) suggestive of incipient oxidation of supergene sulfides.

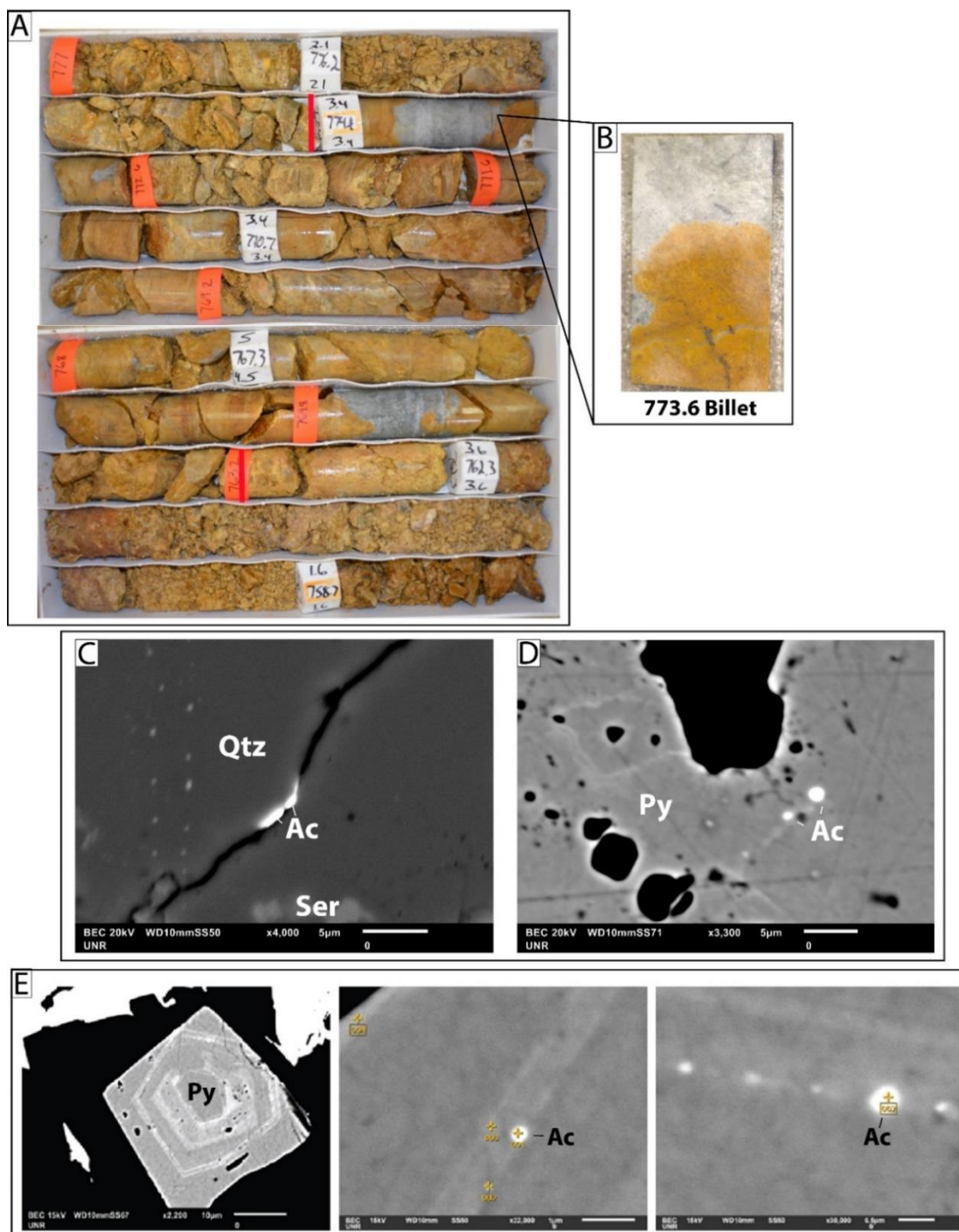


Figure 31. Core hole ERC14-002 from the Rochester Formation mixed zone. **A.** Sample interval 763.2-774.1 ft, assayed 1.33 opt Ag and 0.002 opt Au. **B.** Sample 773.6 thin section billet showing oxidation boundary containing 15% indigenous goethite, 2% indigenous hematite, and 1% remnant pyrite. **C.** SEM BSE image from the oxide portion of sample 773.6 showing acanthite (Ac) along a fracture in quartz (Qtz). **D.** SEM BSE image of acanthite in a pyrite (Py) grain making up a pyrite veinlet in the sulfide portion of sample 773.6. **E.** SEM BSE image of a pyrite grain from sample 773.6 showing acanthite along arsenian growth zones in pyrite.

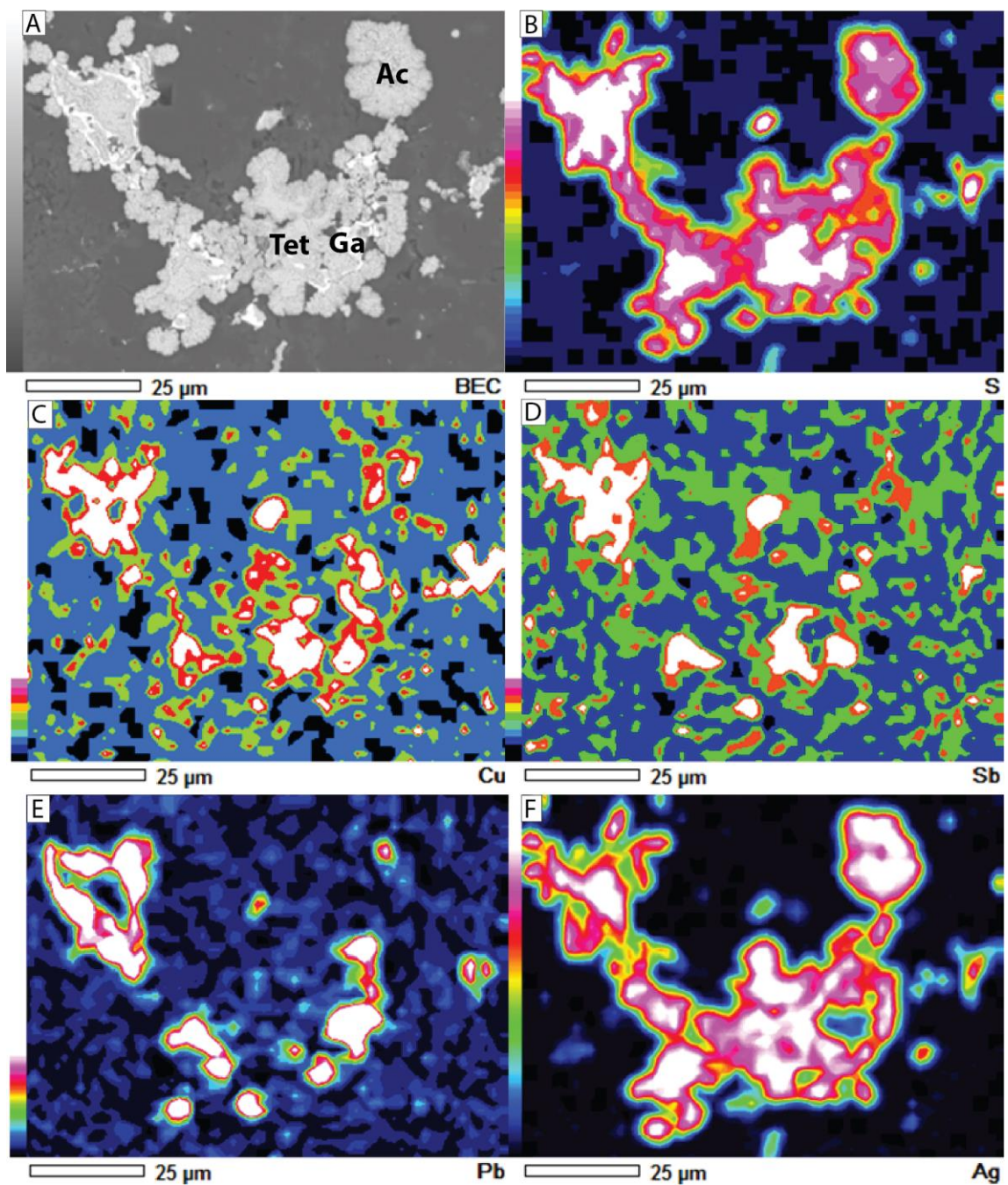


Figure 32. Sample 790.2 from ERC14-002 Rochester Formation mixed zone. **A.** SEM BSE image showing silver-bearing tetrahedrite (Tet) with later galena (Ga) and acanthite (Ac). SEM EDS elemental maps of **B.** S, **C.** Cu, **D.** Sb, **E.** Pb, and **F.** Ag.

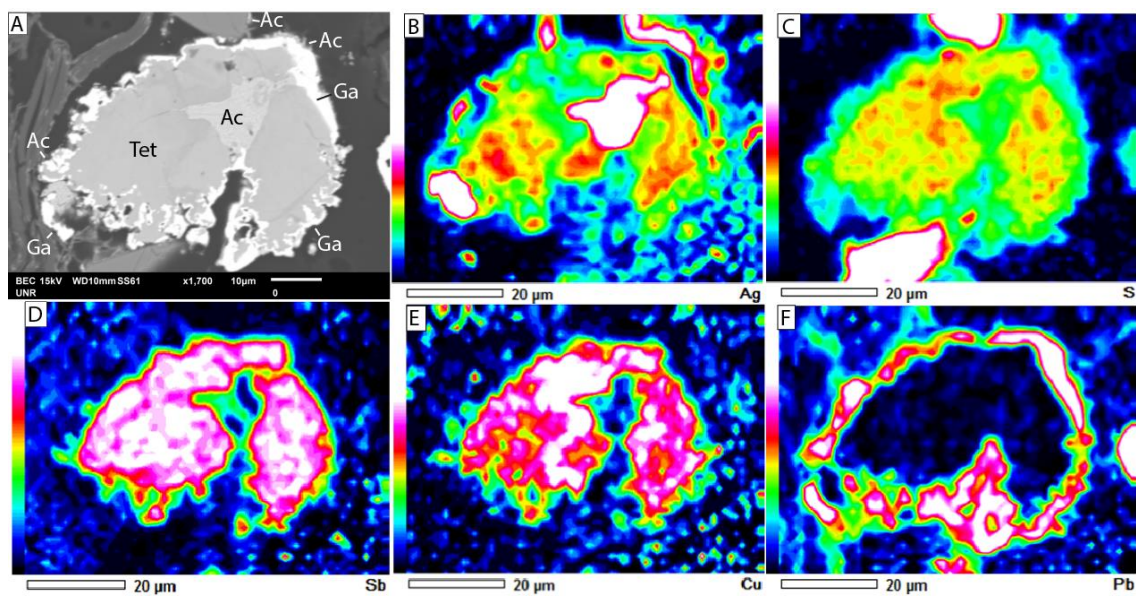


Figure 33. Sample 790.2 from ERC14-002 Rochester Formation mixed zone. **A.** SEM BSE image showing acanthite (Ac) replacing tetrahedrite (Tet) rimmed by later galena (Ga) and acanthite. SEM EDS elemental maps of **B.** Ag, **C.** S, **D.** Sb, **E.** Cu, and **F.** Pb.

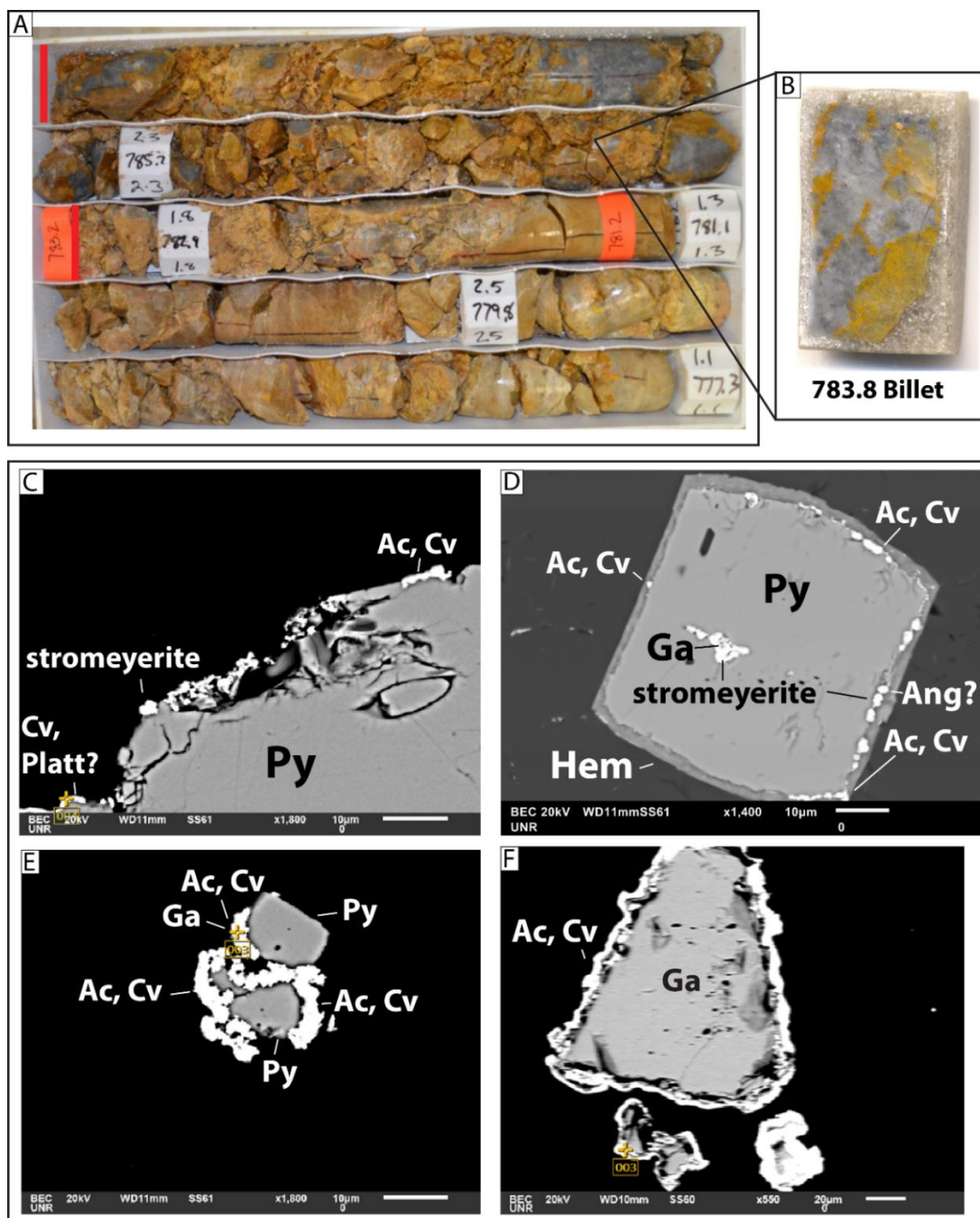


Figure 34. Core hole ERC14-002 from the Rochester Formation mixed zone. **A.** Sample interval 783.2-788 ft, assayed 5.34 opt Ag and 0.007 Au. **B.** Sample 783.8 thin section billet. **C.** SEM BSE image from 783.8 depicting stromeyerite (based on EDS analysis), acanthite (Ac), covellite (Cv), and plattnerite? (based on EDS analyses) (Platt) rimming a pyrite (Py) grain. **D.** SEM BSE image from 783.8 showing stromeyerite and galena enclosed by a pyrite grain and acanthite, stromeyerite, covellite, and anglesite(?) (Ang) rimming the pyrite grain that has a hematite oxidation rim. **E.** SEM BSE image from 783.8 showing acanthite, covellite, and galena rimming a pyrite grain. **F.** SEM BSE image from 783.8 showing acanthite and covellite rimming a galena grain.

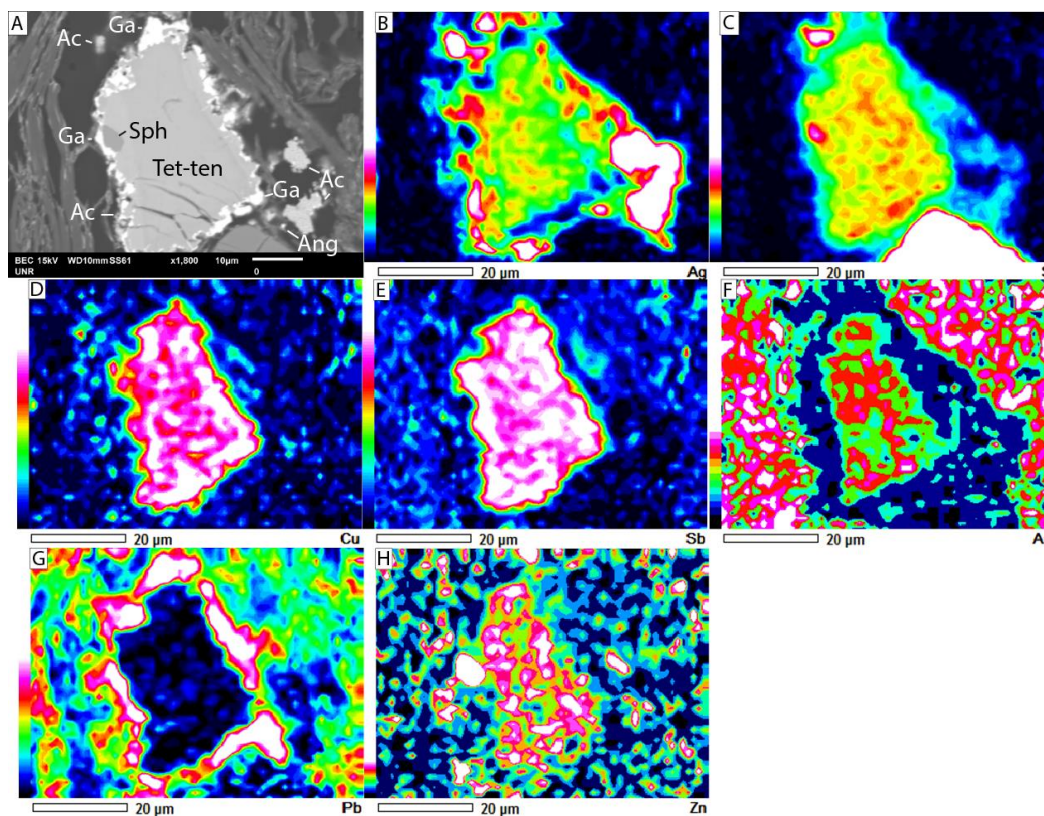


Figure 35. Sample 790.2 from ERC14-002 Rochester Formation mixed zone. **A.** SEM BSE image showing tetrahedrite-tennantite (Tet-ten) with later sphalerite (Sph) rimmed by galena (Ga) and acanthite (Ac). Some galena is oxidized to anglesite (Ang). SEM EDS elemental maps of **B.** Ag, **C.** S, **D.** Cu, **E.** Sb, **F.** As, **G.** Pb, and **H.** Zn.

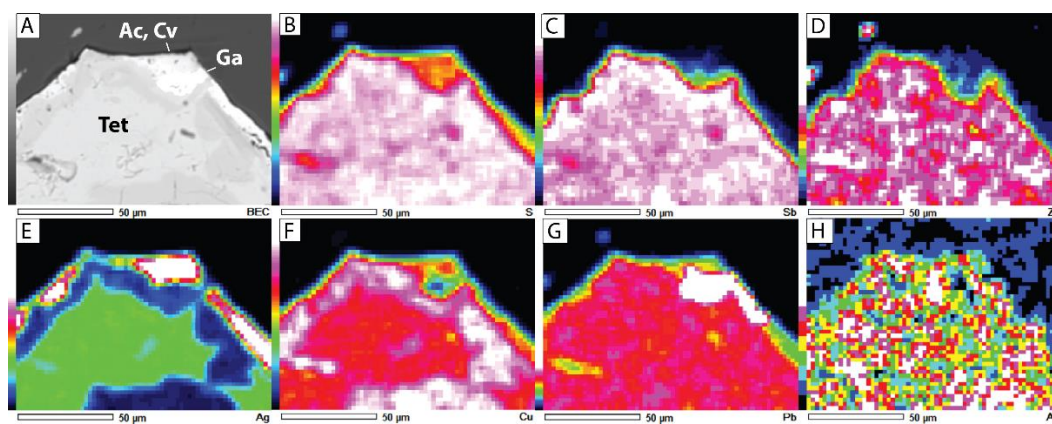


Figure 36. Oxide portion from sample 788 ERC14-002 Rochester Formation mixed zone. Acanthite (Ac) and covellite (Cv) rimming galena (Ga) and tetrahedrite (Tet). **A.** SEM BSE image, the lighter areas in the tetrahedrite (Tet) are silver-rich, whereas the darker areas are enriched in Cu and Sb. SEM EDS elemental maps of **B.** S, **C.** Sb, **D.** Zn, **E.** Ag, **F.** Cu, **G.** Pb, and **H.** As.

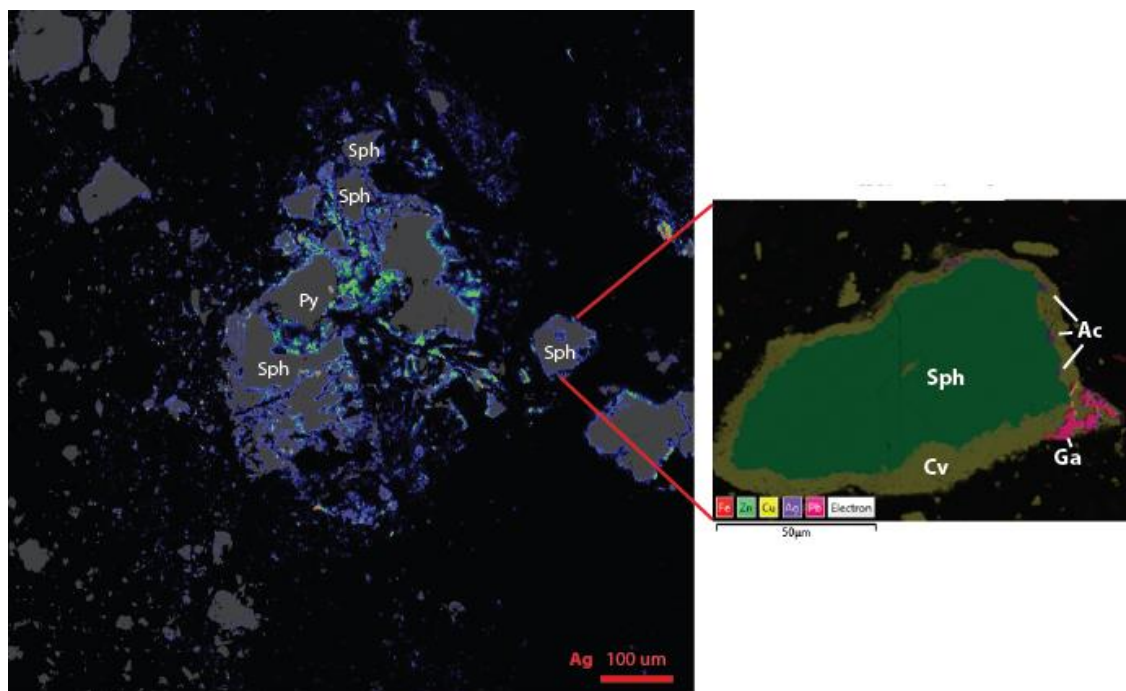


Figure 37. Sulfide portion of sample 788 ERC14-002 from the Rochester Formation mixed zone. On the left is an electron microprobe WDS silver elemental map showing predominantly acanthite rimming hypogene sulfides pyrite and sphalerite. On the right is an SEM EDS layered map showing acanthite and covellite rimming sphalerite and galena.

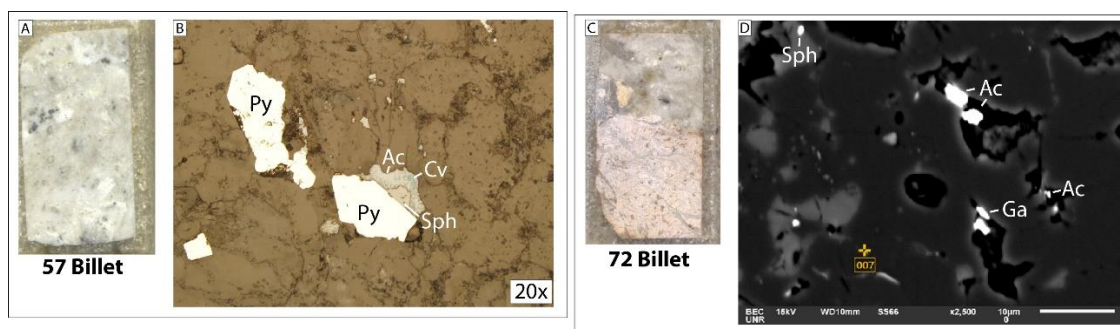


Figure 38. 6425 Bench #2 in the Rochester Formation mixed zone. **A.** Thin section billet of sample 57, assayed 0.91 opt Ag and 0.0014 opt Au. **B.** Reflected light photo from sample 57 showing supergene covellite (Cv) and acanthite (Ac) rimming a sphalerite (Sph) and pyrite (Py). **C.** Thin section billet of sample 72, assayed 2.43 opt Ag and 0.004 opt Au. **D.** SEM BSE image from sample 72 showing sphalerite, acanthite, and galena (Ga) surrounded by quartz and sericite.

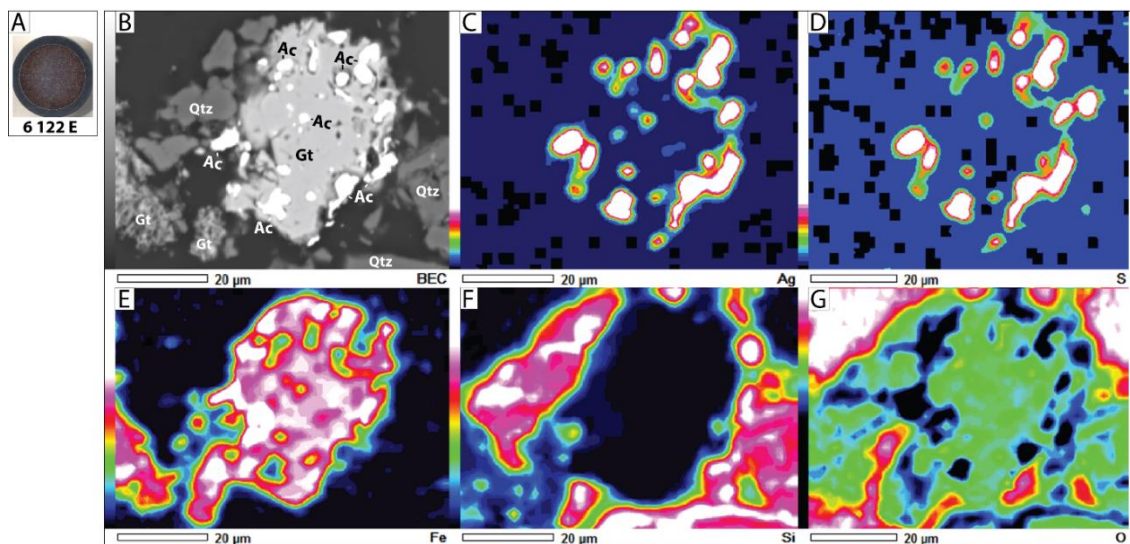


Figure 39. A. Grain mount 6 122 E from Vikre's (1977; 1981) work from the mixed zone. B. SEM BSE image showing acanthite (Ac) grains with goethite (Gt) surrounded by quartz (Qtz). SEM EDS elemental maps of C. Ag, D. S, E. Fe, F. Si, and G. O.

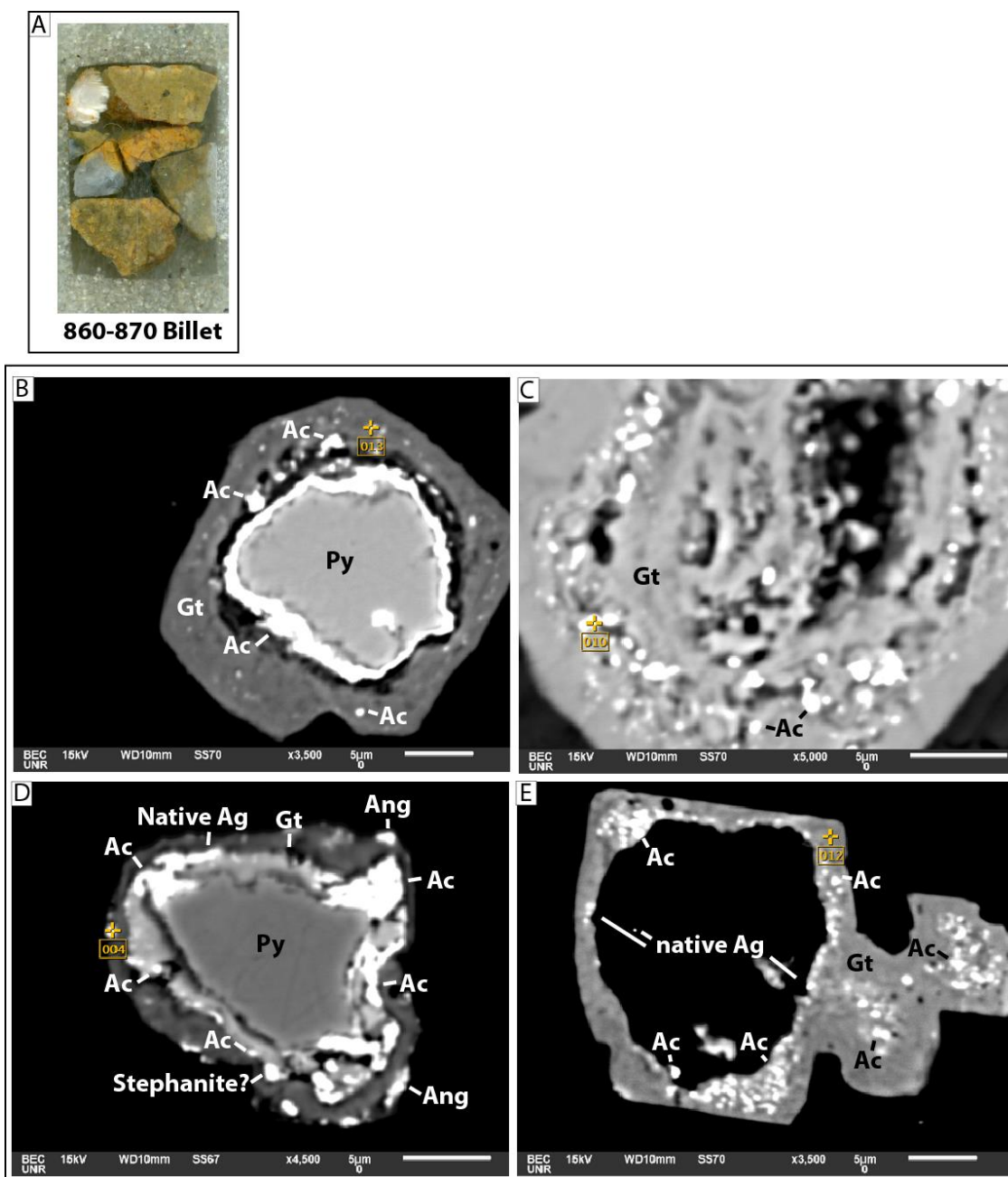


Figure 40. RC hole ER14-001 from the Rochester Formation mixed zone. **A.** Thin section billet from 860-870 ft interval that assayed 12.76 opt Ag and 0.016 opt Au. **B.** SEM BSE image showing pyrite (Py) partially oxidized to goethite (Gt) with blebs of acanthite (Ac). **C.** SEM BSE image showing discrete acanthite grains occurring with goethite. **D.** SEM BSE image showing a pyrite grain partially oxidized to goethite that contains grains of acanthite, native Ag, stephanite(?), and anglesite (Ang). **E.** SEM BSE image showing former pyrite that is now a leached cavity coated with goethite, acanthite, and native silver.

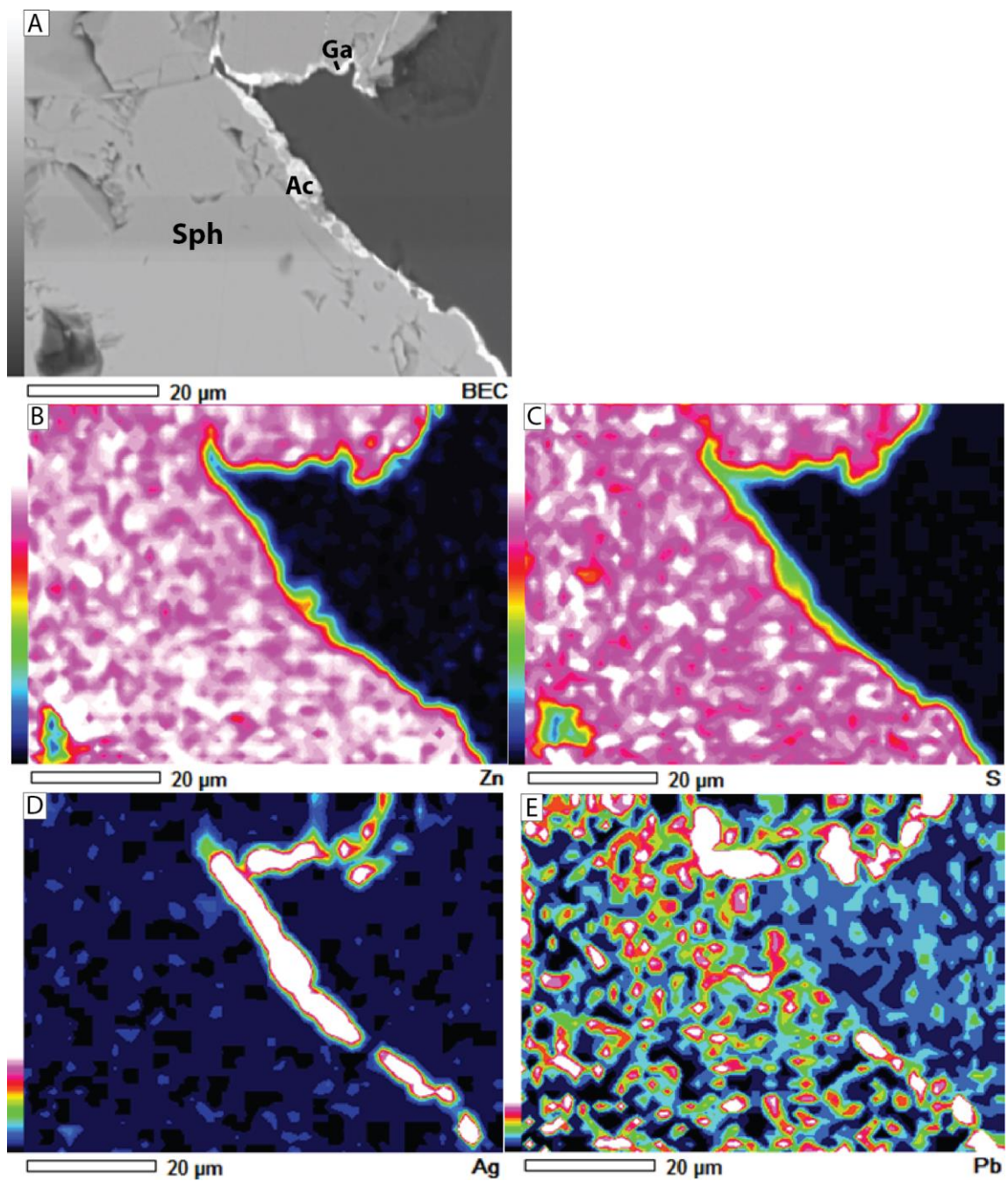


Figure 41. Sample 790.2 from ERC14-002 Rochester Formation mixed zone showing **A.** SEM BSE image of acanthite (Ac) and galena (Ga) rimming sphalerite (Sph). SEM EDS elemental maps of **B.** Zn, **C.** S, **D.** Ag, and **E.** Pb.

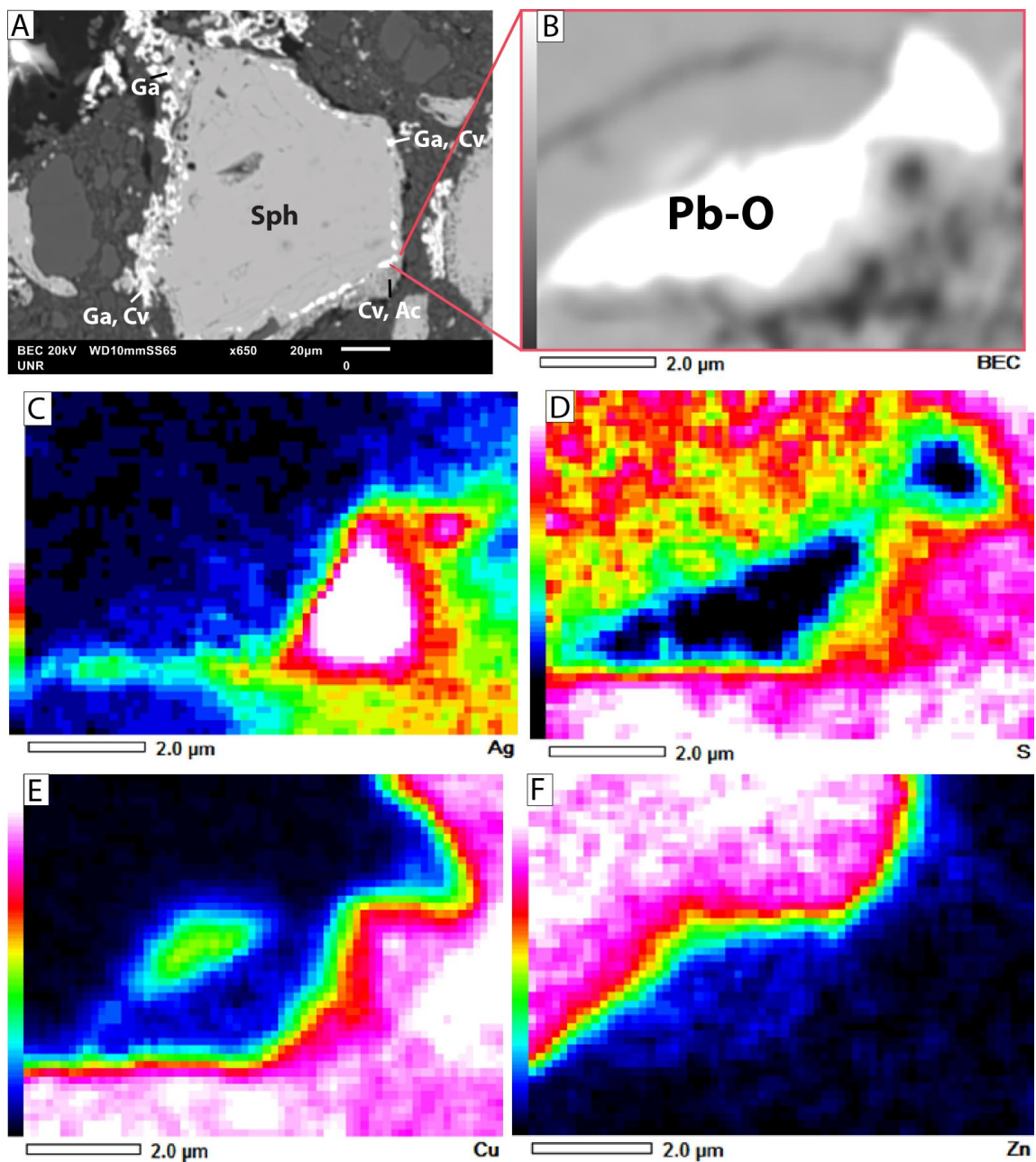


Figure 42. Sulfide portion of sample 788 from ERC14-002 Rochester Formation mixed zone. **A.** SEM BSE image showing sphalerite (Sph) rimmed by covellite (Cv), acanthite (Ac), and galena (Ga). **B.** Enlarged SEM BSE image of acanthite and an unknown lead-oxide phase (plattnerite?) rimming sphalerite. SEM EDS elemental maps of **C.** Ag, **D.** S, **E.** Cu, and **F.** Zn.

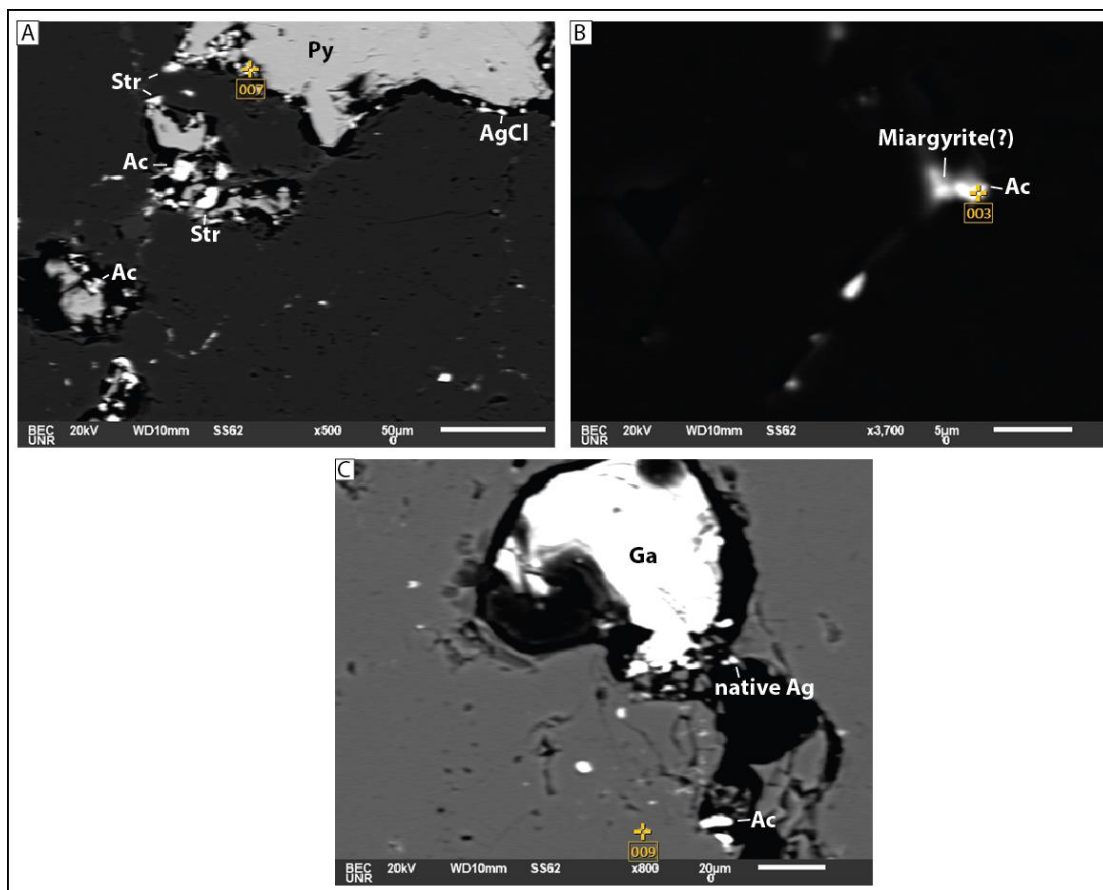


Figure 43. Sample 104 from 6425 bench #2 in the Rochester Formation mixed zone. **A.** SEM BSE image from sample 104 showing late stromeyerite (Str), acanthite (Ac), and chlorargyrite (AgCl) rimming pyrite (Py). **B.** SEM BSE image showing miargyrite(?) and acanthite surrounded by quartz and sericite. **C.** SEM BSE image showing native Ag and acanthite surrounded by quartz and sericite.

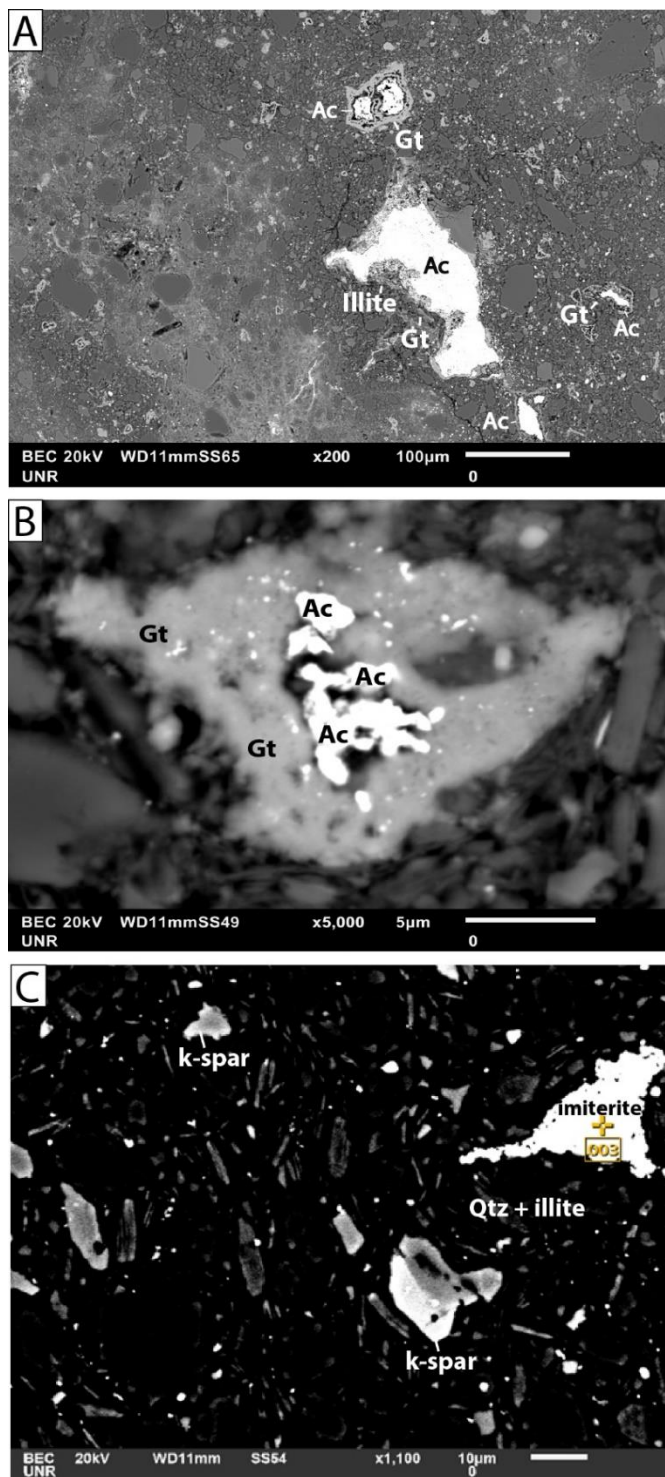


Figure 44. Oxide portion from sample 788 ERC14-002 Rochester Formation mixed zone. **A.** SEM BSE image showing acanthite (Ac) surrounded by goethite (Gt) and illite. **B.** SEM BSE image showing acanthite is enveloped by goethite (Gt). **C.** SEM BSE image showing imiterite surrounded by gangue including quartz, illite, and relict K-feldspar. Mercury assayed over 100 ppm in this sample.

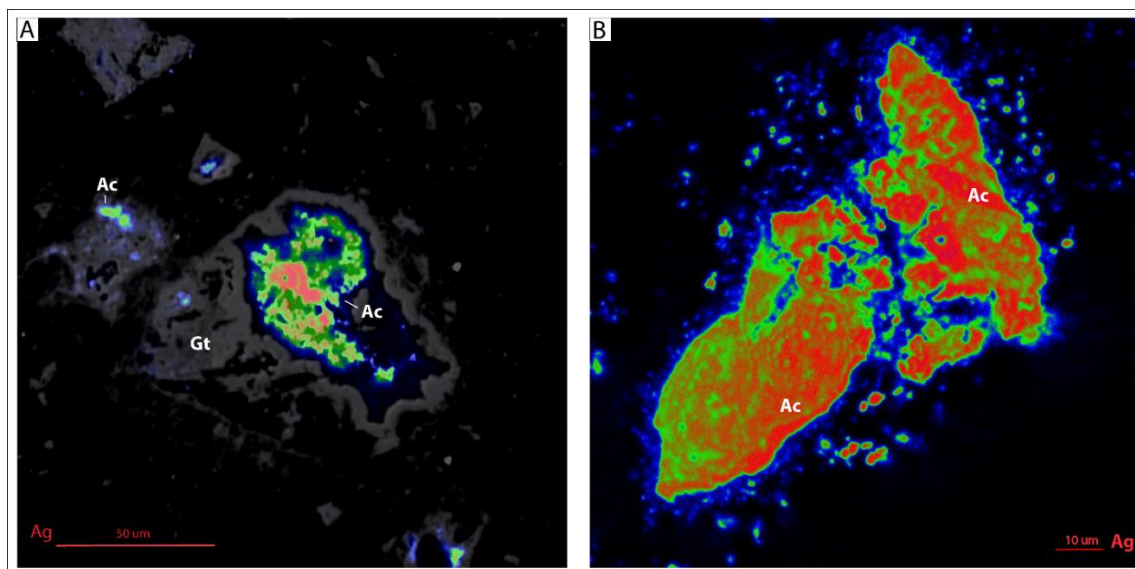


Figure 45. Sample 788 from ERC14-002 Rochester Formation mixed zone. Electron microprobe WDS elemental maps of silver. **A.** Oxide portion of sample 788 showing acanthite (Ac) surrounded by goethite (Gt). **B.** Sulfide portion of sample 788 showing acanthite as aggregates.

Paragenesis

Through detailed petrography, 16 hypogene phases and 22 supergene phases have been identified (Fig. 46). Pyrite is the dominant and first sulfide phase to form. This first generation of pyrite appears to be stoichiometrically pure and is free of inclusions. A second generation of pyrite has zones of arsenian pyrite and contains acanthite, and occasionally galena along growth zones of pyrite indicating these minerals formed during the second generation of pyrite. Other sulfides that occur as inclusions in, and, therefore likely before, this second generation of pyrite include tetrahedrite-tennantite, which is locally argentiferous, chalcopyrite, molybdenite, arsenopyrite, and rare stromeyerite suggesting these phases were formed before the second generation of pyrite. Tetrahedrite-tennantite post-dates chalcopyrite but formed prior to sphalerite and galena. Sphalerite is the second most abundant sulfide phase and is always later than arsenian pyrite and barite. Galena is the latest hypogene phase. Pearceite formed after

MINERAL PHASE	HYPOGENE Sulfide Zone	SUPERGENE Mixed Zone	SUPERGENE Oxide Zone
Quartz	—————		
K-feldspar	—		
Sericite	—————		
Pyrite	—————		
Chalcopyrite	—————		
Molybdenite	—————		
Tetrahedrite-tennantite	—————		
Stromeyerite	—	—————	
Acanthite	—————	—————	
Galena	—————		
Arsenopyrite	—————		
Arsenian Pyrite	—————		
Barite	—————		
Sphalerite	—————?	
Pearceite	?.....	?.....?	
Polybasite	?.....?		
Goethite		—————	—————
Jarosite		—————	
Hematite		—————	
Illite			—————
Covellite		—————	
Chalcocite		—————	
Proustite		—————	
Stephanite		—————	
Miargyrite		—————	
Chlorargyrite		—————	—————
Iodargyrite			—————
Illite			—————
Native Ag			—————
Native Au?			—————
Ag-Sb			—————
Imiterite		?
Anglesite		—————?
Valentinite			—————
Malachite			—————
Plattemite			?.....?

Figure 46. Interpreted hypogene and supergene mineral phase paragenesis at the Rochester mine.

chalcopyrite but it is not clear if pearceite is a supergene or hypogene phase. Barite formed after the second generation of pyrite.

Supergene covellite and acanthite are found together rimming hypogene sulfides, mostly sphalerite, but also galena partially oxidized to anglesite. Locally these rims occur on pyrite,

tetrahedrite-tennantite, and chalcopyrite. Goethite and acanthite appear to have formed by initial weathering of pyrite. The presence of hematite, especially in high silver grade samples, may be indicative of oxidation of supergene acanthite and other supergene silver-bearing sulfide phases with higher metal to sulfur ratios. Native silver and silver-halides likely formed by the oxidation of supergene silver phases. Imiterite forms at numerous stages of weathering likely due to the mobility of mercury.

Controls on Silver Mineralization

Porphyry copper deposits commonly develop supergene chalcocite enrichment blankets during weathering. Cross sections were constructed to identify any blanket-like morphology related to silver grade at Rochester, similar to those found in porphyry copper deposits. The Weaver and Rochester Formations are the only lithologic units at the Rochester mine and both host silver mineralization (Fig. 47B). High-angle faults cut and offset stacked low-angle faults (Fig. 47A). The boundaries between the oxide-mixed and mixed-sulfide weathering zones generally follow the morphology of the Weaver-Rochester contact with an overall dip to the east (Fig. 47D). Humps in the boundary between the oxide and mixed zones are largely controlled by faults but likely also reflect differences in logging among the dozens of geologists that have worked at the mine over the last 40 years. Patterns of silver grade observed in multiple cross-sections do not indicate the presence of any blanket-like geometries that suggest similarities to supergene enrichment blankets observed in porphyry copper deposits. High silver grades (≥ 2 opt Ag) are largely controlled by the Weaver-Rochester contact, high- and low-angle faults, and the oxide-mixed weathering boundary (Fig. 48). Most of the high grade occurs in the Weaver Formation oxide zone.

Comparison of geological characteristics to silver grades in logged core holes shows intensity of oxidation, dark sulfides, and fault gouge are the best macroscopic indicators of silver

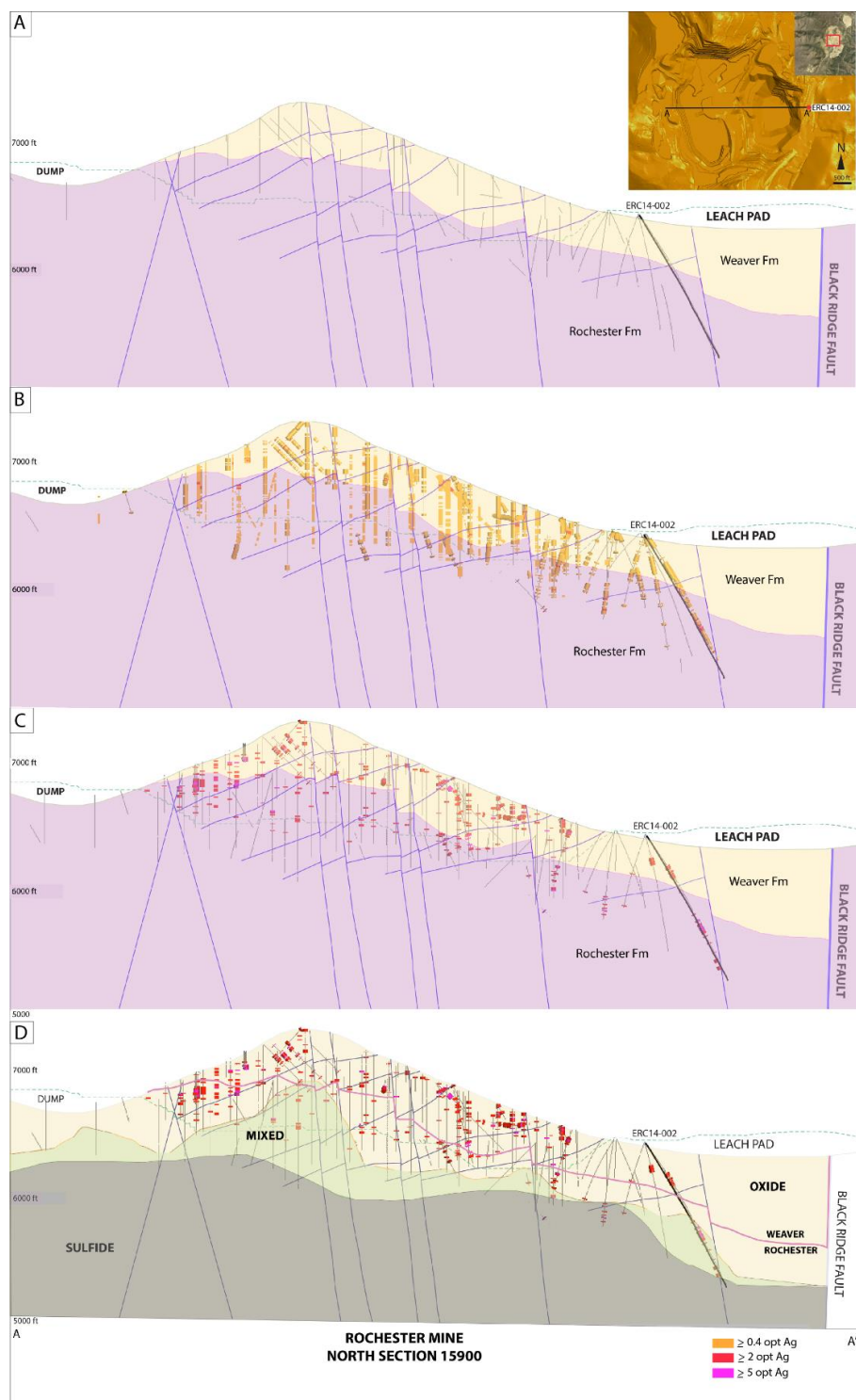


Figure 47. Schematic cross section A-A' at 15900 N through the Rochester pit showing the intersection of high- and low-angle faults and the Weaver-Rochester contact. **A.** No silver grades shown. **B.** Cut off silver grades of ≥ 0.4 opt in orange. **C.** High silver grades of ≥ 2 opt in red and ≥ 5 opt in pink. **D.** The oxide, mixed, and sulfide weathering zones shown with ≥ 2 opt Ag in red and ≥ 5 opt Ag in pink.

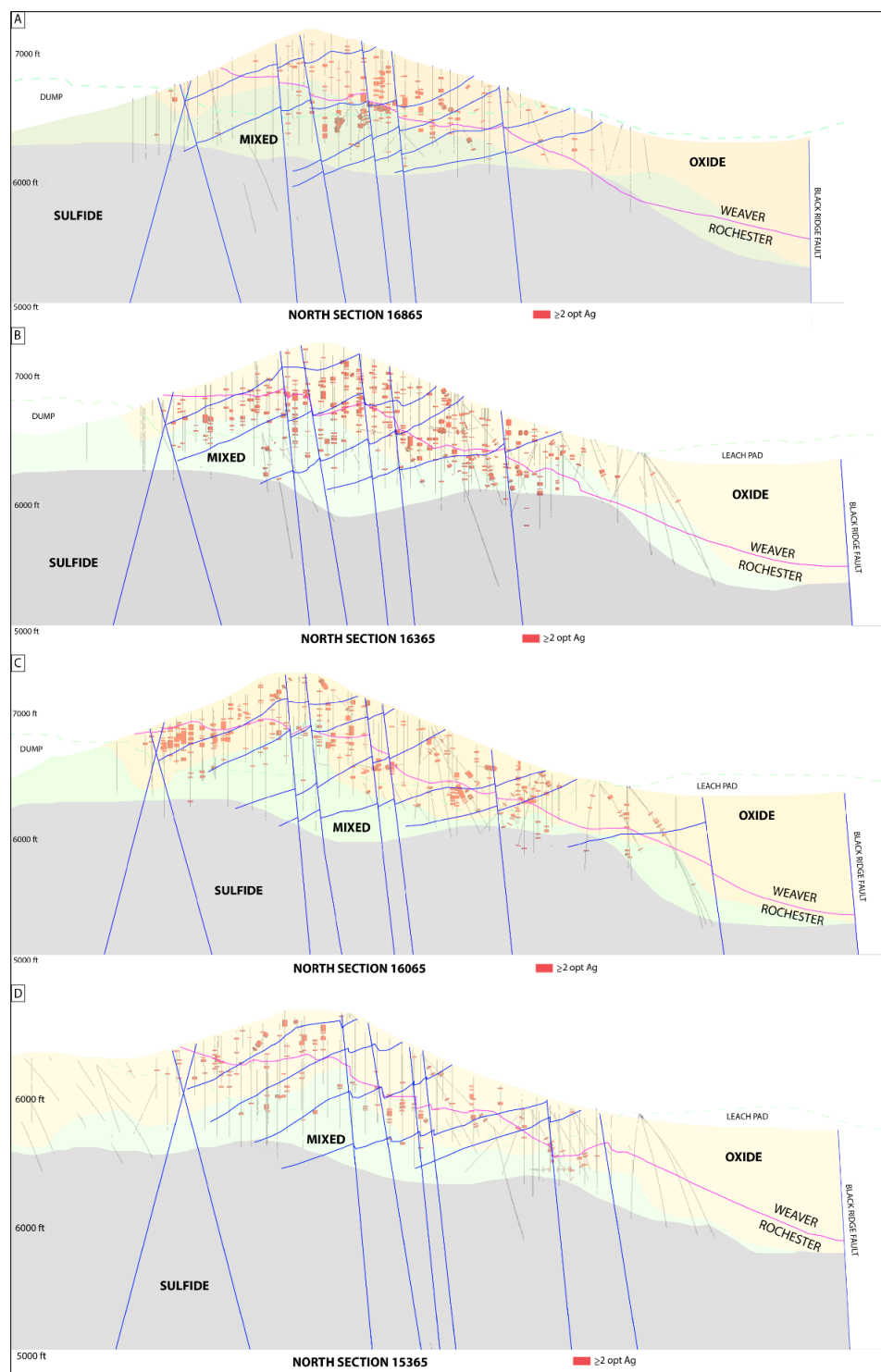


Figure 48. A. Cross section 16865 N showing ≥ 2 opt Ag largely in Weaver oxide and Rochester mixed. B. Cross section 16365 N showing ≥ 2 opt Ag along the Weaver-Rochester contact. C. Cross section 16065 N showing ≥ 2 opt Ag along the Weaver-Rochester contact clustering around fault zones. D. Cross section 15365 N showing ≥ 2 opt Ag along faults near the Weaver-Rochester contact.

grade (Fig. 49, 50, 51). The highest silver grades from pit mapping are associated with the intersection of low- and moderate- to high-angle faults, disseminated dark sulfides, and an increase in indigenous and exotic limonite (Fig. 52 and 53). Examination of the Weaver-Rochester contact in drill core indicates faults, especially fault intersections, within a few hundred feet of the contact are the primary control rather than the contact itself.

High silver grades overwhelmingly occur in the oxide weathering zone and along the oxide-mixed boundary. There are only a few high-grade silver intercepts in the sulfide zone (Fig. 47D). Acanthite is the dark sulfide that is largely associated with these high silver grades in the oxide and mixed zones. In the oxide zone acanthite occurs as discrete grains with various other silver phases, predominantly chlorargyrite and native silver (Fig. 21). In the mixed zone acanthite occurs both as discrete grains with various other silver phases (Fig. 40) and as rims on primary sulfides (Fig. 37). The occurrences and textures of acanthite suggest a predominantly supergene origin.

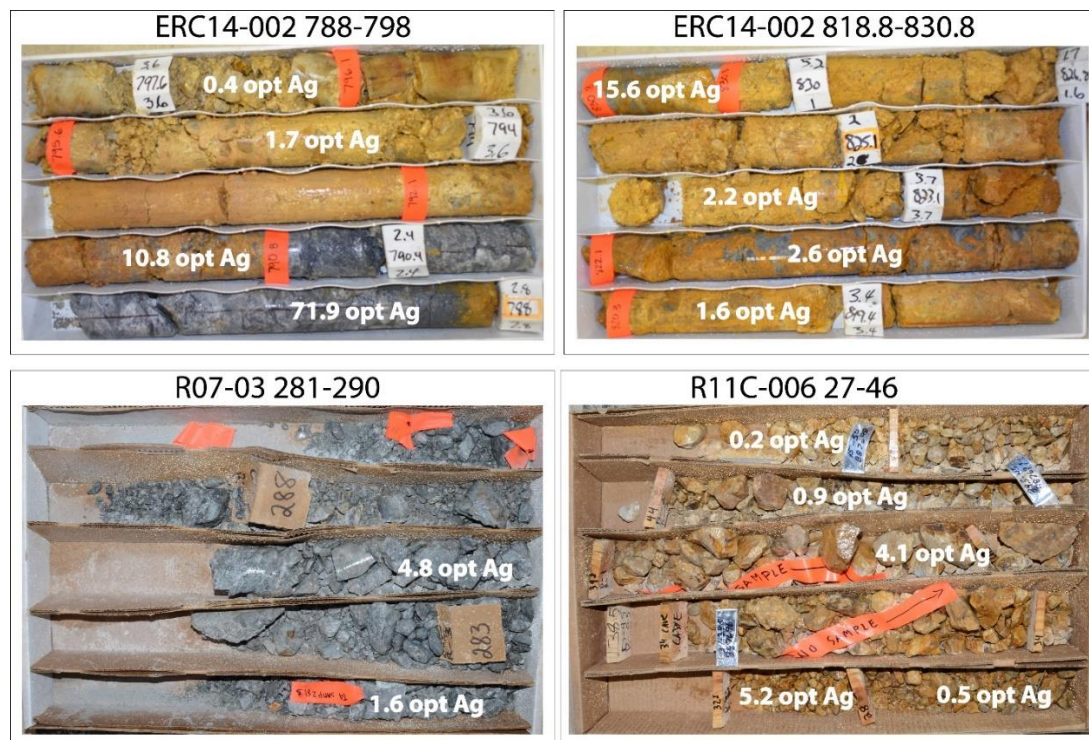


Figure 49. Sampled drill core intervals with the highest silver grades.

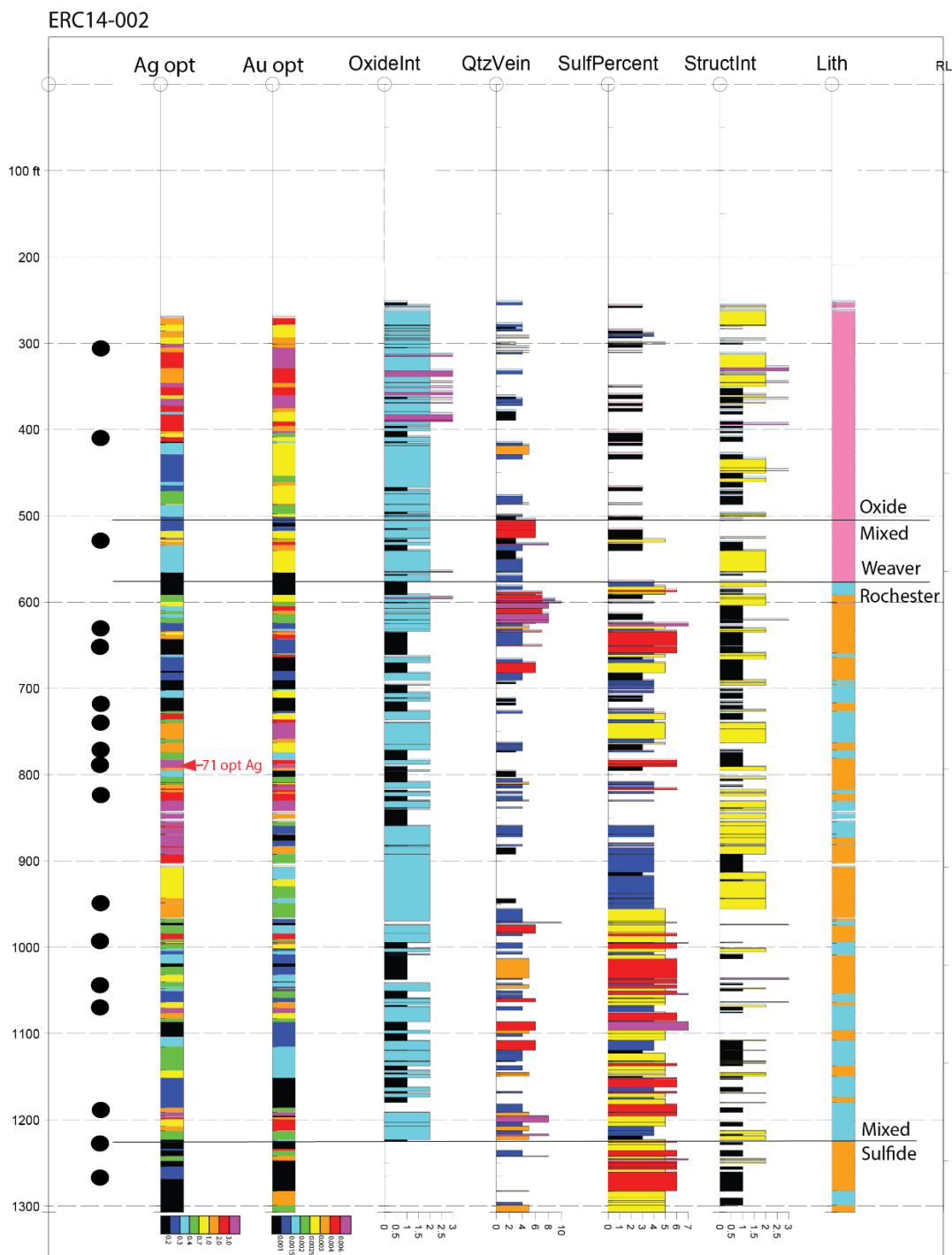


Figure 50. Silver, gold, and geological characteristics of core hole ERC14-002 are shown. The top of the hole was drilled through dump material and not recovered. Oxide intensity is the volume percent of total limonite, quartz veining is the estimated volume percent of quartz veins, sulfide percent is the estimated volume percent of total sulfides, and structure intensity is relative amount of deformation as determined by fracture density and gouge development. Lithology includes both the Weaver Formation in pink and Rochester Formation in blue (massive tuff) and orange (flow layered tuff). Black dots on the left side are disseminated dark sulfide occurrences.



Figure 51. ERC14-002 high-grade assay interval in the Weaver Formation oxide zone outlined in black. Sample interval 364.5 to 364.9 ft assayed 7.08 opt Ag and 0.256 opt Au and is composed of fault gouge and strong exotic goethite.

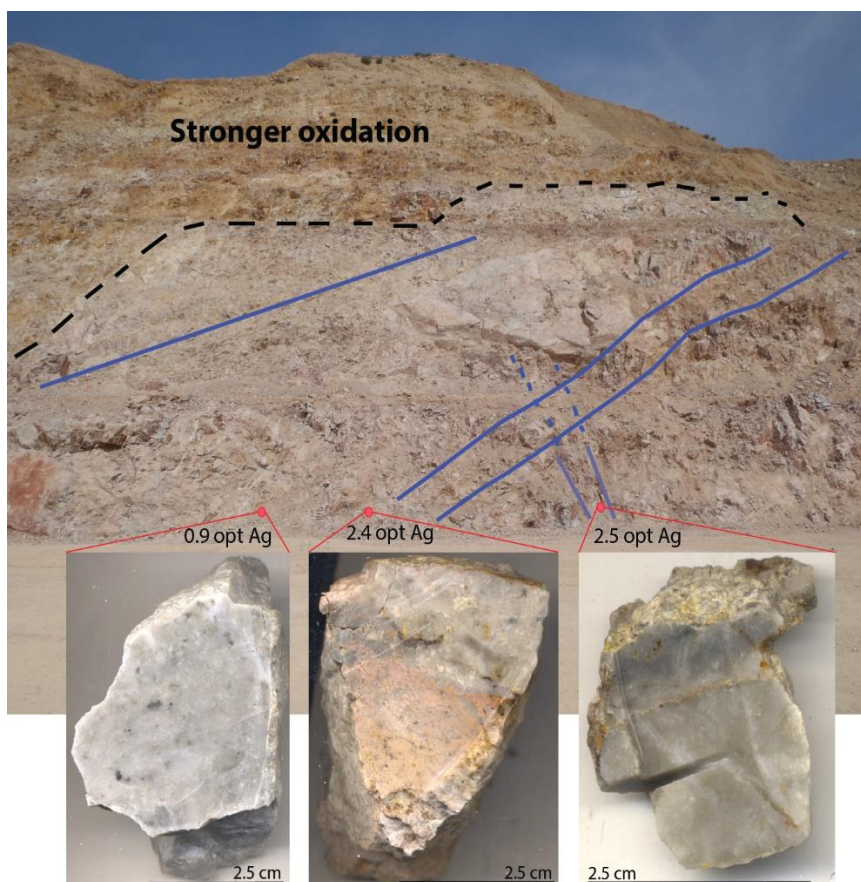


Figure 52. Pit wall from 6425 #2 bench showing the highest grade samples with the corresponding billet. The highest grade (2.5 opt Ag) was close to a fault intersection.

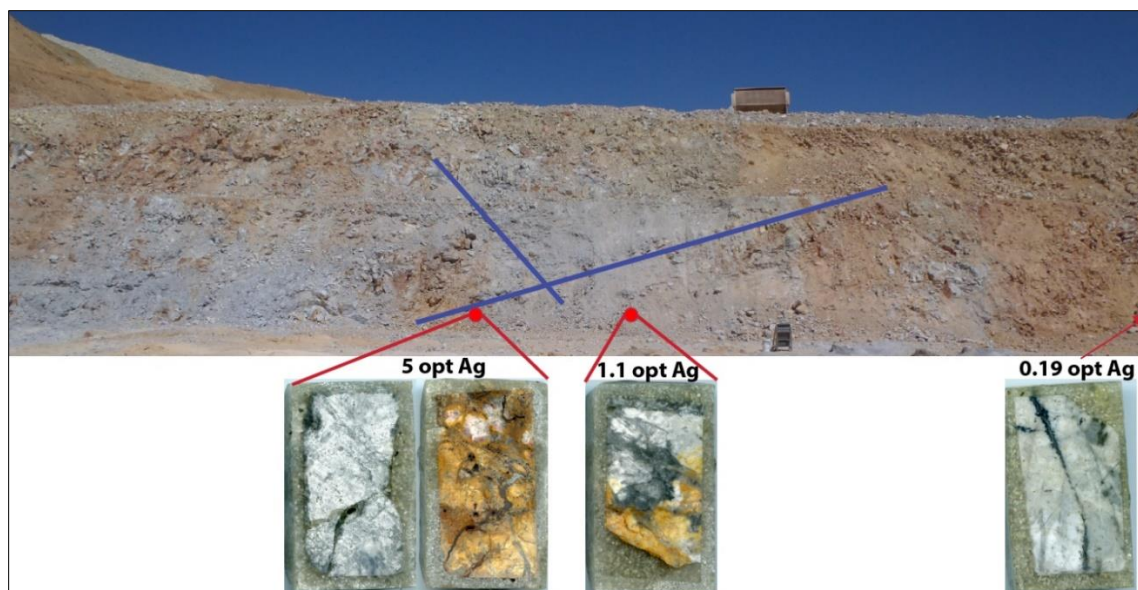


Figure 53. Bench 6425 #1 from low- to high-grade silver from right to left. The low-grade sample (0.19 opt Ag) collection site is not in the photo but is about 30 feet to the right, the sample that assayed 0.19 opt Ag is completely unoxidized with ~7% very fine grained pyrite as disseminations, clusters, and in quartz veinlets; 2% galena disseminated and on fractures, and <1% chalcopyrite. The sample that assayed 1.1 opt Ag is 40% oxidized with ~10% quartz+pyrite veinlets, ~5% disseminated pyrite; <1% chalcopyrite, acanthite, covellite, and sphalerite. The high-grade sample on the far left assayed 5 opt Ag. The oxide portion of this sample is predominantly exotic goethite>>hematite and quartz veinlets with minor indigenous goethite. The sulfide portion of this sample contains ~15% disseminated pyrite with ~0.5% acanthite.

V. Evidence for Supergene Enrichment

Although there does not appear to be a copper porphyry-like enrichment blanket, macroscopic controls on high silver grades and petrographic observations of minerals suggest zones of supergene silver enrichment are present. Most high silver grades are in the oxide zone mainly along fault zones at the base of the Weaver Formation and in the upper Rochester Formation.

Whether this increase in silver grade is related to hypogene or supergene processes is discussed here. If hypogene processes were responsible for this increasing silver grade, one might expect vertical zonation in mineralogy including, 1) change in style of veins, 2) change in sulfide assemblages, 3) change in alteration style, and 4) increasing abundance of hypogene silver relative to elevation. No major changes in style of veining, sulfide assemblages, or alteration

style were observed between low grades in Rochester sulfide and high grades in Weaver oxide. Silver grade relative to elevation is discussed below.

Comparing silver grade relative to elevation three peaks of increased silver emerge occurring mostly in the oxide and mixed zones (Fig. 54). This suggests multicyclic supergene enrichment and subsequent oxidation of enriched zones with supergene silver moving down in elevation. Less silver would move down with each new cycle of oxidation causing silver to eventually become locked up in oxidation and immobile phases. High silver grades in the sulfide

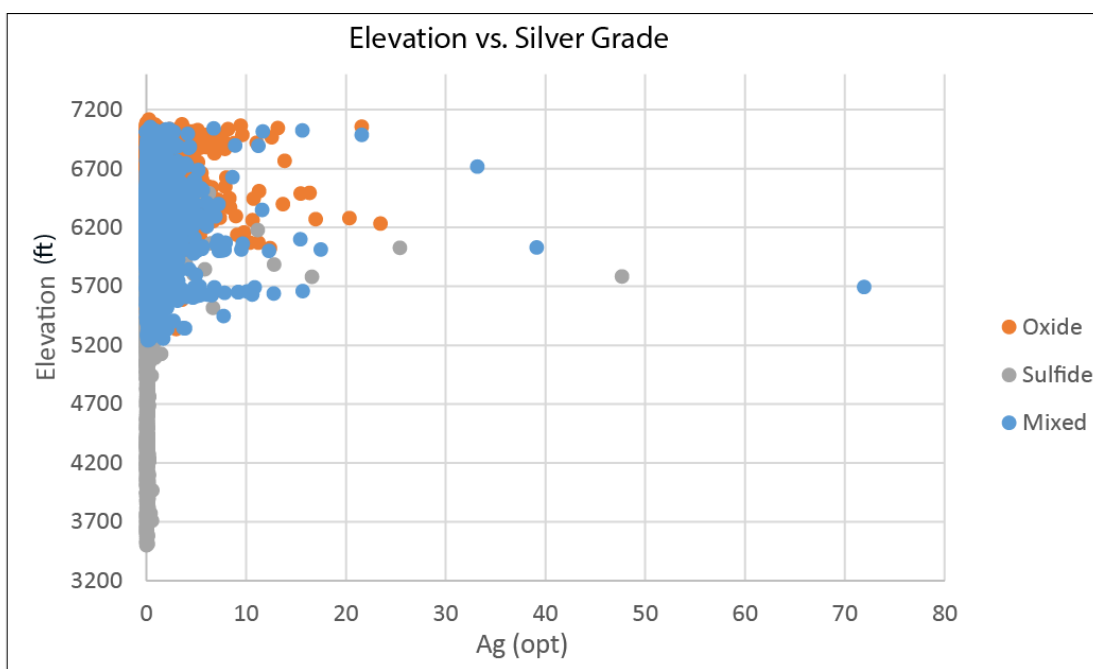


Figure 54. Elevation vs. silver grade showing grade distribution relative to oxide, mixed, and sulfide weathering zones.

zone (Fig. 54) could either be incipient supergene enrichment or the result of differences in logging the weathering zones among workers and are actually in the mixed zone. Similarly, the Ag:Au ratio would be expected to continually increase uninterrupted from the sulfide zone into the mixed and oxide zones if hypogene zonation is responsible for metal distribution (Sillitoe, 2009). At the Rochester deposit background Ag:Au ratios do increase with elevation but high

silver grades (≥ 5 opt Ag) display the same three peaks described above (Fig. 55C) indicating silver is moving independently of gold. Gold grade does show one peak which may be indicative of primary hypogene zonation (Fig. 55B).

Sillitoe (2009) attributed increases in silver grade in the oxide zone to mass loss by supergene oxidation, resulting in residual enrichment of silver. To test this, immobility plots were constructed to determine mass gains and losses of silver relative to other elements during supergene processes at Rochester. Generally, mass gain can be attributed to a variety of processes including filling of vesicles to form amygdules, veining/silicification, and/or supergene enrichment of mobile elements. Mass loss during supergene alteration is typically associated with a decrease in density due to oxidation and removal of sulfide mineral components, and the weathering of silicates to clays, resulting in residual enrichment of immobile elements. However, at Rochester there is very little supergene clay indicating sericite was largely stable during supergene oxidation, thus the only significant decrease in density would be due to oxidation of sulfides to limonite.

Immobility plots were constructed using only Rochester Formation samples from core hole ERC14-002 since pre-weathering sulfide samples of Weaver Formation rocks were not available. All samples (123 total) from the oxide and mixed zones of the Rochester Formation in core hole ERC14-002 were used to construct an immobility Al_2O_3 % vs. Zr (ppm) plot. Compositions of pre-weathering Rochester Formation rocks are based on the average of nine samples from depths of 1224.7 to 1307 (total depth) that assayed < 0.25 opt Ag. The majority of high silver grades (including the 71 opt Ag interval) are associated with mass gain in ERC14-002 (Fig. 56). The mass gain could either be related to silicification/veining or supergene enrichment. Mine wide alteration is associated with silicification and quartz veining, however high silver grades are more closely related to fault gouge, dark sulfides, and strong limonite suggesting

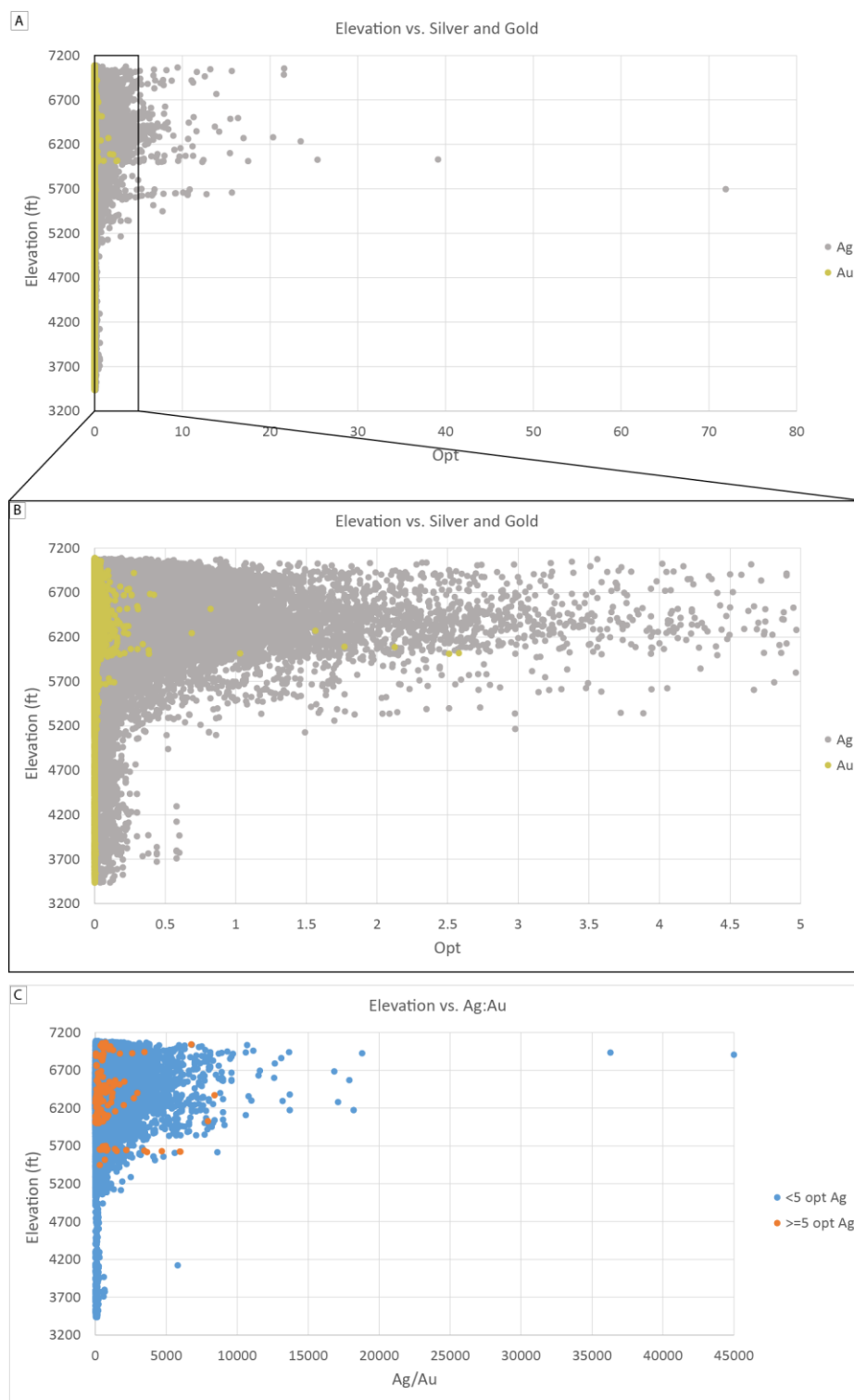


Figure 55. **A.** Elevation vs. silver and gold showing the silver to gold ratio does not continually increase with increasing elevation. **B.** Elevation vs. silver and gold with a narrower x-axis to zoom in on gold. The gold grade peak does match one of the peaks in silver grade. **C.** Elevation vs. Ag/Au showing high silver grades do not correspond to high gold grades.

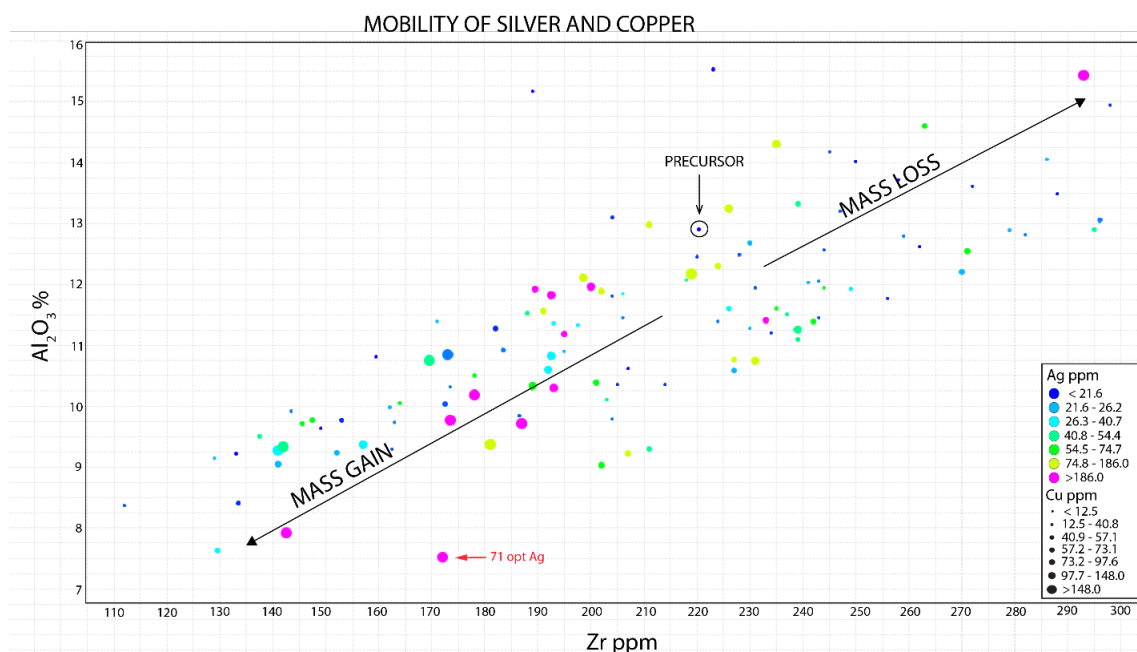


Figure 56. $\text{Al}_2\text{O}_3\%$ vs. Zr (ppm) immobility plot showing high silver (color of data points) and copper (size of data points) concentrations are related to overall mass gain including the high-grade assay interval of 71 opt Ag. Data are from intercepts of core hole ERC14-002. The 71 opt Ag is from the mixed zone in the Rochester Formation. The precursor data point is the average of nine intercepts in the Rochester Formation that assayed <0.25 opt Ag.

silicification or veining are not responsible for high silver grades. Regardless, this is evidence that residual enrichment is likely not the cause of higher silver grades in the oxide zone.

Additionally, if residual enrichment was the cause for high silver grades in the oxide and mixed zones the density of rock would be expected to decrease with increasing silver grade. Samples from ERC14-002 were measured for specific gravity to test this. Eight samples from the oxide zone were measured with grades ranging from 0.41 to 3.31 opt Ag. From the mixed zone 11 samples were measured with grades ranging from 0.21 to 71.92 opt Ag. Six samples from the sulfide zone were measured with grades ranging from 0.02 to 0.59 opt Ag. In ERC14-002 the specific gravities were inconspicuously different among varying silver grades between the oxide, mixed, and sulfide zones (Fig. 57). The specific gravities in the sulfide zone are slightly higher

	<p>Footage: 351.1' Weathering zone: Oxide Grade: 3.31 opt Ag</p> <p>SG: 2.67</p>
	<p>Footage: 463.8' Weathering zone: Oxide Grade: 0.41 opt Ag</p> <p>SG: 2.47</p>
	<p>Footage: 624.8' Weathering zone: Mixed Grade: 0.28 opt Ag</p> <p>SG: 2.58</p>
	<p>Footage: 790.2' Weathering zone: Mixed Grade: 70.92 opt Ag</p> <p>SG: 2.70</p>
	<p>Footage: 1245.7' Weathering zone: Sulfide Grade: 0.59 opt Ag</p> <p>SG: 2.98</p>
	<p>Footage: 1306.4' Weathering zone: Sulfide Grade: 0.09 opt Ag</p> <p>SG: 2.77</p>

Figure 57. Samples of varying silver grade from core hole ERC14-002 measured for specific gravity from the oxide, mixed, and sulfide zones.

(up to 1.2 times greater) than in the mixed and oxide zone but not enough to increase silver concentration by five to 120 times as observed in the Weaver and Rochester Formations. Specific gravity measurements were based on Archimedes principle and pore spaces were not completely saturated, therefore these are minimum estimates and oxide zone densities could be higher, further disproving residual enrichment.

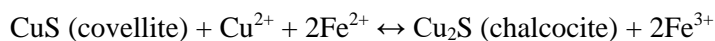
Increases in arsenic, copper, lead, and zinc concentrations are also generally related to mass gain in ERC14-002 (Fig. 56, 58A, 59). Arsenic, copper, lead, and zinc are known mobile elements in oxygenated and acidic meteoric environments (Williams, 1990; Lawrance, 2007). The most common explanation of acidic meteoric fluids in the supergene environment of ore deposits comes from the weathering of pyrite summarized by the following reactions (Sillitoe, 2005):



Arsenopyrite also readily oxidizes during supergene alteration, forming aqueous sulfuric and arsenous acids as summarized by the following reactions (Corkhill and Vaughn, 2009):



Supergene alteration of chalcopyrite and covellite in copper-porphyry deposits (Brimhall et al., 1985; Williams, 1990; Sillitoe, 2005), can generally be explained by the following reactions (Williams, 1990; Sillitoe, 2005):



Relating copper concentrations to mass gain at Rochester is additional evidence for supergene processes mobilizing copper during oxidation, as well as other elements, and re-precipitating as secondary sulfides under reducing conditions.

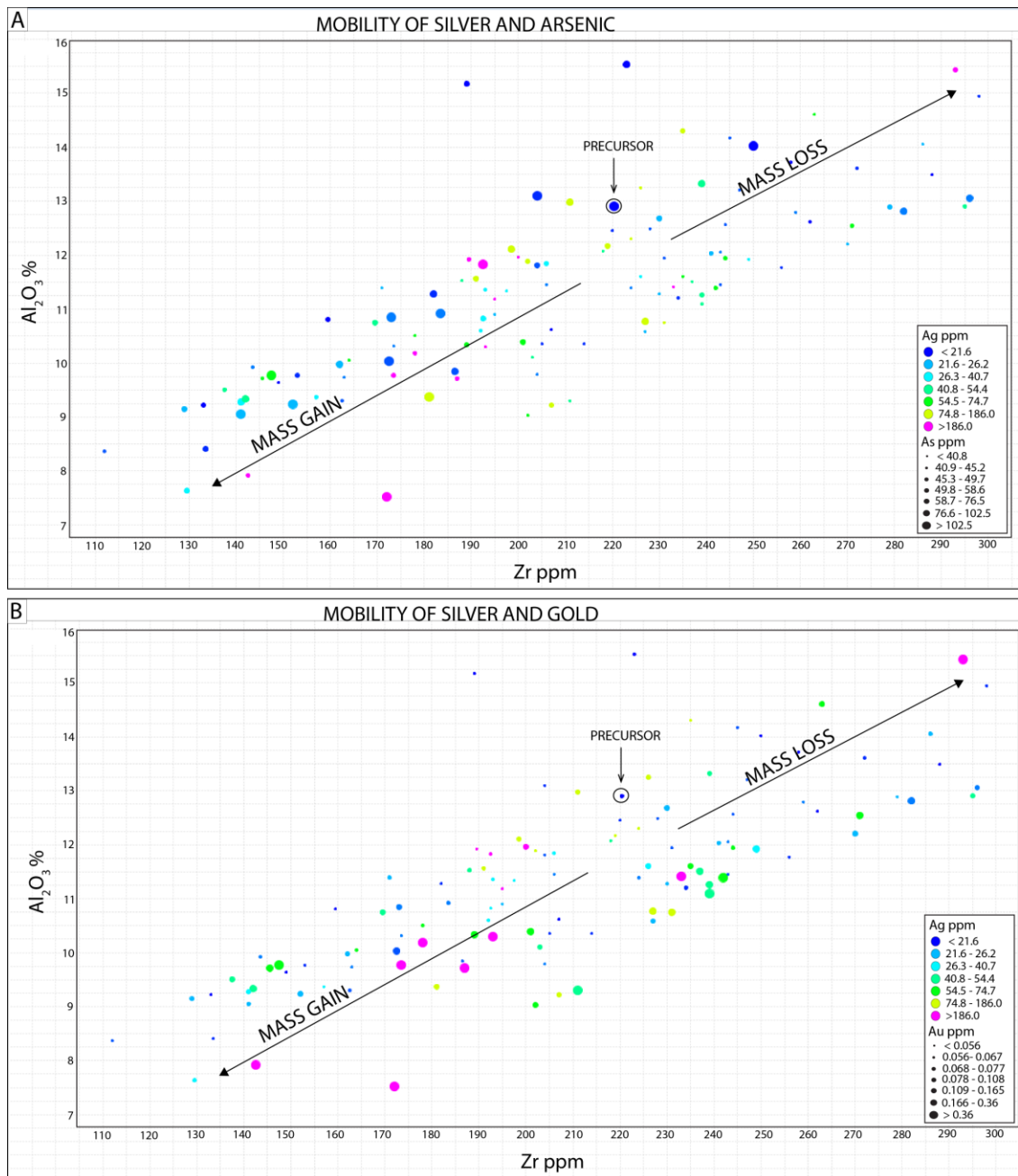


Figure 58. $\text{Al}_2\text{O}_3\%$ vs. Zr (ppm) immobility plots. **A.** Arsenic (size of data points) and silver (color of data points) concentrations showing generally increases in arsenic and silver are related to mass gain. **B.** Gold (size of data points) and silver (color of data points) showing increases in gold concentrations are related to both mass gain and either no mass change or small mass losses.

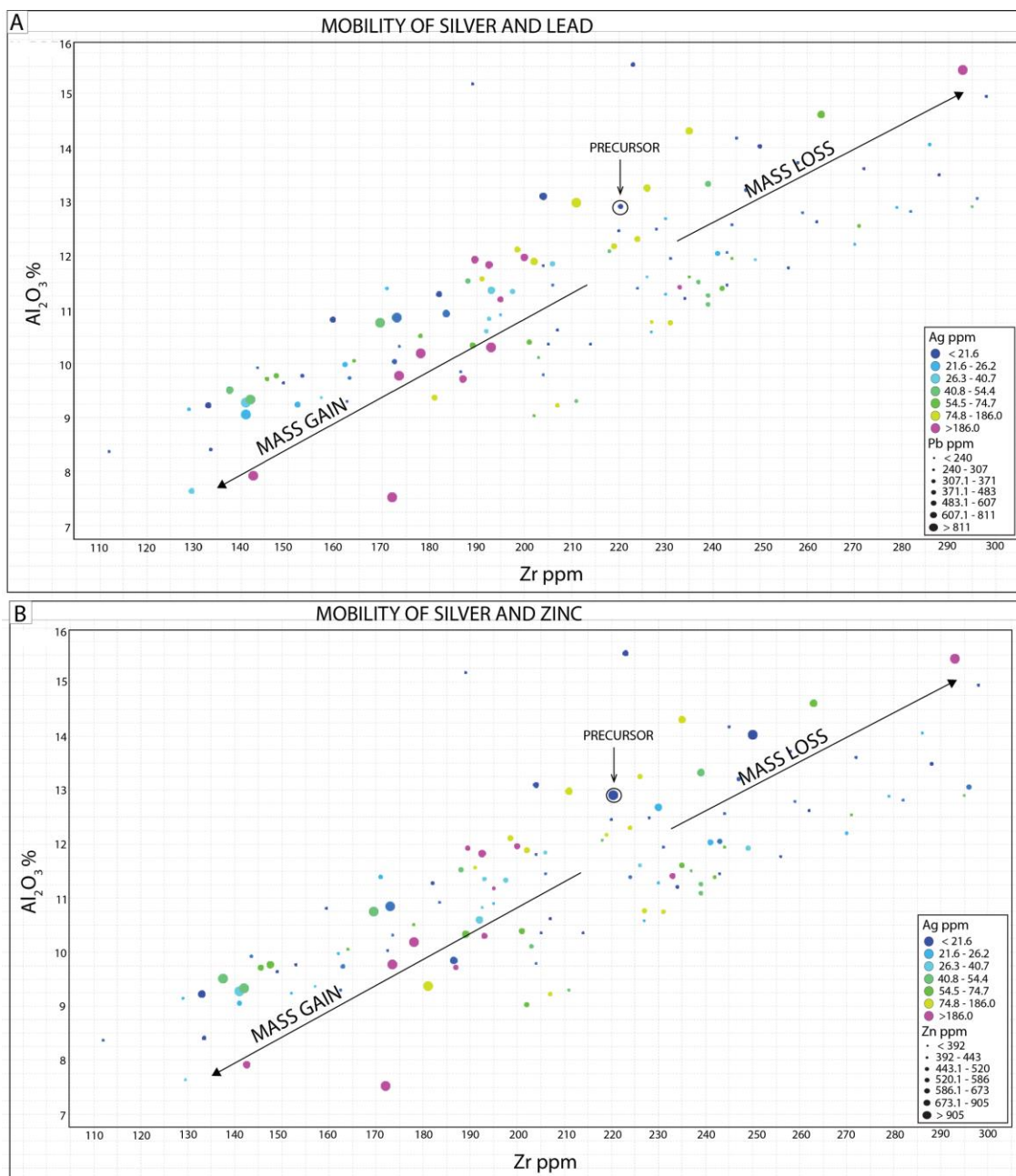
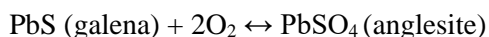
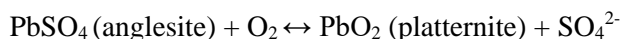


Figure 59. $Al_2O_3\%$ vs. Zr (ppm) immobility plots. **A.** Lead (size of data points) and silver (color of data points) concentrations showing lead is mainly related to mass gain. **B.** Zinc (size of data points) and silver (color of data points) concentrations showing increases in zinc are mainly related mass gain.

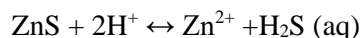
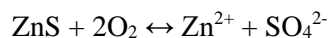
The oxidation of galena under acidic conditions will typically yield anglesite explained by the simplified reaction:



Lead-sulfate(II) is much less soluble than copper, zinc, iron, and manganese but will still dissolve much easier than lead-sulfide (Williams, 1990). Further oxidation of anglesite can result in lead-oxides, such as plattnerite:



Sphalerite can be highly soluble under numerous conditions including from interaction with oxygenated groundwater, oxidized iron, or acidic fluids from weathering sulfides summarized by the following reactions (Heidel et al., 2011):



Supergene sphalerite has been documented forming significant enrichment blankets under the right conditions occurring both as framboidal aggregates, and coating pyrite and hypogene sphalerite (Bawden et al., 2003). Gold is related to both mass gain and minor mass loss (Fig. 58B) possibly suggesting some enrichment of gold.

Clays (kaolinite, montmorillonite, gibbsite) can often develop in the supergene environment due to destruction of feldspars and micas by downward percolating acidic fluids. Samples were analyzed using the ASD Terraspec Spectrometer from core hole ERC14-002 to detect any supergene clays. Thirteen samples from the oxide zone were analyzed ranging in grade from 0.23 to 3.31 opt Ag. From the mixed zone 14 samples were analyzed ranging in grade from 0.08 to 71.92 opt Ag. Only two samples from the sulfide zone were analyzed. Muscovite and illite were the only alteration minerals identified using the spectrometer. The muscovite is part of the quartz+sericite±pyrite (QSP) hypogene alteration assemblage. The absence of

abundant kaolinite and alunite reflect the pH of the weathering fluid, possibly suggesting it was not strongly acidic.

VI. Geochronology

Jarosite was dated by the $^{40}\text{Ar}/^{39}\text{Ar}$ method to place timing constraints of weathering and supergene processes. Jarosite was identified and confirmed using SWIR spectroscopy in two samples, NPWS 45 and NPWR 41, from Rochester rhyolite collected during pit mapping.

Jarosite occurred in these samples with goethite and hematite coating fractures. Jarosite was separated from the two samples by hand and sent to the New Mexico Geochronology Research Laboratory at the New Mexico Bureau of Geology and Mineral Resources. Samples were then analyzed by x-ray diffraction to confirm jarosite abundance and purity. The jarosites were step-heated with a Photon Machine Diode laser and wrapped in silver packets to aid in removal of reactive gases. The silver packets were crimped with platinum and were analyzed with a Thermo Helix MC Plus mass spectrometer. Both jarosite samples yielded saddle-shaped and highly disturbed Ar release spectra. $^{40}\text{Ar}/^{39}\text{Ar}$ dates of the two jarosite samples yield maximum ages of 2.77 ± 0.28 and 3.39 ± 0.19 Ma (Fig. 60 and 61) based on isochron ages. Older apparent ages (Table 2) and increasing radiogenic yields at higher temperatures suggest contamination by older material with excess Ar, which is common in jarosite age analyses.

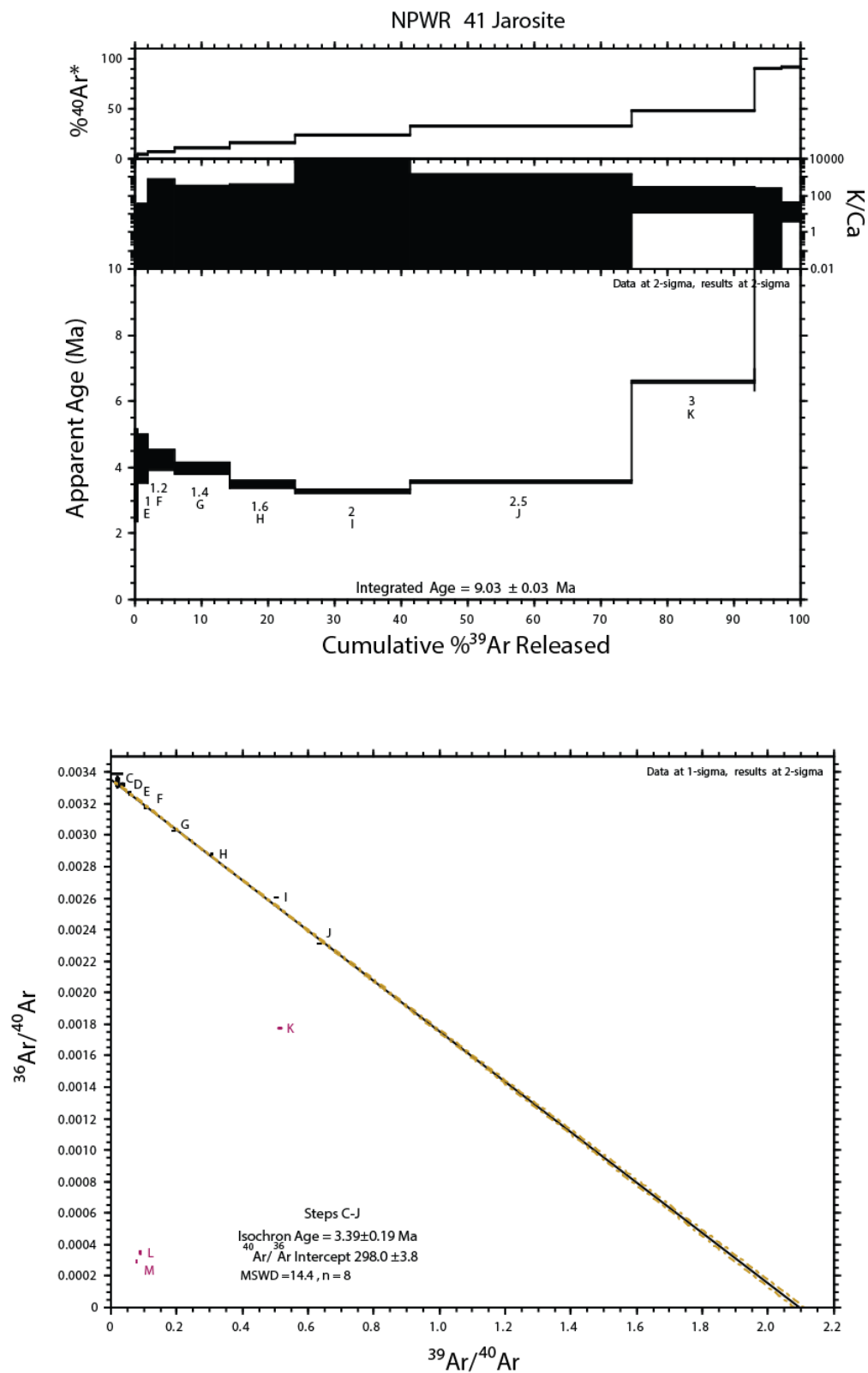


Figure 60. $^{40}\text{Ar}/^{39}\text{Ar}$ age spectra for NPWR 41 jarosite sample from the Rochester pit.

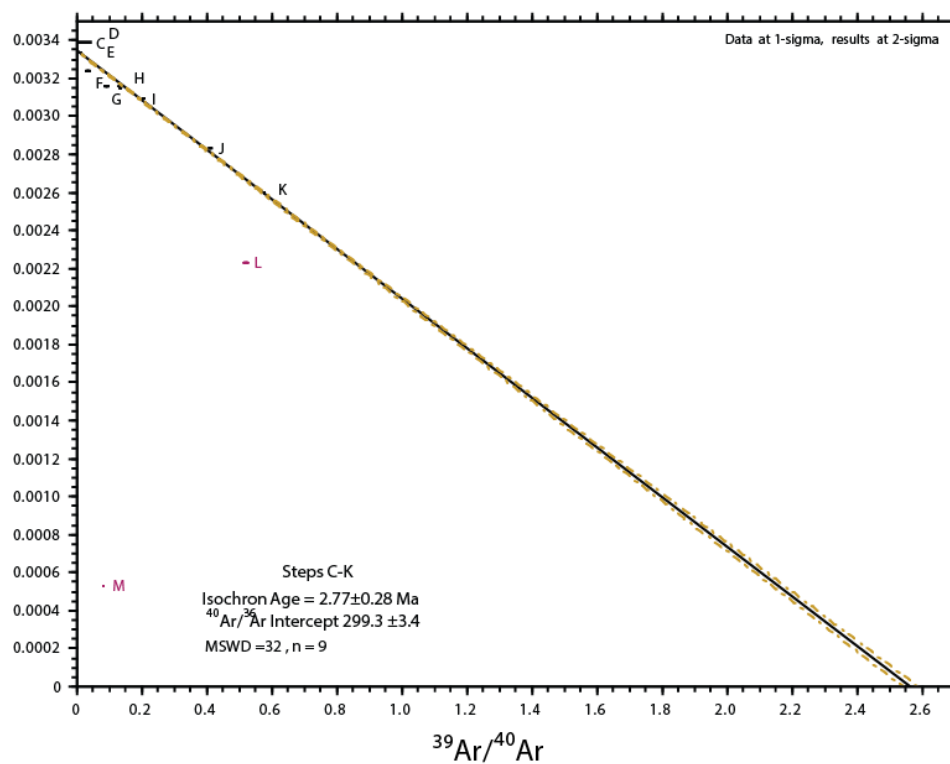
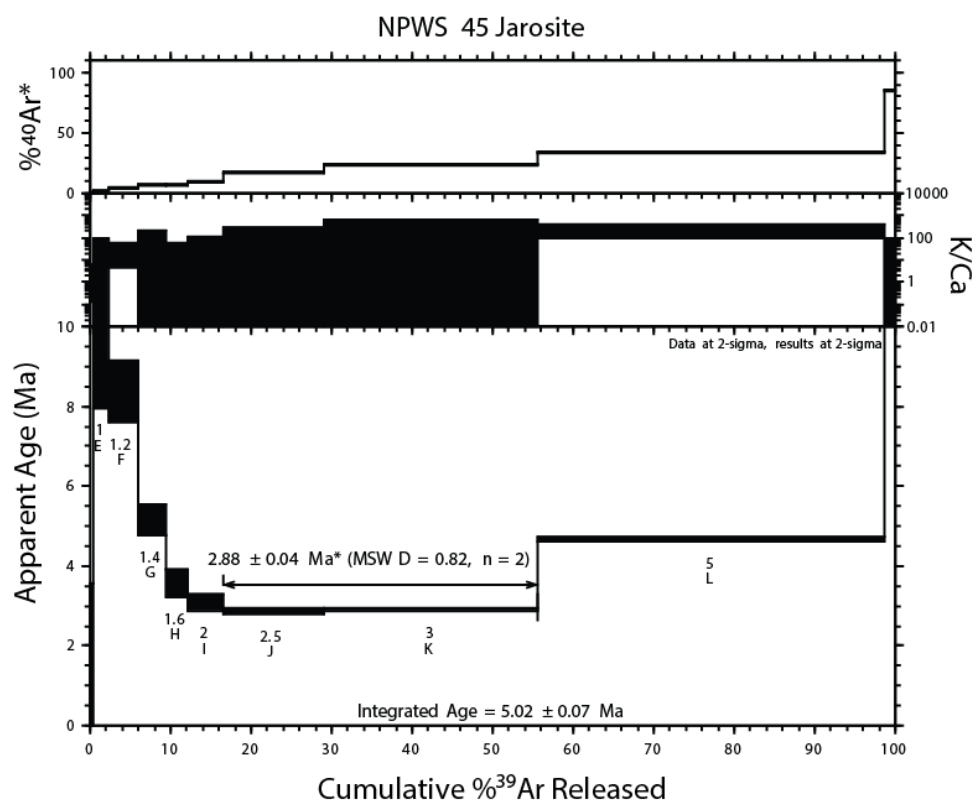


Figure 61. $^{40}\text{Ar}/^{39}\text{Ar}$ age spectra for NPWS 45 jarosite sample from the Rochester pit.

Table 2. $^{40}\text{Ar}/^{39}\text{Ar}$ analytical data.

ID	Power (Watts)	$^{40}\text{Ar}/^{39}\text{Ar}$	$^{37}\text{Ar}/^{39}\text{Ar}$	$^{36}\text{Ar}/^{39}\text{Ar}$ ($\times 10^{-3}$)	$^{39}\text{Ar}_K$ ($\times 10^{-15}$ mol)	K/Ca	$^{40}\text{Ar}^*$ (%)	^{39}Ar (%)	Age (Ma)	$\pm 1\sigma$ (Ma)
NPWS 41 , Jarosite, 3.01 mg, J=0.0038829 \pm 0.02%, IC=1.003935 \pm 0.0017263, NM-284J, Lab#=65155-01, Argus VI										
X C	0.6	43.04	0.4991	143.7	0.1	1.0	1.4	0.1	4.27	2.75
X D	0.8	25.98	0.0551	86.12	1.5	9.3	2.0	0.6	3.74	0.70
X E	1.0	16.71	0.0326	54.49	4.4	15.7	3.6	2.1	4.25	0.37
X F	1.2	9.359	0.0036	29.65	11.4	141.3	6.3	6.0	4.20	0.16
X G	1.4	5.194	0.0042	15.67	24.2	122.9	10.7	14.3	3.94	0.08
X H	1.6	3.251	0.0037	9.326	28.3	139.5	15.0	24.1	3.46	0.05
X I	2.0	1.988	0.0004	5.151	50.4	1237.8	23.2	41.4	3.26	0.03
X J	2.5	1.576	-0.0007	3.618	96.7	-	31.8	74.6	3.54	0.02
Xi K	3.0	1.945	0.0034	3.425	53.8	148.5	47.8	93.1	6.57	0.02
Xi L	5.0	11.03	0.0065	3.788	12.1	78.4	89.8	97.3	69.04	0.08
Xi M	7.0	12.63	0.0251	3.610	8.0	20.3	91.6	100.0	80.33	0.13
Integrated age $\pm 2\sigma$			n=11		290.9	153.6	K2O=9.56%		9.03	0.03
Isochron$\pm 2\sigma$ steps C-J			n=8	MSWD=14.36		$^{40}\text{Ar}/^{36}\text{Ar}=298.0\pm 3.8$			3.39	0.19
NPWS 45 , Jarosite, 3.01 mg, J=0.0038845 \pm 0.02%, IC=1.003935 \pm 0.0017263, NM-284J, Lab#=65157-01, Argus VI										
X C	0.6	1104.9	1.709	3738.6	0.1	0.30	0.0	0.1	1.94	18.52
X D	0.8	267.2	0.1717	906.2	1.0	3.0	-0.2	0.4	-4.51	4.04
X E	1.0	90.05	0.0174	299.8	5.6	29.4	1.6	2.4	10.37	1.22
X F	1.2	26.42	0.0181	85.41	10.6	28.1	4.5	6.1	8.35	0.39
X G	1.4	10.59	-0.0054	33.37	9.7	-	6.8	9.5	5.13	0.19
X H	1.6	7.356	0.0188	23.18	7.7	27.1	6.8	12.3	3.55	0.17
X I	2.0	4.886	0.0107	15.06	12.4	47.5	8.8	16.7	3.05	0.11
J	2.5	2.436	0.0041	6.861	35.3	125.7	16.5	29.2	2.85	0.04
K	3.0	1.742	0.0018	4.490	75.0	278.3	23.5	55.7	2.90	0.03
Xi L	5.0	1.922	0.0022	4.263	121.4	228.8	34.2	98.7	4.65	0.02
Xi M	7.0	12.31	0.0187	6.434	3.8	27.3	84.6	100.0	72.51	0.23
Integrated age $\pm 2\sigma$			n=11		282.6	92.3	K2O=9.28%		5.02	0.07
Plateau $\pm 2\sigma$ steps J-K			n=2	MSWD=0.82	110.259	229.409 \pm 215.7 ϵ		39.0	2.88	0.04
Isochron$\pm 2\sigma$ steps C-K			n=9	MSWD=32.34		$^{40}\text{Ar}/^{36}\text{Ar}= 299.3\pm 0.6$			2.77	0.28
Notes:										
Isotopic ratios corrected for blank, radioactive decay, and mass discrimination, not corrected for interfering reactions.										
Errors quoted for individual analyses include analytical error only, without interfering reaction or J uncertainties.										
Integrated age calculated by summing isotopic measurements of all steps.										
Integrated age error calculated by quadratically combining errors of isotopic measurements of all steps.										
Plateau age is inverse-variance-weighted mean of selected steps.										
Plateau age error is inverse-variance-weighted mean error (Taylor, 1982) times root MSWD where MSWD>1.										
Plateau error is weighted error of Taylor (1982).										
Decay constants and isotopic abundances after Minn et al., (2000).										
# symbol preceding sample ID denotes analyses excluded from plateau age calculations.										
Weight percent K ₂ O calculated from ^{39}Ar signal, sample weight, and instrument sensitivity.										
Ages calculated relative to FC-2 Fish Canyon Tuff sanidine interlaboratory standard at 28.201 Ma										
Decay Constant (LambdaK (total)) = 5.463e-10/a										
Correction factors:										
$(^{39}\text{Ar}/^{37}\text{Ar})_{\text{ca}} = 0.0006946 \pm 0.000017$										
$(^{36}\text{Ar}/^{37}\text{Ar})_{\text{ca}} = 0.0002606 \pm 0.0000005$										
$(^{38}\text{Ar}/^{39}\text{Ar})_K = 0.01261$										
$(^{40}\text{Ar}/^{39}\text{Ar})_K = 0.007531 \pm 0.000105$										

VII. Interpretation of the Supergene Profile at Rochester

The supergene profile at Rochester is a result of multiple magmatic, hydrothermal, tectonic, and weathering events over the last ~248 million years (Fig. 62). Koipato Group volcanic rocks and associated intrusions erupted upon and intruded the Golconda allochthon in the Early Triassic. Hydrothermal alteration, likely related to Koipato magmatism, was the initial event to alter Koipato Group rocks, characterized by sodium and initial boron metasomatism and hydrolytic alteration (Vikre, 2014).

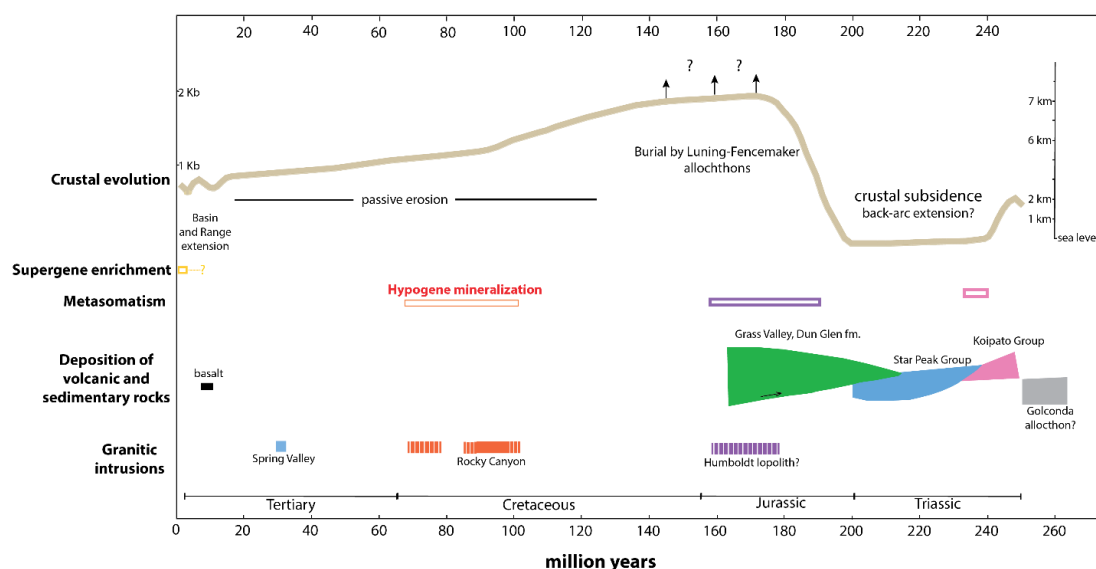


Figure 62. Schematic timeline of the geologic events in the Humboldt Range. (Modified from Vikre, 2014).

After Koipato volcanism, deposition of up to 3.6 km of marine, predominantly platform carbonates, of the Star Peak Group buried the Koipato Group (Vikre, 1981). The Humboldt mafic intrusive complex (Johnson and Barton, 2000), best exposed in the nearby Buena Vista Hills, West Humboldt, and Stillwater Ranges, is inferred to underlie the Humboldt Range based on Rb-Sr data from pervasively altered Koipato rocks giving an age of 168.6 ± 9.3 Ma (Kistler and Speed, 2000). Jurassic thrust faulting and emplacement of Luning-Fencemaker allochthon, post Humboldt mafic intrusive complex, occurred between ~190-165 Ma based on $^{40}\text{Ar}/^{39}\text{Ar}$

geochronology (Wyld et al., 2003). The Luning-Fencemaker allochthon, comprised of thrust sheets of mainly basinal siliciclastic rocks, buried the Koipato and Star Peak Groups (Wyld, 2002; Wyld et al., 2003). The thickness of the Luning-Fencemaker allochthon is estimated to be between 7 to 14 km, based on lower greenschist metamorphic facies, penetrative foliation, conodont coloration, illite-muscovite crystallinity, and $^{40}\text{Ar}/^{39}\text{Ar}$ geochronology (Heck, 1987; Elison and Speed, 1989; Wyld et al., 2003; Vikre, 2014). Based on these data, Star Peak and Koipato Group rocks would have been subjected to lithostatic pressures and temperatures of ≥ 1.8 kb and $\sim 200\text{-}350^\circ\text{C}$ (Vikre, 2014). Vikre (2014) suggested Jurassic magmatism and tectonism was responsible for regional, pervasive QSP alteration of the Koipato Group rhyolite and is cospatial with penetrative deformation caused by the thrusting.

Several Cretaceous intrusions including the $\sim 92\text{-}90$ Ma quartz monzonite Rocky Canyon stock and inferred intrusions ranging from $>103\text{-}86$ Ma and $\sim 81\text{-}70$ Ma based on K-Ar and $^{40}\text{Ar}/^{39}\text{Ar}$ dates resulted in quartz-sericite-sulfide veins, and alteration assemblages of quartz-andalusite-dumortierite-muscovite (QADM) and QSP in surrounding rocks (Vikre, 2014). The association of Cretaceous magmatism and QSP alteration is supported by δD and $\delta^{18}\text{O}$ isotope values from dated vein muscovite reflecting, in part, equilibrium with magmatic fluid. Also, isotopic values from fluid inclusions in dated QADM and quartz+muscovite+sulfide veins reflect mixing of meteoric and magmatic water. Fluid inclusion and mineral stabilities indicate QADM mineral assemblages formed at $550\text{-}400^\circ\text{C}$ and 1-2 kb (Vikre, 2014).

$^{40}\text{Ar}/^{39}\text{Ar}$ dates on muscovite from Rochester deposit veins support a Late Cretaceous age for mineralization (Vikre, 2014). Three-phase CO_2 -bearing fluid inclusions from Vikre (1981) contain 2.0 to 8.1 weight percent NaCl equivalent with no evidence for entrapment of separate CO_2 -rich and H_2O -rich fluids. Based on fluid salinities, CO_2 concentrations, and estimated entrapment temperatures, Koipato Formation strata were under pressures of 0.5 to 1.5 kb in the Late Cretaceous. Assuming an average density for post Koipato carbonate and clastic rocks of

2.5 g/cm³, 0.5 to 1.5 kb of lithostatic pressure corresponds to depths of 2 to 6 km. However, sphalerite geobarometry shows a formation pressure of $1,850 \pm 250$ bars corresponding to a depth of ~7.1 km. Vikre 1981 studies indicate vein formation conditions of $\geq 300^\circ\text{C}$ and ~1 kb. Based on vein fluid and mineral compositions, as well as temperature and pressure data, rocks at Rochester require a minimum overburden of 3.8 km assuming lithostatic pressure during mineralization (Vikre, 1981; 2014). Assuming Jurassic Luning-Fencemaker allocthon thicknesses of 7-14 km and <3.6 km of overlying Star Peak Group, most of the allocthon would have been removed by the time of ore formation in the Late Cretaceous.

Late Cretaceous thermal activity was followed by slow regional cooling, tectonic quiescence, slow erosion, and minimal deposition through the late Eocene (Colgan et al., 2006). The early Oligocene to middle Miocene is marked by widespread eruption of volcanic rocks across western Nevada. Although minor Tertiary rocks occur within the core and western flank of the Humboldt Range, faulted Oligocene to Pliocene volcanic rocks occur in the hanging wall of the Humboldt Range bounding normal fault (e.g., Wallace et al., 1969) suggesting the onset of extension and any significant erosion of the interior of the Humboldt Range commenced after the Oligocene. Accordingly, apatite fission track (AFT) dates from the footwall of normal faults bounding the western flank of the Humboldt Range yield age dates of 14.5 to 10.1 Ma, indicating the likely initiation of Basin and Range extension in this area (Schweickert et al., 2006).

Assuming a 30°C/km geothermal gradient and closure temperature of $110 \pm 10^\circ\text{C}$ for apatite (Green et al., 1986; Gallagher et al., 1998; Ketcham et al., 2007), these rocks would have been at paleodepths of ~3-3.5 km at the onset of extension. Young erosional surfaces that preserve late Miocene basalt and Pleistocene gravels, dominantly along the eastern and northwestern flanks of the Humboldt Range (Bonham and Sharp, 1957; Wallace et al., 1969b; Vikre, 1977), suggest little erosion since ~12-9 Ma (Vikre, 1977). Together, these data suggest minimal erosion (~1 km) from the time of primary mineralization in the Late Cretaceous to the initiation of Basin and

Range faulting and significant erosion of ~3-3.5 km in the middle Miocene, followed by active but reduced rates of extension after the Pleistocene. This is consistent with AFT and apatite U/Th(He) thermochronology from the adjacent East Range, which suggests extension began at 17-15 Ma with initial rapid exhumation of ~5 km, then renewed exhumation at ~10 Ma with an additional >1 km of exhumation (Fosdick and Colgan, 2008). These dates are also in agreement with regional estimations for the onset of extension including the Shawave Range west of the Humboldt Range with initiation at 14.5 Ma (Whitehill et al., 2008) and ~12 Ma across northwestern Nevada (Colgan et al., 2006).

Supergene oxidation of ore deposits has been dated from a variety of deposits and minerals across Nevada. Arehart et al. (1992) dated supergene alunite from the Post, Gold Quarry, and Rain Carlin-type gold deposits in northeast Nevada using the K-Ar technique. Dates range from ~8 to 26 Ma. Alunite from the Alligator Ridge Carlin-type gold deposit in eastern Nevada yield K/Ar supergene ages of ~13 to 10 Ma (Ilchick, 1990). Supergene alunite from the Paradise Peak epithermal Au-Ag-Hg deposit was dated by K/Ar at 10.0 ± 0.5 Ma (Sillitoe and Lorson, 1994). Supergene jarosite was dated from Goldfield, NV by the $^{40}\text{Ar}/^{39}\text{Ar}$ dating technique at 10.6 ± 0.2 Ma (Vasconcelos et al., 1994). Paradise Peak and Goldfield are located in southwestern Nevada, approximately 150 and 250 km south of Rochester, respectively. The preponderance of middle to late Miocene dates indicate Basin and Range extension was responsible for the onset of weathering and supergene processes across much of Nevada. As described above, $^{40}\text{Ar}/^{39}\text{Ar}$ dates on supergene jarosite from Rochester yield ages of ~3 Ma, indicating either weathering is relatively recent or was prolonged compared to other weathered deposits across Nevada.

At the inception of Basin and Range extension, mid-late Miocene fauna indicate the climate was highly seasonal as evident from abundant silt and salt in paleosols, likely due to dry summers and wet winters. Arid late-summers likely produced highly alkaline groundwater

(Retallack, 2004). Estimates for the mean annual precipitation during this time is about 600-1000 mm with mean annual temperature ranging from 8 to 18°C (Wolf, 1994; Graham, 1999; Retallack, 2004). The water table would have fluctuated seasonally but was likely shallow given the wet climate. The ~3 Ma date on supergene jarosite at Rochester corresponds to a global climatic shift caused by the closing of the seaway between North and South America. This climatic shift brought warm and saline waters from the gulf to high latitudes and caused increased precipitation followed by the onset of glaciation and global cooling at ~3 Ma creating a seasonal climate that was cooler and drier (Haug and Tiedemann, 1998). In the late Holocene, cycles of both severe drought and heavy precipitation lasting between 50 to 200 years have been recorded ~33 km south of Rochester in the Carson Sink area (Adams, 2003). Today Rochester has a mean annual precipitation of about 330 mm and mean annual temperature of -6 to 20°C (Robinson et al., 2014); therefore, the climate has become more arid since extensional faulting began in the mid-Miocene, which is optimal for preservation of a supergene profile.

Basin and Range extension continues today at a likely lower rate with active faults bounding the Humboldt Range, consistent with nearby ranges (Colgan et al., 2006, Fosdick and Colgan, 2008). At the Rochester mine, the pre-mining water table was roughly at an elevation of 6,550 ft (BLM, 2016) with the now mined Nenzel Hill at 7,284 ft. The modeled water table currently sits anywhere from 70 to 300 feet below the bottom of the pit (6,425 ft) and increases in elevation to the east closer to the Black Ridge fault. About 3 km north in the Spring Valley basin (~5,500 ft) the water table sits 20 to 30 feet below the surface in alluvium (Crowl et al., 2014). There are springs along the Black Ridge fault east of the Rochester pit indicating a perched aquifer. Water in the Humboldt Range today is non-saline with Cl concentrations <200 ppm (NBMG, 2014).

When the Humboldt Range initially began to rise due to extension at ~14-10 Ma, the Rochester deposit would have been well below the water table at ~3-3.5 km depth. The deposit

would have moved closer to the water table as the water table dropped and overlying rocks were eroded due to uplift. Significant oxidation of the deposit did not start until the water table dropped to the level of the deposit. While late Miocene basalts are preserved on the eastern and northwestern flanks of the Humboldt Range no major erosional surfaces are preserved near Rochester which suggests continual active erosion. Jarosite samples yielding maximum supergene ages of ~3 Ma were collected in the pit where mining is active at an elevation of 6,425 ft. As mentioned above pre-mine Nenzel Hill was at an elevation of 7,284 ft, therefore this young supergene date is possibly when weathering processes reached lower elevations of the deposit. Depending on how thick a hypothetical and now eroded leached cap was, weathering could have started at higher elevations of the deposit much earlier and possibly as early as the onset of Basin and Range extension.

Pyrite and other sulfides at Rochester were oxidized and formed sulfuric acid. Typically, pervasive quartz+sericite alteration, such as at Rochester, has little, if any, acid-consuming capacity. The lack of alunite, kaolinite, and halloysite in the oxide zone at Rochester is consistent with observations from leached caps in porphyry copper deposits where sericite is not altered to supergene kaolinite (e.g., El Salvador, Gustafson and Hunt, 1975). Moreover, the presence of minor but widespread relict igneous and hydrothermal reactive K-feldspar likely inhibited generation of extremely acidic supergene fluids. The oxidation of pyrite led to the formation of both indigenous goethite and mobilization of iron to form exotic goethite. Much less indigenous and exotic hematite formed relative to goethite. During oxidation, acidic fluids leached mobile elements, particularly copper, silver, and zinc. Relatively immobile elements such as lead and gold were left behind. As pointed out above, gold grades >0.2 opt are restricted to elevations above 5,500 feet, and >0.5 opt between 6,000 to 7,000 feet, suggestive of original hypogene zoning (Fig. 55B).

During supergene oxidation, mobile metals, as ionic or complexed species and sulfur as sulfate, percolate downward through the vadose zone moving towards the water table.

Alternatively, fluid moving through rock with low total volume percent of sulfide and reactive wallrock mineralogy (e.g., feldspar, carbonate) will be less acidic and metal ions will not be transported as far but will precipitate in the oxide zone as carbonates, hydroxides, oxides, sulfates, or silicates. Metal ions will then reprecipitate under reducing conditions which typically occur at and below water table, but locally can exist above the water table where capillary water is present (Anderson, 1982).

The solubility of copper and silver in downward percolating oxidized fluids is dependent on pH and oxygen fugacity (Fig. 63 and 64). A decrease in pH will lead to an increase in solubility of copper and silver while an increase in pH typically leads to precipitation of copper oxides and carbonates, silver-halides, and native copper and silver. Reduction with little or no pH increase favors precipitation of copper and silver sulfides. Therefore, highly acidic and oxidized fluids are crucial for efficient leaching and transport of copper and silver down to and below the water table to form supergene sulfides.

For copper, in oxidized fluids at pH values $< \sim 4$, no solid copper phases are stable and aqueous copper is transported downward as Cu^{2+} (Fig. 63). When fluid becomes reduced at and below the water table, supergene chalcocite forms first. Covellite forms at greater depth under more reduced conditions (S^{2-} rather than S^{1-}) (Alpers and Brimhall, 1989). At pH $> \sim 4$ copper is less soluble and can precipitate in a variety of minerals dependent upon fluid chemistry, including antlerite, brochantite, cuprite, and native copper (Anderson, 1982). Neutral to high pH oxidizing conditions will not significantly leach copper but carbonates (azurite and malachite) and oxides (tenorite) will form in place or nearby (Anderson, 1982).

For silver, oxidized fluids at similar pH values of $< \sim 4$ can form chlorargyrite, iodargyrite, and native silver. At conditions where aqueous sulfide is present such as near and below the

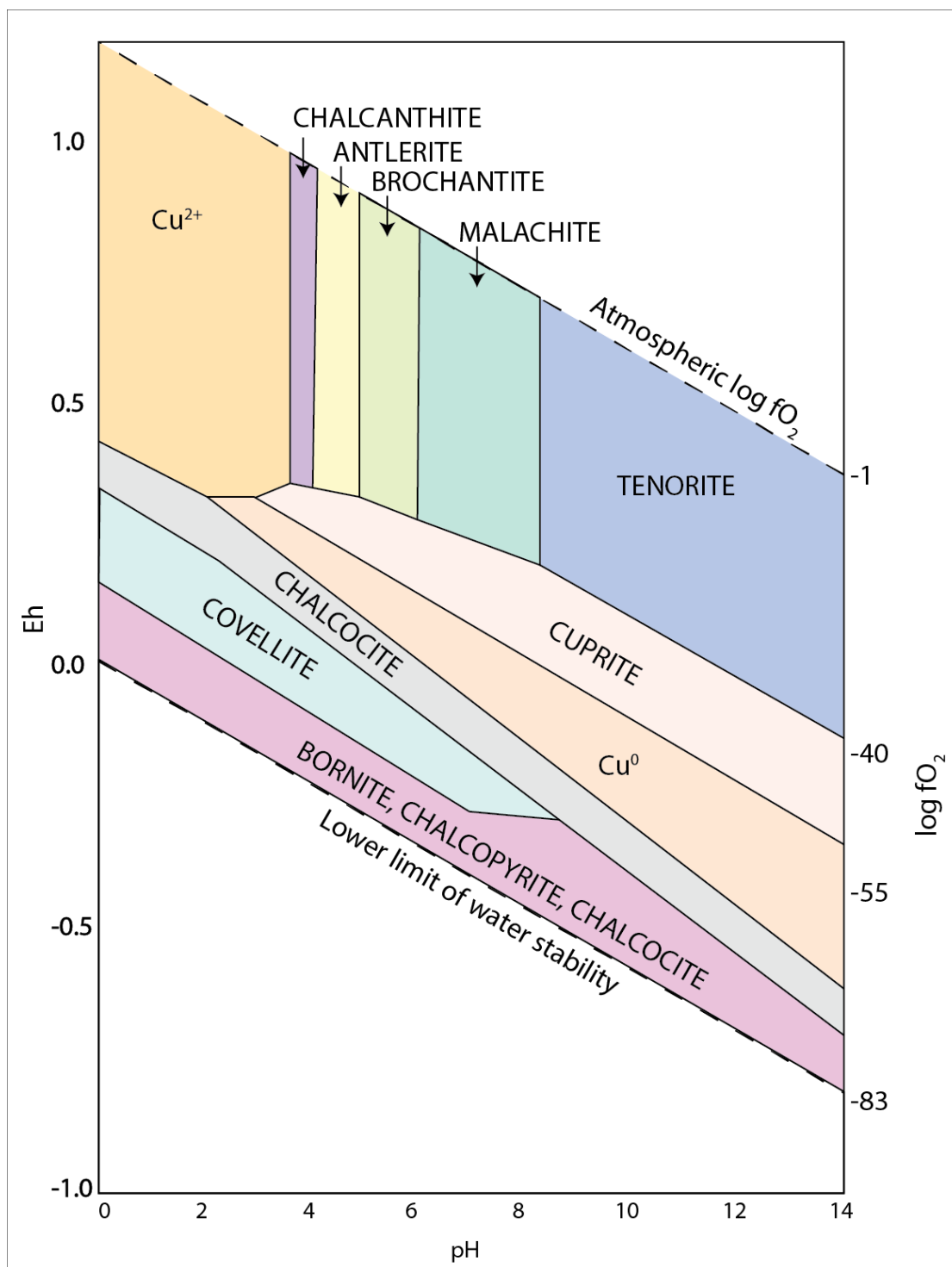


Figure 63. Eh-pH diagram showing the stability fields for copper minerals in the Cu-S-H₂O system at 25°C with $p = 1$ atm, $\text{CO}_3 = 10^{-3}$ m, and total S = 0.1 m. (Modified from Anderson, 1982).

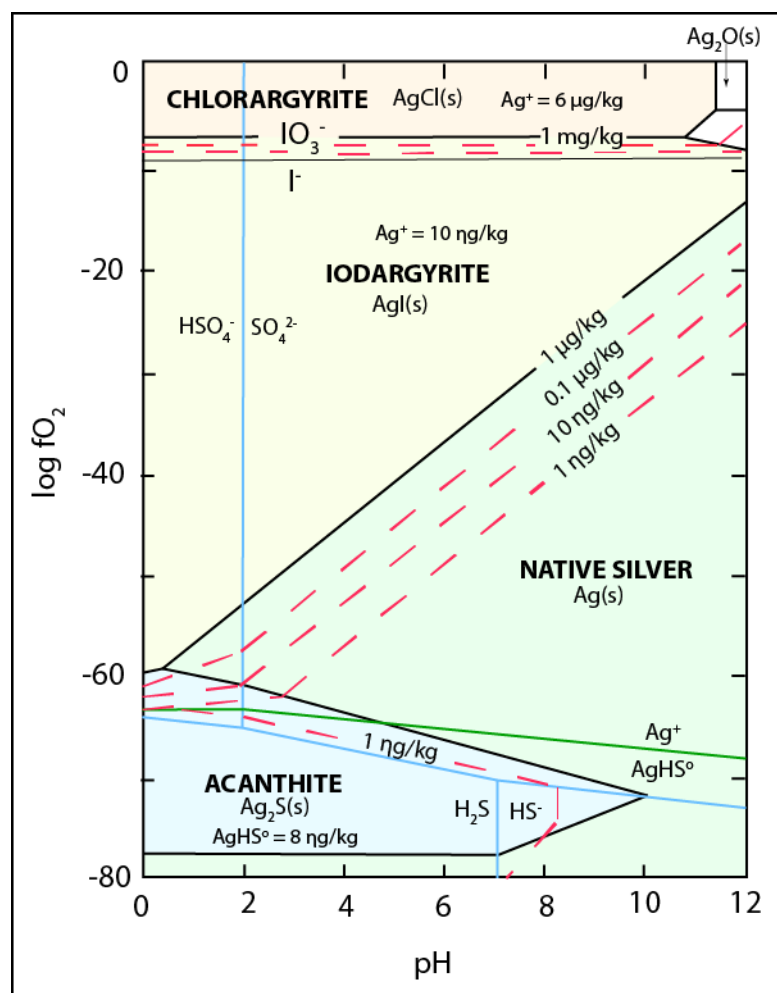


Figure 64. Oxygen fugacity vs. pH diagram showing the stability of silver minerals in the Ag-S-I-Cl-H₂O system at 25°C. Ligand concentrations represent average rain water from Hem (1985): $\Sigma S = 10^{-5}$ m, $\Sigma I = 7.9 \cdot 10^{-9}$ m, $\Sigma Cl = 2.8 \cdot 10^{-5}$ m. Blue solid lines represent boundaries between sulfur species. Green solid line represents the boundary between two silver complexes in solution, Ag^+ and $AgHS^\circ$. Black solid lines represent boundaries between silver mineral stability fields. Red dashed lines represent the solubility concentrations of silver as Ag^+ and $AgHS^\circ$. (Modified from Gammons and Yu, 1997).

water table, acanthite is stable (Fig. 64). Alternatively, acanthite will oxidize to native silver and iodargyrite. As stressed by Sillitoe (2008), the stability field of iodargyrite is quite large and iodargyrite is much less soluble than chlorargyrite and native silver. However, as pointed out by Gammons and Yu (1997), unless the supply of iodide (I) in supergene fluids is continuously

replenished, the I/Cl ratio of the groundwater, which is always <1 , will decrease until the stability field of chlorargyrite will expand at the expense of iodargyrite (Fig. 64).

Acanthite is the most common supergene silver sulfide occurring as rims on hypogene sulfides in the Rochester deposit. Covellite is a well-known secondary sulfide in supergene copper deposits and commonly occurs with acanthite on hypogene rims suggesting this supergene texture forms under the same conditions and processes. Knopf (1924) also noted acanthite and covellite rimming hypogene sulfides, dominantly sphalerite and lesser tetrahedrite, galena, and chalcopyrite. In the Rochester deposit, covellite rims without acanthite are found only in the mixed zone and in the upper parts of the sulfide zone suggesting copper moved to greater depths than silver. Rare sphalerite occurring with acanthite rimming a hypogene sulfide suggests possible supergene sphalerite, especially given most of this late sphalerite has little to no iron. In situ sulfur isotope microanalyses of the sphalerite might help evaluate a supergene origin (i.e., Bawden et al., 2003).

As the water table lowered in elevation with time due to continued uplift and decreasing precipitation, more sulfides, including previously formed supergene sulfides were exposed to weathering and oxidized, likely resulting initially in hematite formation, due to decreased S/metal ratios of supergene sulfides relative to pyrite (Anderson, 1982) (Fig. 65B). Additional silver may have been transported further downward as supergene acanthite rims were subsequently oxidized. Upon acanthite oxidation immobile silver phases will also form, primarily native silver and silver-halides. Gammons and Yu (1997) predicted a vertical zonation based on phase equilibria with iodargyrite at the base of weathering followed by bromargyrite higher in the supergene profile then chlorargyrite closest to the surface. Pure bromargyrite is rare because it forms a complete solid solution with chlorargyrite and Cl⁻ is more common in meteoric fluids compared to Br⁻. This vertical zonation was observed at Tonopah, NV with iodargyrite at depth and chlorargyrite near the surface in the zone of weathering (Chitayeva et al., 1971). On the other

hand, the opposite was observed in the Rochester deposit, where chlorargyrite and supergene native silver locally occur in the mixed oxide-sulfide zone adjacent to supergene acanthite with no iodargyrite. Iodargyrite was only found in the upper portion of the supergene profile in the oxide zone, where samples had been pervasively and strongly oxidized. This suggests iodide was not sufficiently replenished during oxidation and the I/Cl ratio decreased over time; thus, as pointed out above, the chlorargyrite stability field likely expanded at the expense of the iodargyrite field. Thus, silver solubility at low pH values and oxidized conditions would have increased with time, as the iodargyrite field shrank. Knopf (1924) and Vikre (1977) also observed supergene acanthite partially replaced by chlorargyrite in oxidized ore.

Silver from secondary sulfides either became soluble as weathering progressed and moved further down the supergene profile (Fig. 65C) or formed silver-halides nearly in place. Once the surrounding rock and hypogene sulfides are pervasively oxidized, remnant supergene acanthite can remain in the oxide zone, and subsequent supergene fluids are not sufficiently acidic to mobilize silver and other metals, unless the water table drops significantly into the underlying hypogene sulfide zone (Fig. 65D). Therefore, zones of supergene enrichment should form in the early stages of weathering but are then oxidized and largely become immobile unless the water table drops again.

Supergene enriched zones, documented in this study, mostly occur within or adjacent to fault zones near the Weaver-Rochester contact. This is likely a result of fluid movement enhanced by fracture permeability. Oxidation of these supergene sulfides in fault zones results in strongly oxidized gouge and formation of native silver and silver-halides largely responsible for silver grade. Vikre (1977) similarly observed fragments of quartz veins in fault zones with significant silver grades occurring dominantly as silver-halides suggesting mineralized veins were pulverized by faulting and the silver grade enriched due to supergene processes.

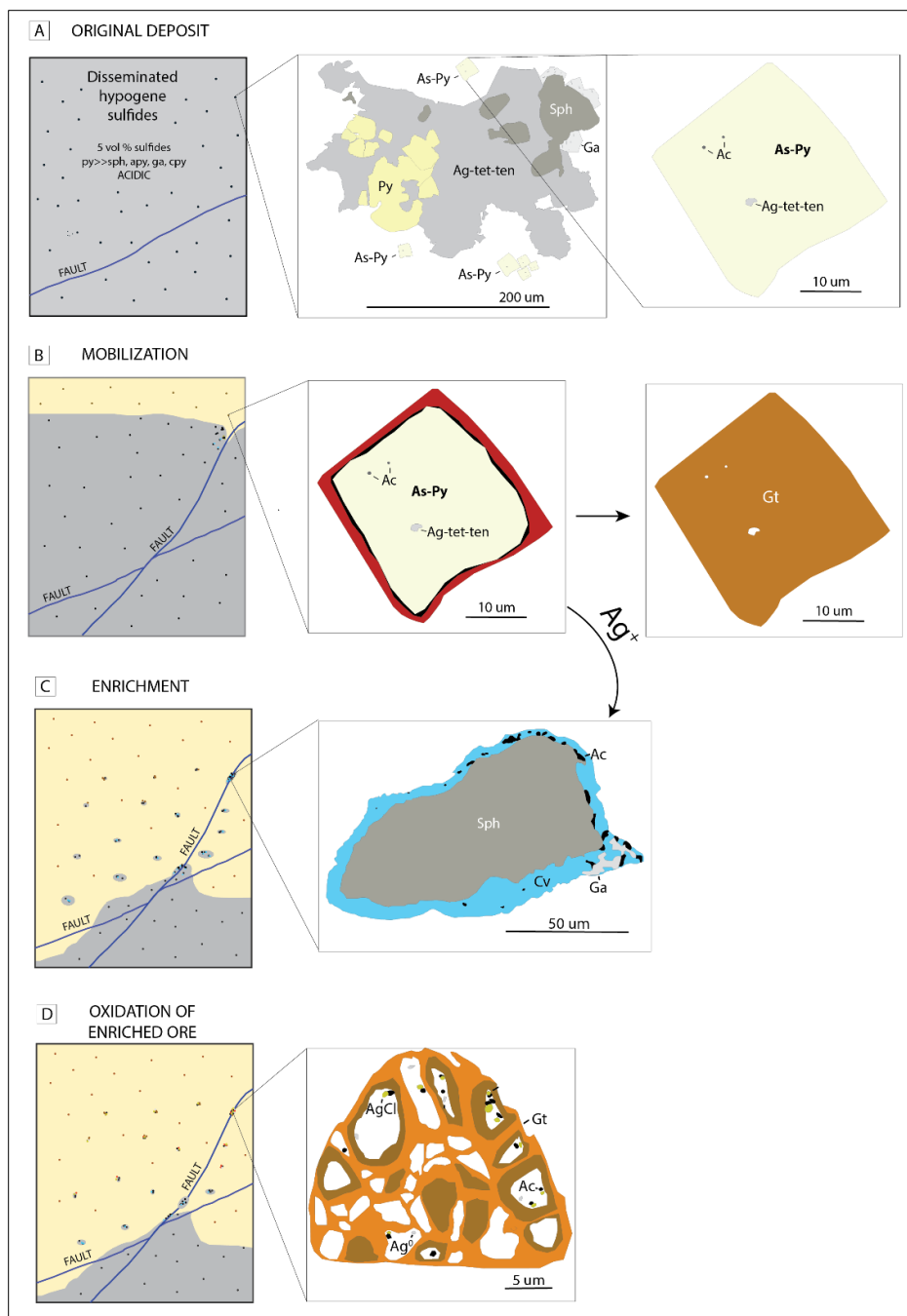


Figure 65. Schematic diagram of the interpreted supergene profile progression at Rochester. **A.** Primary hypogene sulfide assemblage dominated by silver-bearing tetrahedrite-tennantite and acanthite inclusions in arsenian pyrite. **B.** Initial oxidation of the hypogene mineralization with silver mobilizing to nearby sulfides and oxidizing to hematite then complete leaching and mobilization. **C.** Silver mobilizes down in elevation and becomes enriched mostly along fluid pathways, such as faults, precipitating as rims on hypogene and supergene(?) sulfides. **D.** Oxidation of supergene enriched silver zones creates dominantly immobile silver phases (native silver and silver-halides) and remnant supergene acanthite with indigenous and exotic goethite>hematite.

The amount of silver fixed as silver-halides and native silver depends on environmental conditions at the time supergene processes are affecting hypogene silver mineralization, which likely change over time. Environmental conditions determining the mobility of silver include the availability of halides due to the salinity of groundwater, length and periodicity of weathering, and tectonic activity causing uplift thus decreasing the elevation of the water table. Silver-halides are relatively soluble therefore continual fluid flux will transport silver down out of the weathering zone and are only preserved in arid environments (Gammons and Yu, 1997). For example, at a pH of ~2 and high oxygen fugacity the chlorargyrite field is dominant and 6 $\mu\text{g}/\text{kg}$ of Ag^+ is in the supergene fluid (Fig. 64). If this highly oxidizing, highly acidic fluid then percolated downward and increasingly became more reduced but remained acidic, Ag^+ in solution would increase to 1 mg/kg but then decrease as iodargyrite precipitates. However, as mentioned above, if I⁻ is not present in high concentrations, the chlorargyrite field expands at the expense of iodargyrite and Ag^+ will remain at 6 $\mu\text{g}/\text{kg}$. As the fluid continues to move downward Ag^+ will slightly decrease from the chlorargyrite field to 1 $\mu\text{g}/\text{kg}$ in solution and native silver becomes stable. Along this fluid pathway in the native silver field, Ag^+ will decrease to 1 ng/kg until the fluid is sufficiently reduced to form acanthite. In the acanthite field, aqueous silver is complexed as AgHS^0 , and at a concentration of 1 ng/kg . When sulfur in the fluid is predominantly aqueous sulfide, the concentration of AgHS^0 in solution will increase to 8 ng/kg in the acanthite stability field.

The large and variable mixed zone at Rochester is likely a product of the water table having dropped with time as extension uplifted the Humboldt Range. Silver likely became locked up in the oxidized upper portion of the supergene profile, mainly as halides, as the water table moved down but some silver was able to mobilize to lower elevations to the mixed zone. As silver moved down from the supergene enriched zones in the oxide zone, new enriched zones were produced in the mixed zone and those are currently being oxidized.

A copper-porphyry style blanket of secondary sulfides is not obvious at Rochester, however, the overall pattern of ≥ 2 opt silver, which is mainly in the current oxide zone, generally parallels the Weaver-Rochester contact. At this point, the possibility that this apparent stratiform body is a remnant supergene enrichment blanket cannot be ruled out. A leached capping at the Rochester deposit could have easily been eroded considering at least ~4 km of overburden has been removed since ore formation in the late Cretaceous, ~3-3.5 km of which has occurred since the middle Miocene. Various rates of erosion have likely occurred over the last 10 m.y. in conjunction with tectonic uplift as evidenced by the young supergene jarosite ages of ~3 Ma. In comparison, supergene weathering at individual deposits across the Chile copper porphyry province was ongoing for at least 0.4 to 6.2 m.y. (Sillitoe and McKee, 1996). A similar period of weathering could have enabled supergene processes at Rochester to oxidize hypogene mineralization and erode the upper portions of the deposit. Therefore, oxidized segments of an enrichment blanket could explain the high silver grades and blanket-like geometry of the Rochester deposit in the oxide zone. After initial enrichment, a blanket-like feature could have been further eroded and dismembered by continued active faulting.

To further test supergene silver enrichment at Rochester the timing of oxidation needs to be constrained and fluid flux and transport characteristics specific to Rochester mineral assemblages needs to be better understood. To constrain timing and duration of weathering more dates of minerals associated with oxidation need to be determined. This would be difficult considering the minor amounts of jarosite and absence of supergene alunite but is feasible given that jarosite from this study was pure enough to use the $^{40}\text{Ar}/^{39}\text{Ar}$ dating technique. Geochemical transport modeling using mass balance calculations similar to studies by Ague and Brimhall (1989) and Alpers and Brimhall (1989) on supergene enrichment of copper-porphyry systems are needed to understand transport and mobilization of elements in the Rochester deposit during weathering.

VIII. Regional Comparisons to other Silver-rich Districts

Historically, some silver mines in Nevada have been short lived after their shallow high-grade oxidized and upper parts of underlying sulfide portions were exploited. Ore minerals in the shallow oxide zone of some silver deposits included chlorargyrite, other silver-halides, and native silver; and electrum, native silver, acanthite, silver-bearing sulfosalts, and galena deeper in the weathering profile (Ross, 1953; Stager, 1977; Kleinhampl and Ziony, 1984). Most workers noted limonite and other oxides as vein constituents with sulfides suggesting ore was mined from the mixed oxide-sulfide zone (Page, 1959; Stager, 1977; Kleinhampl and Ziony, 1984). Summaries of short lived camps and a comparison to the Rochester deposit are provided below.

Austin, NV (Ross, 1953; Stager, 1977)

There are several mining districts near the town of Austin, NV where silver was discovered in 1862, peak production was reached in 1868, and production declined with sporadic mining into the early 1900's. Major ore deposits in this district are silver-bearing quartz veins filling joint and fault fractures in Jurassic granitic intrusions and adjacent Paleozoic sedimentary rocks.

The deposits around Austin are similar to those in the Rochester district, especially the mineralogy of both oxide and sulfide ores. At both Rochester and Austin, high-grade oxide ore near the surface is characterized by chlorargyrite, other silver-halides, and native silver, these minerals and supergene covellite and chalcocite support supergene enrichment of silver. Sulfide mineral similarities include acanthite and silver-sulfosalts, including tetrahedrite-tennantite, proustite, polybasite, stephanite, chalcopyrite, and rare molybdenite. Similar gangue minerals include quartz, pyrite, galena, sphalerite, and arsenopyrite. The presence of carbonates and graphite in the deposits at Austin, which are absent at Rochester, would have led to less acidic

and more reduced supergene fluids in the oxide zone. This fluid chemistry would have resulted in more native silver precipitating from weathering fluids at Austin.

Candelaria Mining District, NV (Page, 1959; Moeller, 1988)

The Candelaria Mining District is in southwestern Nevada, along the county line between Mineral and Esmeralda Counties. Silver-rich veins were first discovered in 1863 and mined through the 1880's. Mining operations were reactivated in 1983 and ore mined contained average grades of 1.45 opt Ag and 0.006 opt Au. Ore deposits in this district are mostly hosted in Triassic shale. The intensity and depth of oxidation is extremely variable vertically, locally extending to depths of 200 m. However, sulfide pockets locally occur within 70 m of the surface.

The most abundant sulfides in hypogene ore are pyrite, sphalerite, along with minor arsenopyrite, chalcopyrite, galena, and jamesonite. Locally, silver occurs in galena and jamesonite. Gangue minerals include quartz, dolomite, and minor rhodochrosite. Carbonaceous rocks also occur at depth. Secondary copper minerals were identified locally.

Ore from open pit mining in the 1980's came exclusively from the oxide zone. The highest silver grade zone was a gossan boxwork indicative of massive sulfide (possibly an oxidized enriched zone). This high-grade gossan was underlain by a zone of milky quartz veinlets with abundant limonite with silver grades of 1 to 4 opt. Chlorargyrite is abundant in high-grade oxidized ores and acanthite is more abundant in zones of minor limonite. Acanthite reportedly coats native silver and native silver rims were found on chlorargyrite, indicative of a supergene origin for at least some of the minable acanthite. Jarosite is a common constituent occurring as fracture coatings suggesting highly acidic supergene fluids. Other oxides reported include anglesite, cerussite, and smithsonite with limonite boxwork. Bindheimite, and other unidentifiable antimony and arsenic phases occur in the oxide zone.

Past workers had supported a hypogene zonation for silver minerals but Moeller (1988) argues for significant supergene silver migration. Two periods of oxidation are recognized; the first is constrained by Oligocene volcanics unconformably overlying a deeply oxidized zone and the second was initiated at the onset of erosion of the volcanic rocks. Moeller speculates that the water table fluctuated significantly during oxidation and the water table now lies at an unknown depth below oxidation, allowing for continuing development of a supergene profile. In the Mount Diablo ore zone, silver grade increases with depth to about 180 m suggesting supergene enrichment.

Supergene mineralization at Candelaria and Rochester are similar in that chlorargyrite is an important oxide ore mineral and acanthite occurs spatially with chlorargyrite and native silver indicative of a supergene origin for acanthite. Oxide mineralogy of the two deposits is also similar, including the presence of anglesite and bindheimite. Some important differences are carbonate and carbonaceous gangue minerals at Candelaria which would likely inhibit the mobility of silver, at least locally, in the supergene environment. This gangue mineralogy at Candelaria would result in reduced and higher pH fluids where native silver and acanthite would become more stable than chlorargyrite.

Northern Nye County, NV (Kleinhampl and Ziony, 1984)

The Reville District is located in the northern part of the Reville Range in central northern Nye County east of Tonopah. Silver, lead, copper, antimony, and zinc were mined intermittently from 1866 until 1982. Early reports of the district claimed that near surface ore was oxidized and dominated by chlorargyrite and cerussite. Chlorargyrite was mined as late as 1979 in newly discovered ore bodies hosted in Paleozoic rocks along a major south dipping fault (Kleinhampl and Ziony, 1984). Pyrargyrite and acanthite were reported to increase with depth suggestive of supergene enrichment. Locally silver-bearing galena occurs at depth in the sulfide

zone. Gossan and silicified zones surround shafts and shear zones. Ore zones are typically in veins along fractures and faults in the Paleozoic and Tertiary rocks, and along contacts between Tertiary andesite and Paleozoic carbonate and siliciclastic rocks. However, early descriptions of the ore body reported a flat blanket-like silver deposit indicative of a supergene enriched zone.

The Belmont District lies in the low hills between the southern Toquima Range and Monitor Range. This district was short lived and only active from 1865 to 1888. The district straddles a contact between a late Cretaceous granitic pluton and Ordovician sedimentary rocks. Shallow high-grade oxidized silver ores were first mined and were dominated by chlorargyrite. Deeper silver-rich ores consisted mostly of silver-bearing tetrahedrite and sulfide minerals in quartz veins, including pyrite, galena, and secondary copper minerals. Stromeayerite was reported spatially occurring with chlorargyrite suggestive of at least some supergene sulfide mineralization.

The main similarity among these districts in northern Nye County is chlorargyrite reported as the dominant ore mineral in the oxide zone occurring with secondary copper minerals. Acanthite, tetrahedrite, and minor stromeayerite are often the main sulfide ore minerals occurring in mixed oxide-sulfide and sulfide zones. However, textures of sulfide ores are not described in adequate detail to infer a hypogene or supergene origin for many of these minerals. Pyrite and sphalerite are typically the dominant hypogene sulfide minerals. These characteristics are similar to those at Rochester where chlorargyrite is a common oxide ore; acanthite and tetrahedrite with lesser stromeayerite are the main sulfide ore minerals in the mixed and sulfide weathering zone; and pyrite and sphalerite are the most common sulfides occurring in veins and as disseminations in wall rocks.

Faults, gossan, and silicified zones are reported as abundant and can be important for ore in northern Nye County indicating some high grade zones are the result of supergene processes. While fault gouge and strongly oxidized rocks often comprise high silver grade zones at

Rochester, silicification is not necessarily indicative of ore. Another difference between ore deposits in northern Nye County and Rochester is the presence of silver-bearing galena. Acanthite occurs with galena at Rochester, but silver has yet to be documented to occur in the galena crystal structure. Silver-bearing sphalerite was reported in deposits in Nye County whereas at Rochester sphalerite can be closely associated with elevated silver grades but sphalerite does not contain silver, silver-bearing supergene sulfides commonly replace sphalerite. Ore mineralogy reports for northern Nye County were written several decades ago; it is possible that galena and sphalerite do not actually contain silver in their structures and that silver occurs in very fine-grained rims or inclusions of silver-bearing sulfides and sulfosalts.

The most important characteristics these deposits share, including Rochester, are shallow high-grade oxidized ore zones with chlorargyrite as the dominant silver mineral and acanthite and silver-sulfosalts abundance increasing with depth. Most of the silver-sulfosalts are likely hypogene in origin while some could be supergene, particularly stromeyerite. Some of the acanthite texture descriptions in the Candelaria and Reveille districts are certainly suggestive of a supergene origin but more detailed petrographic descriptions are necessary for verification. The most important difference between some of the deposits described above and Rochester is the presence of carbonate and carbon which have buffering capabilities and would inhibit the mobility of silver. Alternatively, for example, downward percolating fluids that encountered a lithologic contact between volcanic rocks and carbonaceous limestone would promote locally efficient precipitation of metals resulting in supergene enrichment. At Rochester, no carbonate or carbon material is present and with pervasive QSP alteration there is little buffering capabilities allowing the fluid to remain acidic and transport metals. Therefore, if a similar deposit style was characterized by shallow high-grade oxidized ore dominated by chlorargyrite with no carbonate or carbon gangue minerals in an environment similar to Nevada with a structural framework and

recent aridity to preserve supergene minerals, then a deeper large disseminated silver deposit similar to Rochester is possible.

IX. Conclusions

Supergene silver enrichment was documented in this study, occurring predominantly as acanthite with covellite rimming earlier sulfides. Supergene enrichment was mostly found in high grade zones (≥ 2 opt Ag) related to faulting. Identifying and understanding geologic controls on high grade zones is important for future mine planning and exploration to vector in potential targets. A supergene enrichment blanket responsible for the tabular geometry of higher silver grades in the lower Weaver oxide and upper Rochester oxide and mixed zones cannot be ruled out. Further testing this possibility is hindered by the lack of Weaver sulfide protore samples for comparison to high-grade Weaver oxide ore. Future work that can further test supergene silver enrichment at Rochester includes geochemical modeling similar to studies by Ague and Brimhall (1989) and Alpers and Brimhall (1989) of chalcocite enrichment blankets in copper porphyry deposits, as well as additional dating to better constrain the timing and duration of supergene processes during late Cenozoic uplift and erosion of the Humboldt Range.

References

- Adams, K.D., 2003, Age and paleoclimatic significance of late Holocene lakes in the Carson Sink, NV, USA: *Quaternary Research*, v. 60, pp. 294-306.
- Ague, J.J., and Brimhall, G.H., 1989, Geochemical Modeling of Steady State Fluid Flow and Chemical Reaction during Supergene Enrichment of Porphyry Copper Deposits: *Economic Geology*, v. 84, pp. 506-528.
- Alpers, C.N. and Brimhall, G.H., 1989, Paleohydrologic Evolution and Geochemical Dynamics of Cumulative Supergene Metal Enrichment at La Escondida, Atacama Desert, Northern Chile: *Economic Geology*, v. 84, pp. 229-255.
- Anderson, J.A., 1982, Characteristics of leached capping and techniques of appraisal, in Titley, S.R., ed., *Advances in geology of the porphyry Copper deposits, southwestern North America*: Tucson, University of Arizona Press, p. 275-295.
- Arehart, G.B, Kesler, S.E., O'Neil, J.R., and Foland, K.A., 1992, Evidence for the Supergene Origin of Alunite in Sediment-Hosted Micron Gold Deposits, Nevada: *Economic Geology*, v. 87, pp. 263-270.
- Barrett, T.J. and MacLean, W.H., 1994, Mass Changes in Hydrothermal Alteration Zones associated with VMS Deposits of the Noranda Area: *Exploration and Mining Geology*, v. 3, no. 2, pp. 131-160.
- Bawden, T.M., Einaudi, M.T., Bostick, B.C., Meiborn, A., Wooden, J., Norby, J.W., Orobona, M.J.T., and Chamberlain, C.P., 2003, Extreme ^{34}S depletions in ZnS at the Mike gold deposit, Carlin Trend, Nevada: Evidence for bacteriogenic supergene sphalerite: *Geology*, v. 31, no. 10, p. 913-916.
- Blanchard, R., 1968, Interpretation of leached outcrops: Nevada Bureau of Mines Bulletin, v. 66, 196 p.
- Bonham, H.F., and Sharp, J.V.A., 1957, Geology and mineral resources of township 28 north ranges 34 and 33 east, Mount Diablo base and meridian, Pershing County, Nevada, Southern Pacific Land Company Report, San Francisco.
- Brimhall, G.H., Alpers, C.N., and Cunningham, A.B., 1985, Analysis of Supergene Ore-Forming Processes and Ground-Water Solute Transport Using Mass Balance Principles: *Economic Geology*, v. 80, pp. 1227-1256.
- Bureau of Land Management, February 2016, Coeur Rochester Mine Plan of Operations Amendment 10 and Closure Plan Final EIS: U.S. Department of Interior, Winnemucca District, Humboldt River Field Office, Figure 4-1.
- Burke, D.B., and Silberling, N.J., 1973, The Auld Lang Syne Group of Late Triassic and Jurassic (?) age, north-central Nevada: U.S. Geological Survey Bulletin B 1394-E, 14 p.
- Cameron, E.N., 1989, Geology and mineralization of the northeastern Humboldt Range, Nevada: *Geological Society of America Bulletin*, v. 50, p. 563-634.

- Chadwick, T.H. and Harvey, D., 2001, Geologic Mapping and Exploration of the Rochester Pit, Pershing County, Nevada: Submitted to Coeur Explorations, Inc., 32 p.
- Chadwick, T.H., 2014, Geologic Mapping and assessment, Prepared for Coeur Mining, Inc.
- Chadwick, T.H., Robinson, W., and White, B., 2016, Geologic Map of the Rochester Mine Pit: prepared for Coeur Mining Inc.
- Cheong, S., 1999, Structural setting and fluid characteristics of metamorphic gold-quartz veins in northwest Nevada: Unpublished Ph.D. dissertation, University of Nevada, Reno, 332 p.
- Chitayeva, N.A., Miller, A.D., Grosse, Y.I., and Christyakova, N.I., 1971, Iodine distribution in the supergene zone of the Gay chalcopyrite deposit, *Geochemical International*, v. 8, 426-436.
- Coeur Mining Inc., 2015, Annual Report, Part 1 Item 2, http://investors.coeur.com/interactive/lookandfeel/4349317/Coeur_2015_AR.pdf
- Colgan, J.P., Dumitru, T.A., Reiners, P.W., Wooden, J.L., and Miller, E.L., 2006, Cenozoic tectonic evolution of the Basin and Range province in northwestern Nevada: *American Journal of Science*, v. 306, p. 616-654.
- Corkhill, C.L. and Vaughn, D.J., 2009, Arsenopyrite oxidation - A review: *Applied Geochemistry*, v. 24, pp. 2342-2361.
- Crosby, B., 2012, Gold and Base Metal Mineralization, Hydrothermal Alteration and Vein Paragenesis in the Spring Valley Deposit, Pershing County, Nevada: Unpublished M.S. Thesis, University of Nevada, Reno, 191 p.
- Crosby, B.L., and Thompson, T.B., 2015, Vein Textures, Mineralization and Hydrothermal Alteration of the Spring Valley Deposit, Pershing County, Nevada, *Geological Society of Nevada, 2015 Symposium*, pp. 551-582.
- Crowl, W.C., Black, Z.J., and Malhotra, D., 2014, Amended NI 43-101 Technical Report on Resources Spring Valley Project, Pershing County, Nevada, Prepared for Midway Gold, 140 p.
- Cuadra C., P. and Roja S., G., 2001, Oxide Mineralization at the Radomiro Tomic Porphyry Copper Deposit, Northern Chile: *Economic Geology*, v. 96, pp. 387-400.
- Elison, M.W. and Speed, R.C., 1989, Structural development during flysch basin collapse: the fencemaker allochthon, East Range, Nevada: *Journal of Structural Geology*, v. 11, no. 5, pp. 523-538.
- Emmons, H., 1917, The enrichment of ore deposits: *U.S. Geological Survey Bulletin* 625, 530 p.
- Fanlo, I., Subias, I., and Mateo, E., 2010, Supergene Enrichment of Primary Cu-Ag Assemblages in Ag at the Pardos Deposit, Iberian Range, Spain: *The Canadian Mineralogist*, v. 48, pp 415-430.

- Ferguson, H.G., Roberts, R.J., and Muller, S.W., 1952, Geology of the Golconda quadrangle, Nevada: U.S. Geological Survey Geologic Quadrangle Map GQ-15.
- Fifarek, R.H., Prihar, D.W., Hillesland, L.L., Casaceli, R.J., and Dilles, P.A., 2015, Tectonostratigraphic Framework and Timing of Mineralization at the Relief Canyon Mine, Pershing County, Nevada: Geological Society of Nevada Symposium 2015, v. 1, pp. 453-482.
- Fosdick, J.C. and Colgan, J.P., 2008, Miocene extension in the East Range, Nevada: A two-stage history of normal faulting in the northern Basin and Range: GSA Bulletin, v. 120, p. 1198-1213.
- Gallagher, K., Brown, R., and Johnson, C., 1998, Fission track analysis and its applications to geological problems: Annual Review of Earth and Planetary Sciences, v. 26, p. 519–572.
- Gammons, C. H., and Yu, Y., 1997, The stability of aqueous silver bromide and iodide complexes at 25-300°C: Experiments, theory, and geologic applications: Chemical Geology, v. 137, pp. 155-173.
- Graham, A., 1999, Late Cretaceous and Cenozoic History of North American Vegetation: Oxford University Press, New York, 350 p.
- Green, P.F., Duddy, I.R., Gleadow, A.J.W., Tingate, P.R., and Laslett, G.M., 1986, Thermal annealing of fission tracks in apatite 1. Variable temperature behaviour: Chemical Geology: Isotope Geoscience, v. 59, pp. 237-253.
- Greffie, C., Bailly, L, and Milesi, JP., 1993, Supergene Alteration of Primary Ore Assemblages from Low-Sulfidation Au-Ag Epithermal Deposits at Pongkor, Indonesia, and Nazareno, Peru: Economic Geology, v. 97, pp. 561-571.
- Gustafson, L.B., and Hunt, J.P., 1975, The Porphyry Copper Deposit at El Salvador, Chile: Economic Geology, v. 70, no. 5, pp. 857-912.
- Haug, G.H. and Tiedemann, R., 1998, Effect of the formation of the Isthmus of Panama on Atlantic Ocean thermohaline circulation: Nature, v. 393, pp. 673-676.
- Heck, F. R., 1987, Mesozoic foreland deformation and paleogeography of the western Great Basin, Humboldt Range, Nevada: Unpublished Ph.D. dissertation, Evanston, Illinois, Northwestern University, 214 p.
- Heidel, C., Tichomirowa, M., and Breitkopf, C., 2011, Sphalerite oxidation pathways detected by oxygen and sulfur isotope studies: Applied Geochemistry, v. 26, pp. 2247-2259.
- Hem, J.D., 1985, Study and interpretation of the chemical characteristics of natural water: U.S. Geological Survey, Water Supply Paper 2254, 263 p.
- Ilchick, R.P., 1990, Geology and geochemistry of the Vantage gold deposits, Alligator Ridge-Bald Mountain mining district, Nevada: Economic Geology, v. 85, pp. 50-75.

- John, D., and Muntean, J., 2006, Summary of Characteristics of Tertiary Metallic Mineral Deposits in the Lovelock Area, Northwestern Nevada: Geological Society of Nevada, 2006 Spring Field Trip Guidebook, spec. pub. no. 42, pp. 60-69.
- Johnson, M.G., 1977, Geology and Mineral Deposits of Pershing County, Nevada: Nevada Bureau of Mines and Geology, Bulletin 89, 115 p.
- Johnson, D.A. and Barton, M.D., 2000, Time-Space Development of an External Brine Dominated, Igneous-Driven Hydrothermal System: Humboldt Mafic Complex, Western Nevada: Society of Economic Geologists Field Trip Guidebook, spec. pub. 32, pp. 127-143.
- Kerr, P.F., and Jenney, P., 1935, Dumortierite-andalusite mineralization at Oreana: Economic Geology, v. 80, p. 287-800.
- Ketcham, R.A., Carter, A., Donelick, R.A., Barbarand, J., and Hurford, A.J., 2007, Improved modeling of fission-track annealing in apatite: American Mineralogist, v. 92, p. 799–810.
- Kistler, R.W., and Speed, R.C., 2000, $^{40}\text{Ar}/^{39}\text{Ar}$, K-Ar, Rb-Sr whole rock and mineral ages, chemical composition, strontium, oxygen and hydrogen isotope systematics of Jurassic Humboldt Lopolith and Permian(?) and Triassic Koipato Group rocks, Pershing and Churchill Counties, Nevada: U.S. Geological Survey Open-File Report 00-217, 14p.
- Kleinhampl, F.J., and Ziony, J.I., 1984, Mineral Resources of Northern Nye County, Nevada: Nevada Bureau of Mines and Geology, U.S. Geol. Surv., Bulletin 99B, 243 p.
- Knopf, A., 1924, Geology and ore deposits of the Rochester district, Nevada: U.S. Geol. Surv., Bulletin 762, 78 p.
- Lawrance, L.M., 2007, The supergene behavior of gold: A natural enrichment and refinement phenomenon: Proceedings of Advances in the understanding of supergene processes, Ores and Orogenesis symposium, Tucson, Arizona, p.9–10.
- Mann, A.W., 1984, Mobility of Gold and Silver in Lateritic Weathering Profiles: Some Observations from Western Australia: Economic Geology, v. 79, pp. 38-49.
- Martz and Reid, 1987, Preliminary Rock Descriptions: Prepared for Coeur Rochester, Inc., 33 p.
- Marvin, R.F., and Dobson, S.W., 1979, Radiometric ages – compilation A, U.S. Geological Survey: Isochron/West, no. 26, p. 3-32.
- McDougall, I., and Harrison, T.M., 1999, Geochronology and thermochronology by the $^{40}\text{Ar}/^{39}\text{Ar}$ method: New York, Oxford University Press, xii, 269 p.
- Moeller, S.A., 1988, Geology and mineralization in the Candelaria district, Mineral County, Nevada, In: R.W. Schafer, J.J. Cooper, and P.G. Vikre (Editors), Bulk Mineable Precious Metal Deposits of the Western United States, Geological Society of Nevada, pp. 135-158.

- Nevada Bureau of Mines and Geology (NBMG), 2014, Great Basin Groundwater Geochemical Database: <http://www.nbmge.unr.edu/geothermal/GeochemDatabase.html> (accessed November 2016)
- Nichols, K.M., and Silberling, N.J., 1977; Stratigraphy and deposition history of the Star Peak Group (Triassic), northwestern Nevada: Geological Society of America, Special paper 178, 73 p.
- Nolan, T.B., 1930, The Underground Geology of the Western Part of the Tonopah Mining District, Nevada: Nevada Bureau of Mines, U.S. Geol. Surv., vol. 24, no. 4, 19 p.
- Page, B.M., 1959, Geology of the Candelaria Mining District, Mineral County, NV: Nevada Bureau of Mines and Geology, Bulletin 56, 67 p.
- Price, J.G., Price, E.M., Callicrate, T.E., Howald, W.C., Conelea, R., Pinto da Silva, R.M., Struhsacker, E.M., Miller, M.S., Coolbaugh, M.F., and Johnson, S., 2014, Mineral Deposits and Minerals of the Humboldt and Trinity Ranges and Majuba Hill: Geological Society of Nevada, 2014 Spring Field Trip Guidebook, spec. pub. no. 58, 149 p.
- Rainbow, A., Kyser, T.K., and Clark, A.H., 2006, Isotopic evidence for microbial activity during supergene oxidation of a high-sulfidation epithermal Au-Ag deposit: Geological Society of America, v. 34, pp. 269-272.
- Reich, M., Chryssoulis, S.L., Deditius, A., Palacios, C., Zuniga, A., Weldt, M., and Alvear, M., 2010, "Invisible" silver and gold in supergene digenite ($\text{Cu}_{1.8}\text{S}$): *Geochimica et Cosmochimica, acta* 74, p. 6157-6173.
- Retallack, G.J., 2004, Late Miocene climate and life on land in Oregon within a context of Neogene global change: *Palaeogeography, Palaeoclimatology, Palaeoecology*, v. 214, pp. 97-123.
- Robinson, G., Lippoth, K., McFarland, A., Mondragon, R., and Willis, D., 2014, NI 43-101 Technical Report for the Rochester Mine, Lovelock, NV, USA: prepared for Coeur Mining, Inc., 215 p.
- Ross, C.P., 1953, The Geology and Ore Deposits of the Reese River District, Lander County, Nevada: U.S. Geol. Surv., Bulletin 997, 132 p.
- Saunders, J.A., 1993, Supergene oxidation of bonanza Au-Ag veins at the Sleeper Deposit, Nevada, USA: implications for hydrogeochemical exploration in the Great Basin: *Journal of Geochemical Exploration*, v. 47, pp. 359-375.
- Schrader, F.C., 1914, The Rochester mining district, Nevada, Geological Survey, Bulletin 580M.
- Schweickert, R.A., Arehart, G.B., Donelick, R.A., and Vikre, P.G., 2006, Cenozoic structural and thermal history of part of the western margin of the Humboldt Range, Nevada; preliminary interpretations, Geological Society of America, Abstracts with Programs, v 38, p. 79.

- Silberling, N.J., 1973, Geologic events during Permian-Triassic time along the Pacific margin of the United States in Logan, A., and Hills, L.V., eds. The Permian and Triassic systems and their mutual boundary: Calgary, Alberta Soc. Petroleum Geologists, p. 345-362.
- Silberling, N.J. and Roberts, R.J., 1962, Pre-Tertiary stratigraphy and structure of northwestern Nevada: Geological Society of America, Special Paper 72, 58 p.
- Silberling, N.J., and Wallace, R. E., 1967, Geologic map of the Imlay quadrangle Pershing County, Nevada: U.S. Geol. Survey Map GQ-666.
- Silberling, N.H., and Nichols, K.M., 1982, Middle Triassic Molluscan Fossils of Biostratigraphic Significance from the Humboldt Range, Northwestern Nevada: U.S. Geological Survey Professional Paper 1207, 77 p.
- Sillitoe, R.H., 2005, Supergene Oxidized and Enriched Porphyry Copper and Related Deposits: Economic Geology 100th Anniversary Vol., pp. 723-768.
- 2007, Hypogene Reinterpretation of Supergene Silver Enrichment at Chanarcillo, Northern Chile: Bulletin of the Society of Economic Geologists, v. 102, pp. 777-781.
- 2009, Supergene Silver Enrichment Reassessed: Society of Economic Geologists, Special Publication, pp. 15-32.
- Sillitoe, R.H. and Lorson, R.C, 1994, Epithermal Gold-Silver-Mercury Deposits at Paradise Peak, Nevada: Ore controls, Porphyry Gold Association, Detachment Faulting, and Supergene Oxidation: Economic Geology, v. 89, pp. 1228-1248.
- Sillitoe, R.H. and McKee, E.H., 1996, Age of Supergene Oxidation and Enrichment in the Chilean Porphyry Copper Province: Economic Geology, v. 91, pp. 164-179.
- Silver, E., MacKnight, R., Male, E., Pickles, W., Cocks, P., and Waibel, A., 2011, LiDAR and hyperspectral analysis of mineral alteration and faulting on the west side of the Humboldt Range, Nevada: Geosphere, v. 7, no. 6, p. 1357-1368.
- Stager, H.K., 1977, Geology and Minerals Deposits of Lander County, Nevada, Part II Mineral Deposits: Nevada Bureau of Mines and Geology, Bulletin 88, pp. 106.
- Stoffregen, R., 1986, Observations on the behavior of gold during supergene oxidation at Summitville, Colorado, U.S.A., and implications for electrum stability in the weathering environment: Applied Geochemistry, v. 1, pp. 549-558.
- Surour, A.A., Harbi, H.M., and Ahmed, A.H., 2014, The Bi'r Tawilah deposit, central western Saudi Arabia: Supergene enrichment of a Pan-African epithermal gold mineralization: Journal of African Earth Sciences, v.89, pp. 149-163.
- Titley, S., and Marozas, D.C., 1995, Processes and products of supergene copper enrichment: Arizona Geological Society 20, p. 156-168.

- Vanderbug, W.O., 1936, Reconnaissance of mining districts in Pershing County, Nevada: U.S. Bureau Mines Inf. Circ. 6902, 57 p.
- Vasconcelos, P.M., Brimhall, G.H., Becker, T.A., and Renne, P.R., 1994, $^{40}\text{Ar}/^{39}\text{Ar}$ analysis of supergene jarosite and alunite: Implications to the paleoweathering history of the western USA and West Africa: *Geochimica et Cosmochimica Acta*, v. 58, pp. 401-420.
- Vetz, N.Q., 2011, Geochronologic and Isotopic Investigation of the Koipato Formation, Northwestern Basic, Nevada: Implications for Late Permian-Early Triassic Tectonics Along the Western U.S. Cordillera: Unpublished M.S. Thesis, Boise State University, 147 p.
- Vikre, P., 1977, Geology and silver mineralization of the Rochester district, Pershing County, Nevada: Unpublished Ph.D. dissertation, Stanford University, 404 p.
- 1981, Silver Mineralization in the Rochester District, Pershing County, Nevada: *Economic Geology*, v. 76, pp. 580-609.
- 2014, Magmatism, metasomatism, tectonism, and mineralization in the Humboldt Range, Pershing County, Nevada: Geological Society of Nevada 2014 Spring Field Trip Guidebook, spec. pub. no. 58, p. 179-204.
- Wallace, R.E., Tatlock, D.B., and Silberling, N. J., 1960, Intrusive rocks of Permian and Triassic age in the Humboldt Range, Nevada: U.S. Geol. Survey Prof. Paper 400-B, p. B291-B293.
- Wallace, R.D., Silberling, N.J., Irwin, W.P., and Tatlock, D.B., 1969a, Geologic map of the Unionville quadrangle Pershing and Churchill Counties, Nevada: U.S. Geol. Surv. Map GQ-820.
- 1969b, Geologic map of the Buffalo Mountain quadrangle Pershing and Churchill Counties, Nevada: U.S. Geol. Survey Map GQ-821.
- Webster, J.G. and Mann, A.W., 1984, The influence of climate, geomorphology and primary geology on the supergene migration of gold and silver: *Journal of Geochemical Exploration*, v. 22, p 21-42.
- White, B., and Chadwick, T.H., 2015, Geologic Map of the Rochester Mine Pit: prepared for Coeur Mining, Inc.
- Whitehill, C.S., Faulds, J., and Thompson, G., 2008, Geologic and thermochronologic constraints on the structural evolution of the Shawave-Nightingale horst block, northwestern Nevada: Geological Society of America, Abstracts with Programs, v. 41, p. 31.
- Wilkins, J., 2010, Structural and Stratigraphic Age Constraints of the Inskip Formation, East Range, Nevada: Implications for Mesozoic Tectonics of Western North America: Unpublished M.S. thesis, Boise State University, Boise, Idaho, 117 p.
- Williams, P.A, 1990, Oxide Zone Geochemistry: Ellis Horwood Series on Inorganic Chemistry, 286 p.

- Wolfe, J.A., 1994, Tertiary climate changes at the middle latitudes of western North America, *Palaeogeography, Palaeoclimatology, Palaeoecology*, v. 108, pp. 195-205.
- Wyld, S.J., 2002, Structural evolution of a Mesozoic backarc fold-and-thrust belt in the U.S. Cordillera: New evidence from Northern Nevada: *Geological Society of America Bulletin*, v. 114, p. 1452-1468.
- Wyld, S.J., Rogers, J.W., Copeland, P., 2003, Metamorphic Evolution of the Luning-Fencemaker Fold-Thrust Belt, Nevada: Illite Crystallinity, Metamorphic Petrology, and $^{40}\text{Ar}/^{39}\text{Ar}$ Geochronology: *The Journal of Geology*, v. 111, pp. 17-38.
- Wyld, S.J., 2016, The Elusive Fencemaker Thrust: Just one part of a broader East Pershing County Jurassic Deformation Belt: presented at Geological Society of Nevada, Winnemucca chapter, 14 Sept.
- Yesares, L., Saez, R., Nieto, J.M., Ruiz de Almodovar, G., and Cooper, S., 2014, Supergene enrichment of precious metals by natural amalgamation in the Las Cruces weathering profile (Iberian Pyrite Belt, SW Spain): *Ore Geology Reviews*, v. 58, p. 14-26.
- Yonkee, W.A., and Weil, A.B., 2015, Tectonic evolution of the Sevier and Laramide belts within the North American Cordillera orogenic system: *Earth-Science Reviews*, v. 150, pp. 531-593.